



UNIVERSITY OF LEEDS

# Variational quantum algorithms and the complexity of many-body systems



Gabriel da Fonseca Matos

University of Leeds

School of Physics and Astronomy

Submitted in accordance with the requirements for the degree of

*Doctor of Philosophy*

June, 2023

## Intellectual Property Statement

The candidate confirms that the work submitted is his own, except where work which has formed part of jointly authored publications has been included. The contribution of the candidate and the other authors to this work has been explicitly indicated below. The candidate confirms that appropriate credit has been given within the thesis where reference has been made to the work of others.

- Chapters 3 and 4 contain work from the publication [116] Matos, G., Self, C. N., Papić, Z., Meichanetzidis, K., and Dreyer, H. (2023). Characterization of variational quantum algorithms using free fermions. *Quantum*, 7:966. The research contained therein can be directly attributed to me; the remaining authors took on a supervisory role and contributed to the discussion.
- Chapter 5 contains work from the publication [115] Matos, G., Johri, S., and Papić, Z. (2021). Quantifying the efficiency of state preparation via quantum variational eigensolvers. *PRX Quantum*, 2:010309. I did the numerics and main research, while Sonika Johri helped in analysing the link between interaction distance and QAOA, and Zlatko Papić took on a supervisory role and helped direct the research.
- Chapter 6 contains work from the publication [114] Matos, G., Hallam, A., Deger, A., Papić, Z., and Pachos, J. K. (2021). Emergence of gaussianity in the thermodynamic limit of interacting fermions. *Phys. Rev. B*, 104:L180408. The main numerical work and analysis were done by me. Jiannis Pachos and Zlatko Papić took on a supervisory role and helped direct the research. Jiannis Pachos also computed the bound of  $\mathcal{W}$  by the interaction distance. Aydin Deger helped compute the correlation length across the phase diagram of the XYZ model.

Andrew Hallam contributed the robustness under realistic conditions study.

This copy has been supplied on the understanding that it is copyright material and that no quotation from the thesis may be published without proper acknowledgement.

The right of Gabriel da Fonseca Matos to be identified as Author of this work has been asserted by him in accordance with the Copyright, Designs and Patents Act 1988.

© 2023 The University of Leeds and Gabriel da Fonseca Matos.

## Acknowledgements

I would like to thank my supervisors, Zlatko Papić and Jiannis Pachos, for supporting me throughout my doctoral degree. They have been pivotal in shaping my research and academic experience, and I can only express my sincere gratitude for their time and availability during the years I have conducted my research in Leeds.

It has been a great pleasure and privilege to work with all of my collaborators, Sonika Johri, Aydin Deger, Henrik Dreyer, Andrew Hallam, Chris Self, and Konstantinos Meichanetzidis. The insight they provided and the fruitful discussions we had were invaluable. I also wish to thank Sam Duffield, Steve Clark, Douglas Brown and Wenduan Xu, with whom I had the great opportunity to work with during the time I spent at Quantinuum.

My time in Leeds would not have been the same without the valuable friends I made there. I thank my friends and colleagues Jean-Yves Desaulles, Matt Girling, Rhea Turner, Chris Turner and Si Chen for their irreplaceable companionship and all the discussions we have had over the years. I also thank my friends Marco Caggianelli, Saurabh Singh, Isabell Hub and Lili Bakó for all the memorable and wholesome times we had.

I am deeply grateful to my parents and my grandparents for their lifelong support and for, ultimately, making it possible for me to pursue this degree. Last, but certainly not least, I thank Shruti for all the support and love she has given me, for which words can not express how thankful and blessed I am.

## Abstract

Recently, variational quantum algorithms have received much attention, having the potential to be successfully run on near-term quantum computers. In this thesis, we study these algorithms from a quantum many-body systems perspective. The Lie theoretical framework for variational quantum algorithms is expanded upon, and we show that the states that a variational algorithm can prepare are the ground states of the Hamiltonians in the Lie algebra of the corresponding parameterised circuit. Leveraging this, we prove that the 1D QAOA can prepare all states mappable to a fermionic Gaussian state through the Jordan-Wigner transformation. We exploit this to conduct a numerical study, where we find that the use of symmetries can overly constrain the optimisation when the target Hamiltonian is non-local. Further, we characterise the overparameterised regime of optimisation, where we find that, as the circuit becomes more overparameterised, the number of iterations to reach the solution sharply decreases before saturating, and that this number goes from a polynomial to a linear scaling in the size of the lattice. By modifying the variational protocol to increase its expressibility, we study non-integrable systems, where we find that the success of state preparation can be quantified by the interaction distance, an entanglement-based measure of fermionic Gaussianity. We employ this measure in an analysis of the XYZ model, where we quantify the emerging freedom of the ground state of the model in the thermodynamic limit. Our work furthers the understanding of how variational algorithms are influenced by the physical properties of the model, the choice of parameterised circuit, and the classical optimisation of the associated parameters.

# CONTENTS

<b>1</b>	<b>Introduction</b>	<b>1</b>
<b>2</b>	<b>Background: Spin systems through a fermionic perspective</b>	<b>5</b>
2.1	Lattice models . . . . .	6
2.2	Fermionic systems . . . . .	7
2.3	Spin systems and spin-fermion mappings . . . . .	8
2.4	Free-fermionic systems . . . . .	9
2.5	Entanglement in many-body systems . . . . .	14
2.6	Interaction distance . . . . .	17
2.7	Example: The Ising model . . . . .	20
<b>3</b>	<b>The expressibility of Variational Quantum Algorithms</b>	<b>24</b>
3.1	Background: Variational Quantum Algorithms . . . . .	26
3.1.1	Brief summary of different types of VQA . . . . .	27
3.1.2	Connecting VQAs to Adiabatic State Preparation . . . . .	30
3.1.3	The barren plateau phenomenon . . . . .	31
3.2	Lie Theory of Parameterised Quantum Circuits . . . . .	33
3.2.1	Background: Characterising unitaries generated by a PQC . . . . .	33
3.2.2	Characterising states generated by a PQC . . . . .	34
3.3	The expressibility of the 1D QAOA in terms of free-fermions . . . . .	35
3.4	Conclusion . . . . .	44
<b>4</b>	<b>Optimisation in free-fermionic Variational Quantum Algorithms</b>	<b>46</b>
4.1	Minimum circuit depth for maximum expressibility . . . . .	48
4.2	Effect of symmetry on cost minimisation . . . . .	49

4.2.1	Influence of Hamiltonian locality on problem difficulty . . . . .	51
4.2.2	Cost stagnation and “staircase” plateaus . . . . .	53
4.2.3	Rate of vanishing of gradients with lattice size . . . . .	55
4.3	The overparameterised regime . . . . .	57
4.3.1	Change in optimisation with increasing circuit depth . . . . .	58
4.3.2	Number of parameters and choice of optimisation algorithm . . . . .	61
4.4	Conclusion . . . . .	63
<b>5</b>	<b>Effect of interactions on state preparation with variational quantum algorithms</b>	<b>65</b>
5.1	Preparing the ground state of non-integrable quantum models . . . . .	66
5.1.1	Transverse and longitudinal field Ising model . . . . .	67
5.1.2	Three-spin Ising model . . . . .	73
5.1.3	Non-integrable Cluster Ising model . . . . .	76
5.1.4	Additional data . . . . .	78
5.2	Relation between variational algorithms and interaction distance . . . . .	78
5.3	Optimisation landscape . . . . .	81
5.4	Conclusions . . . . .	84
<b>6</b>	<b>Towards an experimental quantification of fermionic interactions</b>	<b>86</b>
6.1	Background: The XYZ Model . . . . .	87
6.2	Background: Matrix Product States and the DMRG algorithm . . . . .	90
6.3	Interaction distance and emergent freedom in the XYZ model . . . . .	95
6.4	Violation of Wick’s theorem as an experimental proxy for interaction distance . . . . .	98
6.5	Robustness of experimental probe under realistic conditions . . . . .	103
6.6	Conclusions . . . . .	104
<b>7</b>	<b>Conclusions</b>	<b>107</b>
<b>Bibliography</b>		<b>112</b>

# LIST OF FIGURES

3.1	A schematic illustrating a variational quantum-classical optimisation routine. The optimisation involves $n$ parameters $\theta_j$ , where $j = 1, 2, \dots, n$ . For the ansatz in Eq. (3.22), $n = pm$ . . . . .	27
3.2	Schematic depicting the Lie structures introduced in Section 3.2 and their relation to variational optimisation. From an initial state, the set of unitaries generated by the parameterised circuit, $\mathcal{U}$ , prepares a manifold of states $\mathcal{S}$ . The space of directions that the protocol is able to explore at a given point is characterised by the Lie algebra $\mathfrak{u}$ , and there is a redundancy in the unitaries preparing a state which is represented by a stabiliser Gauge group $\mathcal{G}$ . Symmetries in the protocol constrain the optimisation (a) to a submanifold of states $\mathcal{S}_{\text{sym}}$ which, as later explained in Section 4.2, may affect the landscape by introducing local minima (b) or by restricting the features available to the optimiser, causing the optimisation to take longer (c). . . . .	36
3.3	Parameterised circuits corresponding to the variational protocols (3.28), (3.29). . . . .	37

4.1 Cost function optimisation traces exposing the differences between the minimisations as the protocol and target Hamiltonian change. The effect of circuit depth is probed using the exactly parameterised regime ( $p = L/2$ ) and the overparameterised regime ( $p = L^2/4$ ). The target Hamiltonian is (Top row): the Ising model, as in Eq. (4.2), and 5 random initialisations per value of  $p$ , lattice size and protocol. (Bottom row): 3 randomly generated symmetric quadratic Hamiltonians, as in Eq. (4.3), and 5 random initialisations per generated Hamiltonian, value of  $p$ , lattice size and protocol. The maximum lattice size in each plot reflects the time taken to optimise the circuits, which depends on the number of parameters and on the number of iterations needed for convergence. . . . . 50

4.2 Effect of Hamiltonian locality on optimisation hardness in both the site-dependent and site-independent protocols in the exactly parameterised regime using PBCs. The labels refer to the target Hamiltonians defined in Eqs. (4.6), (4.7) and (4.8). The lattice size is 12, except for  $H_{LG}$ , which was computed for  $L = 16$ , as was  $H_C$  with the site independent protocol (this has no particular significance or influence in the results). Between 20 and 150 random initialisations were computed for each Hamiltonian parameter in the site-dependent cases, and between 200 and 500 were computed in the site independent ones. These indicate the number of samples until the results converged; the exact number needed depends on the specific Hamiltonian. The solid line is the mean value, while the shaded area indicates one standard deviation. . . . . 53

- 4.3 (a) Optimisation traces showing the “staircase” pattern seen in Figure 4.1. Here, the system size is 40, and the label refers to the protocol used and the Hamiltonian targetted, respectively. PBCs and  $p = L/2$  are used. (b) Overlaps of the lowest excited states of the target Hamiltonian with the state under preparation  $|\psi(\boldsymbol{\theta})\rangle$ . Numbers in the legend indicate eigenstate indices, with 0 being the ground state, 1 being the first excited state, etc. Single indices indicate that overlap with the corresponding eigenstate is being plotted. A range of indicate that the sum of the overlaps with the eigenstates having indices in that range is being plotted. We see a high overlap with the first excited state throughout the optimisation, indicating that the cost function cannot easily distinguish this state from the ground state. The site-independent protocol was used and the Ising model (4.2) was targeted at  $p = L/2$  and  $L = 16$ . 54
- 4.4 Variance of gradient taken at the centre angle  $||\partial e/\partial\theta_j||$  using the site-dependent protocol (left) and the site-independent protocol (right) with the ground state of the Ising model as a target state (top) and 5 generic quadratic Hamiltonians (symmetric quadratic Hamiltonians in the independent case) as a target state (bottom), plotted against the inverse of the dimension of the Lie algebra of the protocol, as computed in Section 3.3 and listed in Table 3.1 (note that here the parity is fixed). Various circuit depths, represented by the quantity  $p/L$  in the labels, were used. 20000 samples were taken per value of  $p$ , Hamiltonian and lattice size. Though the samples pertaining to the 5 generic quadratic Hamiltonians are considered simultaneously in the computation of the variance, plotting this variance separately for each such Hamiltonian does not significantly alter the plots shown. . . . . 56

- 4.5 Variance of gradient taken at centre angle  $||\partial e/\partial\theta_i||$  using the site-dependent protocol (left) and the site-independent protocol (right) with the ground state of the Ising model as a target state (top) and 5 generic quadratic Hamiltonians (symmetric generic quadratic Hamiltonians in the independent case) as a target state (bottom), plotted against various values of  $p$  between 1 and  $4L$ . Several system sizes (bottom labels) were used. 20000 samples were taken per value of  $p$ , random state and lattice size. The vertical line indicates  $p = L/2$ . . . . . 57
- 4.6 Number of iterations to converge vs. the circuit depth in the overparameterised regime. We see a decrease, consistent between different system sizes, which is at first pronounced, but then tapers off until it finally saturates at a circuit depth proportional to  $L^2$ . The insets use a linear scale for the vertical axis; they emphasise the point at which this saturation is reached. The target Hamiltonian is that of the Ising model, Eq. (4.2). Between 5 and 40 random initialisations were performed for each circuit depth; solid lines represent the mean value, and the shaded area indicates standard deviation. . . . . 58
- 4.7 Number of iterations to converge vs. lattice size corresponding to the data in Figure 4.1. Solid line is the mean value, and the shaded area indicates the standard deviation. The legend refers to the Hamiltonian targeted and protocol used, in this order. The target Hamiltonians are either the Ising model, Eq. (4.2), or generic symmetric quadratic Hamiltonians, Eq. (4.3). The number of iterations to converge scales polynomially with system size when  $p = L/2$ . This turns into a linear scaling as the circuit enters the overparameterised regime (right). . . . . 59

4.8 Quantification of how well the gradient accounts for the change in the cost function along the optimisation, both in the exactly parameterised ( $p = L/2$ ) and in the overparameterised ( $p/L = 8$ ) regimes. The plot shows the quantity defined in Eq. (4.10) recorded throughout the optimisation. We see that in the overparameterised regime, the value of the gradient consistently predicts the decrease in the cost function up to a constant factor; while it only accounts for a decreasing fraction of this variation in the exactly parameterised regime. Here, the target state was that of the Ising model with PBCs. . . . . 60

4.9 The parameterisation at minimal circuit depth  $\hat{p}$  (a) matches the dimension of the manifold of states. By the implicit function theorem, the overparameterisation (b) defines local, lower-dimensional parameterisations, also matching the dimension of the manifold. These more adequately capture its features, while describing the optimisation path in a piecewise manner. It is an open question whether a global parameterisation with these properties could be found. . . . . 61

4.10 Different quantities characterising the hardness of the optimisation with increasing circuit depth. On the left, we plot the mean of the logarithm of the number iterations to converge; the centre plot depicts the mean of the sum of all the angles of the protocol, where periodicity is appropriately taken into account; on the right, the average of the logarithm of the total computational time is shown. Generic symmetric quadratic Hamiltonians were targeted, and results were averaged over 5 random states and 5 random initialisations per state. Filled line corresponds to the site-dependent protocol, while dotted line represents the site-independent protocol; these two cases essentially display the same behaviour. Periodic boundary conditions were used, and the black vertical line indicates  $p = L/2$ , the depth at which the circuit is exactly parameterised. These results were obtained on an Intel(R) Xeon(R) CPU E5-2650 v4 @ 2.20GHz. . . . . 62

5.1	Top row: Interaction distance for the ground state of FM (a) and AFM (b) model in Eq. (5.4) as a function of fields $h_x$ and $h_z$ . Bottom row: the infidelity $1 - f$ between the prepared state and the ground state for the FM (c) and AFM model (d). See text for the details of the variational protocol. All data is for system size $L = 8$ using PBCs. Red dot denotes the critical point of the FM model, which is in a ferromagnetic phase (i) throughout the diagram, while the red line is the critical line in the AFM model according to Ref. [146] separating an antiferromagnetic phase (ii) from a paramagnetic phase (iii). . . . .	69
5.2	An $m = 3$ -step variational algorithm for the preparation of the ground state of the Ising model in both transverse and longitudinal fields, discussed in Sec. 5.1. . . . .	71
5.3	(i) Scatter plot of interaction distance $D_{\mathcal{F}}$ against $1 - f$ for the FM Ising model from Fig. 5.1(a),(c). (ii)-(iii): Analogous plot for the AFM Ising model in Fig. 5.1(b),(d), where the data points are taken from the antiferromagnetic (ii) or paramagnetic (iii) phase. Data is for $L = 8$ spins with PBCs and different values of $p$ indicated in the legend. . . . .	73
5.4	Top row: Interaction distance for the 3-spin Ising model in Eq. (5.15) as a function of fields $h_x$ and $h_z$ (a) and the infidelity $1 - f$ (b). The protocol is based on Eqs. (5.5), (5.6), (5.17). All data is for system size $L = 9$ using PBCs. Red line is the critical line in the 3-spin Ising model according to Ref. [153] Bottom row: Scatter plot of $D_{\mathcal{F}}$ against $1 - f$ for the 3-spin Ising model, system size $N = 9$ and different values of $p$ indicated in the legend. Vertical red line, drawn heuristically, separates the data belonging to the phase above and below the critical line (respectively to the left and right of the vertical line). . . . .	74

---

5.5	Top row: Interaction distance for the cluster Ising model in Eq. (5.18) as a function of $h_{yy}$ and $h_y$ (a) and the infidelity $1 - f$ of the protocol (b). All data is for system size $L = 8$ with periodic boundary conditions. Critical line, in red, is reproduced from Ref. [197] and separates a cluster phase (i) from a paramagnetic phase (ii). Bottom row: Scatter plot of $D_{\mathcal{F}}$ against $1 - f$ for the cluster Ising model, system size $L = 8$ and different values of $p$ indicated in the legend. Panel (c) shows points in region (i) while (d) shows points in region (ii). . . . .	77
5.6	Pearson correlation coefficients as a function of $p$ . Labels "FM" and "AFM" refer to the data for the ferromagnetic and antiferromagnetic models in Figures 5.3, "3s" refers to the data for three-spin model in 5.4(c) and "Cluster" refers to the data for the cluster model in 5.5(c). The inset zooms in on the top-right corner of the plot. . . . .	78
5.7	Distribution of angles $\theta_{k,1}$ associated with the Hamiltonian in Eq. (5.5) across phase diagrams of FM/AFM, 3-spin and cluster Ising models in Eqs. (5.4), Eq. (5.15) and Eq. (5.18). Data is for system size $L = 8$ with the exception of $L = 9$ for the 3-spin Ising model. In all the plots, $p = 4$ . . . . .	80
5.8	Probability distribution function $P(\log(\epsilon))$ of QAOA outcomes on 10000 uniformly generated initial angles having as target the ground state of the points in $S$ . Data is for system size $L = 8$ and $p = 4$ , with the protocol in Eqs. (5.7)-(5.5). . . . .	82
5.9	Characterisation of the minimisation landscape of the AFM Ising model. Legend indicates the Hamiltonian featuring in the cost function $\epsilon(\boldsymbol{\theta})$ , and corresponds values of $(h_x, h_z)$ taken to be representative of different regions in the phase diagram. (a)-(b) Minimum relative energy $\epsilon$ found after running the <code>basinhopping</code> optimisation plotted against $T_{\leq \max}$ (resp. $T_{=\max}$ ), where we restrict the optimisation to circuits for which the total amount of time to run (5.28) is less than $T_{\leq \max}$ (resp. to be equal to $T_{=\max}$ ). (c)-(d) t-SNE plot identifying relative positions of minima for 500 random initialisations taken at $(h_x, h_z) = (1, 1)$ and $T_{=\max} = 1$ (resp. $T_{=\max} = 8$ ), where the optimisation is performed using the L-BFGS algorithm. All data is for system size $L = 6$ and $p = 3$ . Color scale in (c), (d) represents the value of $\epsilon$ at the minimum. . . . .	83

- 6.1 Phase diagram of the XYZ model (6.1). Red lines denote gapless regions, and the conformal ( $C$ ) and non-conformal ( $E$ ) tricritical points are indicated. . . . . 88
- 6.2 The process of approximating a quantum state with amplitudes encoded by the tensor  $c_{\sigma_1, \sigma_2, \dots, \sigma_L}$  by a product of matrices  $A_{a_1}^{\sigma_1} A_{a_1, a_2}^{\sigma_2} \dots A_{a_L}^{\sigma_L}$  as in (6.12). A singular value decomposition is successively applied to a matrix obtained by regrouping the indices of the amplitude tensor. This introduces a new index  $a_l$  at each step, corresponding to the multiplication of the matrices in the decomposition. This index is truncated so that the smallest singular values are discarded, yielding an efficient approximate representation for quantum states where the number of relevant singular values scales efficiently with the size of the system. This is the case for e.g. the ground states of gapped systems and certain systems at criticality admitting a logarithmic correction to the entanglement entropy. 92
- 6.3 Interaction distance,  $D_{\mathcal{F}}$ , in Eq. (2.45), obtained using DMRG across the phase diagram of the XYZ model for  $L=200$  spins. Red lines denote critical lines, and the conformal ( $C$ ) and non-conformal ( $E$ ) tricritical points are indicated [54]. Vectors  $\vec{u}_1, \vec{u}_2$  are orthogonal to the critical lines and are used in Fig. 6.4. Interaction distance is strongly suppressed in gapped phases of the XYZ model, signalling the emergence of Gaussianity. The DMRG bond dimension was allowed to scale as necessary. . 97
- 6.4 (a) Exponential decay of  $D_{\mathcal{F}}$  with system size at different points along  $\vec{u}_1$  and  $\vec{u}_2$  cuts through the phase diagram in Fig. 6.3. We observe a short initial increase, followed by a plateau and the final decrease beyond some crossover length scale,  $L_{\min}$ , indicated by the dotted lines. Dashed lines are fits to the asymptotic exponential decay,  $D_{\mathcal{F}} \propto \exp(-rL)$ , for data points  $L > L_{\min}$ . (b) Slope  $k$  of the exponential decay, extracted at various points along  $\vec{u}_1$  and  $\vec{u}_2$ , exhibits a power-law dependence on correlation length  $\xi$ . The latter is computed using the analytic formulas (6.10) applicable in the thermodynamic limit. (c) Correlation length  $\xi$  displays power-law dependence on  $L_{\min}$ . The DMRG bond dimension was set to 512 for computations included in this figure . . . . . 99

- 6.5 (a)-(b) Scatter plots comparing  $|\mathcal{W}|$  in Eq. (6.29) and  $|\mathcal{W}_l|$  in Eq. (6.37) with  $D_{\mathcal{F}}$ , for sizes  $L = 600$  and  $L = 400$ , respectively. We see that  $|\mathcal{W}|$  essentially coincides with  $D_{\mathcal{F}}$ , while  $|\mathcal{W}_l|$  strongly correlates with  $D_{\mathcal{F}}$  below the threshold  $D_{\mathcal{F}}^* \approx 10^{-9}$ . The shaded area,  $D_{\mathcal{F}} > D_{\mathcal{F}}^*$ , corresponds to data points near critical regions with high correlation lengths, where the relationship between  $D_{\mathcal{F}}$  and  $\mathcal{W}_l$  breaks down. (c)  $|\mathcal{W}_l|$  across the phase diagram of the XYZ model in Eq. (6.1) for size  $L = 400$ . When computing  $|\mathcal{W}_l|$ , we use a different Jordan-Wigner axis of quantisation for each region, labelled as follows: in 1 we pick the  $z$  quantisation axis, in 2 we pick the  $x$ -axis, and in 3 the  $y$ -axis. The DMRG bond dimension was allowed to scale as necessary in (a), and was set to 128 in (b) and (c). . . . . 102
- 6.6 (a)  $W_l$  as a function of system size for the long-range XYZ model in Eq. (6.38) with fixed  $J_x = 1.0$ ,  $J_y = -1.0$  and  $J_z = 5.0$  and various  $\alpha$ . (b)  $W_l$  across the  $\vec{u}_2$  cut with different amounts of per-site randomness  $\delta J^{\max}$  applied to the couplings  $J_x$ ,  $J_y$  and  $J_z$  at system size  $L = 100$ . (c)  $W_l$  across the  $\vec{u}_2$  cut with a random local field of strength  $h^{\max}$  applied to every site of an  $L = 100$  system. The DMRG code was run with bond dimension  $\chi = 128$ . . . . . 104

# LIST OF TABLES

3.1	Table summarising the expressibility of the site-dependent, Eq. (3.28), and site-independent, Eq. (3.29), protocols. The basis for the corresponding Lie algebra $\mathfrak{u}$ is referenced in this table. As outlined in the main text, these are used to analytically deduce $\mathcal{U}$ , the space of unitaries that each protocol can generate, and $\mathcal{S}$ , the space of states that each protocol can prepare. We assume that the initial state is a FGS of a given parity respecting the symmetries of the circuit. . . . .	44
-----	--	----

## Abbreviations

CTM	Corner Transfer Matrix
DMRG	Density Matrix Renormalisation Group
FGS	Fermionic Gaussian State
HEA	Hardware Efficient Ansatz
HVA	Hamiltonian Variational Ansatz
MPS	Matrix Product State
MPO	Matrix Product Operator
NISQ	Noisy Intermediate Scale Quantum
OBC	Open Boundary Conditions
PBC	Periodic Boundary Conditions
PQC	Parameterised Quantum Circuit
QAOA	Quantum Approximate Optimisation Algorithm
UCC	Unitary Coupled Cluster
VQA	Variational Quantum Algorithm

---

# CHAPTER 1

---

Introduction

---

Quantum computation is expected to become a useful tool for scientific and industrial applications [126, 213]. With proposed uses in the simulation of quantum condensed matter and quantum chemistry systems [28, 125, 189], accelerating classical combinatorial optimisation routines [71, 108, 125], improving machine-learning models [19, 37], and providing better methods for molecular biology and drug discovery [21, 145], it has attracted an increasing amount of attention. Despite the predicted impact of quantum computing in several industrial and academic sectors, progress in applying it to these domains has been impacted by the fact that current quantum computers – often called Noisy Intermediate Scale Quantum (NISQ) [164] devices – lack full-fledged error correction, currently a prerequisite to the success of quantum algorithms with a speed-up guarantee.

In the past years, a great deal of interest has been centred in finding quantum algorithms that can be successfully run on these so-called NISQ devices. The prime candidate for this are Variational Quantum Algorithms (VQAs) [30], such as the Variational Quantum Eigensolver (VQE), first proposed in the context of quantum chemistry [120], or the Quantum Approximate Optimisation Algorithm (QAOA), which is designed to tackle certain combinatorial optimisation problems [58]. These involve optimising a number of controllable parameters defining a quantum circuit by employing a classical nonlinear optimisation routine, with the goal of finding a quantum state that represents a solution to the problem at hand.

Despite being designed to run on NISQ computers using shallow circuit depths, thus avoiding the accumulation of noise in the course of the computation, employing these variational algorithms raises a number of other issues. One of the main obstacles to their practical application is performing the associated classical nonlinear optimisation, which was in many cases found to be difficult, if not impossible. The most prominent reason for this is the presence of so-called *barren plateaus*, first described in [120], where the gradients with respect to the cost function vanish exponentially in the size of the system. It occurs in several interconnected contexts, such as the variational preparation of entangled states [113], the preparation of states using non-local cost functions [31], the presence of simulation noise [202], or the use of parameterised circuits that are overly expressive [80]. Several strategies have been proposed to circumvent this difficulty, such as using classical shadows to avoid regions of high entanglement [167], the adaptive construction of the parameterised circuit to maximise the gradient at every step [69,

---

217], or the transferability of solutions from small to large system sizes [123, 215], though a universal solution has not yet been found. Another problem arising in the optimisation of variational quantum algorithms is the presence of several low-quality local minima [5, 209], which make it necessary to run the algorithm several times with different initial conditions or to use a global optimisation routine.

Given the above difficulties, the importance of accounting for the optimisation hardness in the design and implementation of the algorithm becomes clear. Much effort has been directed to this endeavour, and several important factors determining the success of the optimisation have been identified, such as the boundary conditions used [180], the locality of interactions (both in the circuit and in the cost function) [79, 190, 193], the depth of the parameterised circuit [94, 95, 99] and the use of symmetries in the circuit [65, 101, 124, 175]. The expressibility of the parameterised circuit employed is likewise important: while universal variational algorithms exist [18, 128], these typically present with barren plateaus [80]. A number of approaches to characterise the expressibility of variational algorithms have been developed [1, 48, 133, 176], such as Lie theoretical techniques inspired by studies on quantum optimal control [3, 99].

In this thesis, we explore and quantify several features determining the hardness of optimisation in variational algorithms. The principal focus of this study will be the preparation of ground states of models representing condensed matter systems, though our conclusions are extended to more general applications. We will link the difficulty of optimisation to a number of physical properties of the system at hand, such as its integrability or the structure of its entanglement spectrum; moreover, we explore how this difficulty is influenced by the choice of the parameterised circuit implementing the variational algorithm.

Throughout this work, we will focus on one-dimensional spin systems, often taking a fermionic perspective by employing a spin-fermion mapping. We introduce these topics in Chapter 2, along with the notion of a free-fermionic system. These admit a representation that is polynomial in the size of the system, enabling them to be simulated efficiently on a classical computer. Moreover, the structure of the entanglement of a quantum state representing such a system follows a well-defined combinatorial pattern that can be described using a number of parameters linear in the size of the system. We review how the complexity of a quantum state can be measured in terms of how the structure of its entanglement diverges from this pattern by computing a quantity

---

called the *interaction distance*.

We proceed to introduce variational quantum algorithms in Chapter 3. There, we review and expand upon the quantum optimal control based Lie theoretical framework for the study of these algorithms. In particular, we show that the ground states of the Hamiltonians belonging to the Lie algebra of the parameterised circuit are precisely those that can be prepared by the algorithm. Exploiting this, we analytically demonstrate that the one-dimensional QAOA can prepare exactly all free-fermionic states.

Leveraging the fact that free-fermionic systems are efficient to simulate classically, we conduct a comprehensive numerical study of the QAOA in Chapter 4. By running the optimisation several times with different initial conditions, we draw conclusions about the influence of symmetries on variational algorithms. Moreover, we are able to probe large circuit depths and lattice sizes, which enables the study of the so-called overparameterised regime of optimisation. We characterise this regime by examining how the optimisation hardness scales with the circuit depth and the lattice size.

This study is extended to interacting models in Chapter 5, where we use the interaction distance to quantify the success of ground state preparation in non-integrable models of many-body systems. We observe that the interaction distance is highly correlated with this success, and that this correlation can also yield information about which phase the model is in. This is observed across the phase diagram of several non-integrable models, such as the Ising model in both a transverse and a longitudinal field.

In Chapter 6, we focus our attention on the interaction distance, and we study it in the context of the XYZ model. We begin by quantifying an emerging freedom in the entanglement spectrum of the ground state of this model as the size of the lattice tends to infinity. By analysing a connection between interaction distance and Wick's theorem, we explore the possibility of measuring the interaction distance experimentally, and discuss what this would involve in general cases.

Finally, we conclude in Chapter 7, where we summarise the contributions of this work and lay out further lines of research to be pursued in the future.

---

# CHAPTER 2

---

Background: Spin systems through a fermionic perspective

In this chapter, we will review the mathematical description of spin and fermionic systems. These can be mapped to one another through so-called spin-fermion mappings, such as the Jordan-Wigner transformation, which we will describe in detail. We will then emphasise a subset of fermionic systems which is non-interacting, the free-fermionic systems. These admit a representation of its quantum states and Hamiltonian that is polynomial in the size of the system, enabling them to be efficiently simulated classically. Finally, we review the notions of quantum entanglement and of the entanglement spectrum, and introduce the interaction distance, an entanglement-based measure of how far generic fermionic systems are from free-fermionic ones [192].

## 2.1 Lattice models

In quantum many-body physics, the models describing physical phenomena are often defined on some underlying lattice, which consists of a collection  $\mathcal{L}$  of points (or *sites*) arranged in space. Each site hosts a physical entity (e.g. a particle) described by a vector space  $\mathcal{H}$ , along with a natural set of observables. The full system is then described by the *tensor product* of each individual vector space  $\bigotimes_{p \in \mathcal{L}} \mathcal{H}_p$ . The associated dynamics is defined by a Hamiltonian  $H$  that can be expressed in terms of sums of tensor products of observables on each site. As is usual, where this product is at no risk of being mistaken for the standard matrix product, we will represent it by omitting the  $\otimes$  symbol i.e. we write  $A_1 \otimes A_2$  as  $A_1 A_2$ .

In this work, we will concern ourselves with one-dimensional lattices of fermions (introduced in Section 2.2) and spins (introduced in Section 2.3). We will either work with open boundary conditions (OBC), in which case the sites are assumed to be arranged in a straight line, or periodic boundary conditions (PBC), where the first and last sites are assumed to be adjacent to each other. In certain cases, the system under study may be symmetric with respect to a permutation of the lattice sites. If  $P$  is an operator representing the effect of such a permutation on  $\bigotimes_{p \in \mathcal{P}} \mathcal{H}_p$ , this mathematically translates to the Hamiltonian satisfying  $H = PHP^{-1}$ . Two symmetries we will encounter is a translation symmetry, which results in shifting all the lattice sites forward by one (the last site is assigned to the first one), and a reflection symmetry, which assigns the first site to the last site, the second site to the second to last site, and so forth (if the lattice has an odd number of sites, the centre site remains unchanged).

## 2.2 Fermionic systems

A system composed of a single spinless fermion can be represented by a vector space having two states  $\mathcal{H} = \text{span}\{|0\rangle, |1\rangle\}$ , where  $|0\rangle$  indicates the vacuum, i.e. the absence of a fermion, and  $|1\rangle$  is a quantum state representing its presence. The corresponding description for a lattice of  $N$  sites, each potentially hosting a fermion, is commonly given in terms of a set of *creation operators*  $\{a_j^\dagger\}_{j=1}^N$  acting as

$$|\alpha_1 \dots \alpha_N\rangle = (a_1^\dagger)^{\alpha_1} \dots (a_N^\dagger)^{\alpha_N} |0\rangle. \quad (2.1)$$

A corresponding set of annihilation operators is defined by the Hermitian conjugate of the creation operators. As the name suggests, these correspond to the creation, or destruction, of a fermion on a lattice site. For example, on a lattice with four sites,  $|0101\rangle = a_2^\dagger a_4^\dagger |0\rangle$  corresponds to a quantum state with one fermion occupying the second site and one occupying fourth site. To be consistent with fermionic exchange statistics (i.e. the fact that exchanging two fermions incurs a phase of  $-1$  in the corresponding quantum state), these sets of operators must satisfy the canonical anticommutation relations

$$\{a_j, a_k\} := a_j a_k + a_k a_j = 0, \quad (2.2)$$

$$\{a_j^\dagger, a_k\} = a_j^\dagger a_k + a_k a_j^\dagger = \delta_{jk}, \quad (2.3)$$

thus forming a *CAR algebra* [166] (where CAR is an acronym for canonical anticommutation relations).

The fermions we have introduced so far are *complex fermions*; these describe particles distinct from their own antiparticles. This contrasts with the behaviour of the so-called *Majorana fermions*, named after Ettore Majorana, who first proposed them when describing electrically neutral particles [111]. The corresponding operators can be defined in terms of the fermionic creation and annihilation operators previously introduced as

$$\gamma_{2j-1} := a_j^\dagger + a_j, \quad (2.4)$$

$$\gamma_{2j} := i(a_j^\dagger - a_j), \quad (2.5)$$

and satisfy the relations

$$\{\gamma_j, \gamma_k\} := 2\delta_{jk}. \quad (2.6)$$

Note, in particular, that these are involutions, i.e.  $\gamma_j^2 = I$ , because  $\{\gamma_j, \gamma_j\} = \gamma_j\gamma_j + \gamma_j\gamma_j = 2\gamma_j\gamma_j = 2I$ . This reflects the fact that, unlike complex fermions, Majorana fermions are their own antiparticles. In what follows, we will mainly work with the latter, as many of the structures of interest to us will have a simplified representation when expressed in terms of Majorana fermions.

### 2.3 Spin systems and spin-fermion mappings

The study of quantum spin systems stems principally from the need to understand the magnetic properties of materials [149]. Mathematically, a single spin- $\frac{1}{2}$  is represented as a vector space  $\mathcal{H} = \text{span}\{|\uparrow\rangle, |\downarrow\rangle\}$ , with the states indicating the direction the spin is pointing. The observables in such a system are given by the Pauli operators

$$X = \begin{bmatrix} 0 & 1 \\ 1 & 0 \end{bmatrix} \quad Y = \begin{bmatrix} 0 & -i \\ i & 0 \end{bmatrix} \quad Z = \begin{bmatrix} 1 & 0 \\ 0 & -1 \end{bmatrix}. \quad (2.7)$$

A system comprised of multiple spins is obtained by taking the tensor product  $\bigotimes_{j=1}^N \mathcal{H}_j$ .

It is often desirable to rewrite a system of spins as a system of fermions e.g. in cases where this leads to a simplified description, as is the case of the Ising model we will review in Section 2.7. A common way to accomplish this correspondence is through the so-called *Jordan-Wigner transformation*. This transformation was first proposed in [91] by Jordan and Wigner and was later used by Lieb, Schultz and Mattis to derive an analytical solution to the XY model in [105]. It can be defined through the assignments

$$\gamma_{2j-1} = \left( \prod_k Z_k \right) X_j, \quad \gamma_{2j} = \left( \prod_k Z_k \right) Y_j. \quad (2.8)$$

For simplicity of notation, we will often represent a string of  $Z$ s stretching between lattice sites  $j$  and  $k$  as  $A_j Z \dots Z B_k$ , where  $A$  and  $B$  are any Pauli matrices. This will take the form  $Z \dots Z A_j$  if the string stretches from the beginning of the lattice up to site  $j$ , and  $B_k Z \dots Z$  it stretches from site  $k$  to the end of the lattice. This string, which features

in (2.8), is usually denoted by a *Jordan string*, and it ensures that the anti-commutation relations (2.2), (2.3) are respected under the Jordan-Wigner transformation. Inverting this transformation, we obtain

$$\begin{aligned} X_j &= (-i)^{j-1} \left( \prod_{k=1}^{2(j-1)} \gamma_k \right) \gamma_{2j-1}, & Y_j &= (-i)^{j-1} \left( \prod_{k=1}^{2(j-1)} \gamma_k \right) \gamma_{2j}, \\ Z_j &= -i\gamma_{2j-1}\gamma_{2j}. \end{aligned} \tag{2.9}$$

As we will see in Section 2.4, quantum Hamiltonians that can be expressed as a sum of pairs of Majorana operators represent a special type of non-interacting fermionic system. It will thus be particularly useful to consider the form these pairs take under the Jordan-Wigner transformation:

$$\begin{aligned} -i\gamma_{2j}\gamma_{2k-1} &= X_j Z \dots Z X_k, & -i\gamma_{2j}\gamma_{2k} &= X_j Z \dots Z Y_k, \\ i\gamma_{2j-1}\gamma_{2k-1} &= Y_j Z \dots Z X_k, & i\gamma_{2j-1}\gamma_{2k} &= Y_j Z \dots Z Y_k, \end{aligned} \tag{2.10}$$

where we assume that  $j < k$ , and that the string of  $Z$ s spans all lattice sites between the Pauli operators with explicit indices.

Note that there is an implicit degree of freedom in the Jordan-Wigner transformation, the *axis of quantisation*, which we have chosen to be in the  $Z$  direction. We could have alternatively chosen this to be e.g. the  $X$  direction, in which case the transformation would take the form

$$\gamma_{2j-1}^X = X \dots X Y_j, \quad \gamma_{2j}^X = X \dots X Z_j. \tag{2.11}$$

This choice of axis will depend on the problem at hand; we see a practical example of this in Section 6.4.

## 2.4 Free-fermionic systems

Amongst all fermionic models, there is a subclass for which the constituent particles do not interact with each other. These systems are said to be *free-fermionic*. Physically, they can represent an idealised system of weakly interacting electrons, and are useful in e.g. producing approximate descriptions of materials via density functional theory [90]

or in the Hartree-Fock approximation to interacting quantum states [51, 74, 177]. They also appear as emerging quasiparticles in descriptions such as the BCS theory of superconductivity [10, 22, 106, 194]. In this section, we introduce the basic structures used in the description of free-fermionic systems and review the properties which will be relevant to us in what follows.

Free-fermionic systems can be written in terms of a quadratic fermionic Hamiltonian (which we abbreviate to “quadratic Hamiltonian”). In terms of Majorana fermions, this Hamiltonian takes the form

$$H = i \sum_{j,k} h_{j,k} \gamma_j \gamma_k, \quad (2.12)$$

where  $h_{j,k}$  is a  $2L \times 2L$  real and antisymmetric matrix by virtue of the relations (2.6). In terms of Dirac fermions, this Hamiltonian takes the form

$$H = \sum_{j,k} A_{jk} a_j^\dagger a_k + B_{jk} a_j^\dagger a_k^\dagger + h.c., \quad (2.13)$$

where  $A$  is a Hermitian matrix and  $B$  is an antisymmetric matrix by virtue of the relations (2.2), (2.3). In what follows, we will mainly work with Majorana fermions, and through an abuse of terminology, we use the terms “quadratic Hamiltonian”, “free-fermionic Hamiltonian” interchangeably to refer both to  $H$  and its corresponding matrix  $h$ . Note that all quadratic Hamiltonians preserve (commute with) the fermionic parity

$$P := \prod_j a_j^\dagger a_j = \prod_j \gamma_{2j-1} \gamma_{2j}, \quad (2.14)$$

which takes the form  $P = \prod_j Z_j$  after applying the Jordan-Wigner transformation (2.8).

A quantum state is an eigenstate of a quadratic Hamiltonian if and only if it is a *fermionic Gaussian state* (FGS), which we sometimes also denote by a “free-fermionic state” or just “free state”. These are the fermionic states that satisfy Wick’s theorem, named after Gian-Luca Wick, who derived it in his work on quantum field theory [85, 208]. Prior to stating it, we must define the *covariance matrix*  $\Gamma$  of a quantum state  $\rho$  as

$$\Gamma_{jk} = \frac{i}{2} \langle [\gamma_j, \gamma_k] \rangle_\rho = \frac{i}{2} \text{tr}(\rho(\gamma_j \gamma_k - \gamma_k \gamma_j)), \quad (2.15)$$

which is real and antisymmetric. If  $\rho$  is defined on  $L$  lattice sites, this matrix will be  $2L \times 2L$ -dimensional. Furthermore, we must introduce the notion of a *Pfaffian*. Given an antisymmetric matrix  $M$ , its Pfaffian is defined as

$$\text{Pf}(M) = \frac{1}{2^L L!} \sum_{\sigma \in S_{2L}} \text{sgn}(\sigma) \prod_{j=1}^L M_{\sigma(2j-1), \sigma(2j)}, \quad (2.16)$$

where  $S_{2L}$  is the permutation group of order  $2L$ , and  $\text{sgn}(\sigma)$  is the sign of the permutation  $\sigma$ <sup>1</sup>. For example, for a  $4 \times 4$  matrix ( $L = 2$ ), the Pfaffian is

$$\text{Pf}(M) = M_{1,2}M_{3,4} - M_{1,3}M_{2,4} + M_{2,3}M_{1,4} \quad (2.17)$$

$$(2.18)$$

**Theorem 1** (Wick). A quantum state  $\rho$  with covariance matrix  $\Gamma$  is a fermionic Gaussian state if and only if

$$\text{tr}(\rho \gamma_1^{s_1} \dots \gamma_{2L}^{s_{2L}}) = i^w \text{Pf}(\Gamma[s_1, \dots, s_{2L}]) \quad (2.19)$$

for all  $s_1, \dots, s_{2L} \in \{0, 1\}$ , where  $\Gamma[s_1, \dots, s_{2L}]$  is the submatrix obtained from  $\Gamma$  such that the  $j$ th row and column are kept if  $s_j = 1$ ,  $2w = \sum_j s_j$ , and  $\text{Pf}$  denotes the Pfaffian of a matrix.

This result implies that FGS are uniquely determined (up to a phase) by their  $2L \times 2L$  covariance matrix. A related structure, expressed in terms of complex fermions, is the *correlation matrix*

$$C := \begin{bmatrix} C^{a^\dagger a} & C^{a^\dagger a^\dagger} \\ C^{aa} & C^{aa^\dagger} \end{bmatrix}, \quad (2.20)$$

$$C_{jk}^{a^\dagger a} = \langle a_j^\dagger a_k \rangle_\rho, \quad C_{jk}^{a^\dagger a^\dagger} = \langle a_j^\dagger a_k^\dagger \rangle_\rho, \quad C^{aa} = -\overline{C^{a^\dagger a^\dagger}}, \quad C^{aa^\dagger} = (I - C^{a^\dagger a})^\dagger.$$

<sup>1</sup>A permutation  $\sigma \in S_n$  is canonically represented as  $(\alpha_1, \dots, \alpha_M)$ , indicating that the object in the  $j$ th position will occupy position  $\alpha_j$  after applying the permutation. Every permutation can be decomposed as a sequence of transpositions, i.e. a sequence of permutation of two objects at a time. The *sign* of the permutation is  $-1$  if this number of transpositions is odd, and  $1$  if this number is even. The sign of a permutation is well-defined, as the parity of the number of transpositions is the same in any such decomposition. For example, take  $\sigma = (2, 3, 4, 1) \in S_4$ . Then,  $\sigma(1) = 2$ ,  $\sigma(2) = 3$ ,  $\sigma(3) = 4$ , and  $\sigma(4) = 1$ . A decomposition of  $\sigma$  in terms of transpositions would be e.g.  $(1, 2)(2, 3)(3, 4)$ , meaning it is an odd permutation and its sign is  $-1$ , and no decompositions of this permutation with an even number of transpositions are possible.

From the above, we conclude that both free-fermionic Hamiltonians and FGS can be efficiently represented, requiring a number of parameters that is quadratic in the size of the system to be specified. Moreover, the quantum dynamics associated to the evolution of a covariance matrix under the action of a quadratic Hamiltonian is efficiently computable [92, 182, 188, 195]. Indeed, if  $h$  is a quadratic Hamiltonian, the evolution of a fermionic Gaussian state  $\rho_0$  represented by covariance matrix  $\Gamma_0$  under the action of  $h$  at time  $t$  is given by

$$\Gamma = \exp(th)\Gamma_0 \exp(-th). \quad (2.21)$$

Likewise, its expectation value with respect to a quadratic Hamiltonian  $h$  can be computed as

$$\text{tr}(\rho H) = \text{tr}(\Gamma h). \quad (2.22)$$

The Hamiltonian (2.12) admits a canonical form akin to a diagonalisation. Since  $h$  is antisymmetric, there exists an orthogonal matrix  $O$  such that [20]

$$h_D = OhO^T = \bigoplus_{j=1}^L \begin{bmatrix} 0 & \epsilon_j \\ -\epsilon_j & 0 \end{bmatrix}. \quad (2.23)$$

Numerically,  $O$  can be obtained by computing the real Schur decomposition of  $h$  [43]. This allows us to write  $H$  as

$$H = i \sum_{j=1}^L \epsilon_j \tilde{\gamma}_{2j-1} \tilde{\gamma}_{2j} = \sum_{j=1}^L \epsilon_j \tilde{a}_j^\dagger \tilde{a}_j, \quad (2.24)$$

where

$$\begin{bmatrix} \tilde{\gamma}_1 \\ \vdots \\ \tilde{\gamma}_{2L} \end{bmatrix} = O^T \begin{bmatrix} \gamma_1 \\ \vdots \\ \gamma_{2L} \end{bmatrix}, \quad (2.25)$$

and the  $\epsilon_j$  are *single-particle energies* in this new basis. The eigenvalues  $\lambda_j$  of  $H$ ,

indexed in ascending order, are given in a combinatorial manner as

$$\lambda_j = \sum_{k=1}^L b_k(j) \epsilon_j, \quad (2.26)$$

where  $b_k(j)$  is the  $k$ th digit of the binary representation of  $j$  (and thus is either zero or one), and where the  $\epsilon_k$  are assumed to be ordered in ascending order. The eigenvectors of the quadratic Hamiltonian can also be obtained. Define

$$V_j := \bigoplus_{k=1}^L \begin{bmatrix} 0 & (-1)^{b_k(j)+1} \\ (-1)^{b_k(j)} & 0 \end{bmatrix}. \quad (2.27)$$

Then, the covariance matrix  $\Gamma^j$  of the  $j$ th eigenvector of  $H$  can be computed as

$$\Gamma^j = O^T V_j O. \quad (2.28)$$

Finally, the overlap between two pure FGS  $|\psi\rangle$  and  $|\phi\rangle$  with the same parity  $p$ , represented by covariance matrices  $\Gamma_1$  and  $\Gamma_2$  is given by [24, 170]

$$|\langle\psi|\phi\rangle|^2 = p2^{-L} \text{Pf}(\Gamma_1 + \Gamma_2). \quad (2.29)$$

The symmetries of a free-fermionic system have a direct influence on the structures we have just introduced. A covariance matrix represents a translationally invariant FGS  $\rho$ , and  $h_{j,k}$  defines a translationally invariant quadratic Hamiltonian if and only if, respectively:

$$\Gamma_{jk} = \Gamma_{j+2m, k+2m}, \quad h_{j,k} = h_{j+2m, k+2m}, \quad (2.30)$$

for all integers  $m$ , where it is understood that coefficients are taken modulo the lattice size. A covariance matrix represents a lattice inversion symmetric FGS  $\rho$ , and  $h_{j,k}$  defines a lattice inversion symmetric quadratic Hamiltonian, if and only if, respectively:

$$\Gamma_{jk} = (-1)^{j-k+1} \Gamma_{L-k+1, L-j+1}, \quad h_{j,k} = (-1)^{j-k+1} h_{L-k+1, L-j+1}. \quad (2.31)$$

We denote by ‘‘symmetric FGS’’ and ‘‘symmetric quadratic Hamiltonians’’ those that are invariant both under translation and lattice inversion. This terminology will be

useful in Chapter 3 when studying the expressibility of certain variational quantum algorithms.

## 2.5 Entanglement in many-body systems

Let  $\mathcal{L}$  be a set of points forming a lattice, as described in Section 2.1, and let  $A, B \subseteq \mathcal{L}$  be a bipartition of the lattice e.g.  $A \cap B = \emptyset$  and  $A \cup B = \mathcal{L}$ . If  $|\psi\rangle$  is a pure quantum state of a system on this lattice, each subsystem  $A$  and  $B$  is described by a mixed quantum state characterised by a *reduced density matrix* computed from  $|\psi\rangle\langle\psi|$  by taking a partial trace with respect to the other subsystem. For instance, the reduced density matrix of subsystem  $A$  is given by

$$\rho_A = \text{tr}_B(|\psi\rangle\langle\psi|) = \sum_{\phi_B} \langle\phi_B|\psi\rangle\langle\psi|\phi_B\rangle, \quad (2.32)$$

where the  $|\phi_B\rangle$  form a basis for the vector space of  $B$  (i.e. the vector space for which the tensor product is taken only over the lattice sites contained in  $B$ )<sup>1</sup>. Note that, by abuse of notation and terminology, we refer to a mixed quantum state and its corresponding density matrix interchangeably. A practical way to compute a partial trace of  $|\psi\rangle\langle\psi|$  is through a *Schmidt decomposition*. We begin by writing the state  $|\psi\rangle$  as

$$|\psi\rangle = \sum_{j,k} M_{j,k} |\psi_j^A\rangle \otimes |\psi_k^B\rangle, \quad (2.34)$$

where the  $|\psi_j^A\rangle$  form a basis for the vector space of  $A$ , and  $|\psi_k^B\rangle$  form a basis for the vector space of  $B$ . Then, one can perform a singular value decomposition on  $M$  to obtain  $M = UDV^T$ , where  $U$  is unitary,  $D$  is diagonal and  $V^T$  is orthonormal. By performing a change of basis on each subsystem  $|\phi_j^A\rangle = \sum_l U_{j,l} |\psi_l^A\rangle$  and  $|\phi_k^B\rangle = \sum_l V_{k,l} |\psi_l^B\rangle$ ,  $|\psi\rangle$  can be written as

$$|\psi\rangle = \sum_j \lambda_j |\phi_j^A\rangle \otimes |\phi_j^B\rangle, \quad (2.35)$$

---

<sup>1</sup>To be explicit, the inner product in (2.32) is computed only over the degrees of freedom of  $B$  e.g. if  $|\psi_A\rangle$  is in the vector space of  $A$  and  $|\psi_B\rangle, |\phi_B\rangle$  in the vector space of  $B$ , then

$$\langle\phi_B|\psi_A \otimes \psi_B\rangle\langle\psi_A \otimes \psi_B|\phi_B\rangle = |\langle\psi_B|\phi_B\rangle|^2 |\psi_A\rangle\langle\psi_A| \quad (2.33)$$

where the  $\lambda_j$  are the diagonal entries of  $D$ . The partial trace (2.32) can then be directly obtained as

$$\rho_A = \sum_j |\lambda_j|^2 |\phi_j^A\rangle\langle\phi_j^A|, \quad (2.36)$$

where the  $\rho_j := |\lambda_j|^2$  form the spectrum of the reduced density matrix, also called the *entanglement spectrum* [41]. It characterises the entanglement of the quantum state across the bipartition, and the celebrated *von Neumann entropy* (VNE) can be computed directly from it

$$S_{\text{VN}} := -\text{tr}(\rho_A \ln \rho_A) = -\text{tr}(\rho_B \ln \rho_B) = -\sum_j \rho_j \ln \rho_j. \quad (2.37)$$

From here on, we will drop the index indicating the subsystem, assuming it to be implicit.

Since a density matrix is always positive semidefinite, its logarithm is well-defined, and  $\rho$  can be written in terms of its *entanglement Hamiltonian* [41, 103] (also known as *modular Hamiltonian*) as

$$\rho = e^{-H_{\text{ent}}} \quad H_{\text{ent}} = -\log \rho. \quad (2.38)$$

This can be interpreted as the Boltzmann-Gibbs density matrix of a system in thermal equilibrium at a temperature  $\beta = 1$ . Surprisingly, in certain circumstances, the entanglement Hamiltonian of a reduced density matrix turns out to be local and few-body, despite no such condition being a priori imposed. This is, for example, the case of certain integrable models which we will discuss later in this section, or of a system of free-fermions hopping on a lattice. In fact, the reduced density matrix of the ground state of a free-fermionic system can be written in the form [34, 35, 155]

$$H_{\text{ent}} = \sum_{j,k} A_{jk} a_j^\dagger a_k \quad (2.39)$$

Moreover, it is the case that

$$A = \ln \frac{1 - C^{a^\dagger a}}{C^{a^\dagger a}}, \quad (2.40)$$

## 2.5 Entanglement in many-body systems

---

and the eigenvalues  $\zeta_k$  of  $C$  satisfy the relation

$$\zeta_k = \frac{1}{e^{\epsilon_k} + 1}, \quad (2.41)$$

where  $\epsilon_k$  are the single-particle energies of  $H_{\text{ent}}$ .

For a general fermionic system, these expressions no longer hold, but the entanglement Hamiltonian can be written in a diagonal form as follows

$$H_{\text{ent}} = E_0 + \sum_j \epsilon_j d_j^\dagger d_j + \sum_{j,k} \epsilon_{jk} d_j^\dagger d_j d_k^\dagger d_k + \dots, \quad (2.42)$$

where  $\epsilon_j$  are the single particle energies,  $\epsilon_{jk}$  are the two particle energies of the entanglement Hamiltonian, and so forth. This directly follows from the diagonalisation of  $\rho$ . If  $\rho_k$  is the associated entanglement spectrum in descending order, then, recursively,

$$\epsilon_{\mathcal{S}} = -\ln \rho \left( \sum_{j \in \mathcal{S}} 2^{j-1} \right) - \sum_{\mathcal{R} \subset \mathcal{S}} \epsilon_{\mathcal{R}}, \quad (2.43)$$

where  $\mathcal{S}$  is a set comprised of the site indices for that energy; for instance,  $\epsilon_{12} = -\ln \rho_3 + \ln \rho_2 + \ln \rho_1 - \ln \rho_0$ . Note that we take  $E_0 = -\ln \rho_0$ , and we assume summing over an empty set yields zero. The  $d_j$  are connected to the operators  $a_j$  by conjugation by the diagonalising unitary  $U$ . This contrasts with the free-fermionic case, where all energies other than the single particle energies vanish, and the operators featuring in the entanglement Hamiltonian (2.39) are the operators  $a_j$  associated with each lattice site.

For certain integrable systems, such as the XYZ model, which we will explore in Chapter 6, or the Ising model, which we introduce in Section 2.7, analytical expressions for the entanglement Hamiltonian can be obtained in the thermodynamic limit. This is done by considering their connection to a corresponding 2D classical spin model [136, 137, 186]. In these cases, the Hamiltonian of the quantum 1D model commutes with the transfer matrix  $T$  of the 2D classical model, and the ground state  $|\psi\rangle$  is the largest energy eigenstate of  $T$ . Under such conditions, the reduced density matrix of  $|\psi\rangle$  with respect to a bipartition of the lattice can be seen as the partition function of the aforementioned 2D model, and can be computed as

$$\rho = ABCD, \quad (2.44)$$

where  $A, B, C, D$  are the so-called *corner transfer matrices* (CTMs) of the model [12].

## 2.6 Interaction distance

As established in Section 2.4, free-fermionic systems admit efficient representations in terms of covariance matrices and quadratic Hamiltonians. This description breaks down in most physical systems, where interactions lead to exotic phenomena such as fractionalised excitations and topological order [2, 102]. At the same time, there are many known examples, e.g., Luttinger liquids [66], where interactions give rise to new collective degrees of freedom which can still be described as nearly free. It is thus important to have a systematic understanding of the criteria characterising when a system admits a free-fermionic description. Here, we review a quantity called *interaction distance* [147, 150, 192], which aims to quantify how far from being free-fermionic a quantum state is. Given some density matrix  $\rho$ , the interaction distance [192] of  $\rho$  is defined as

$$D_{\mathcal{F}}(\rho) := \min_{\sigma \in \mathcal{F}} \frac{1}{2} \operatorname{tr} \left( \sqrt{(\rho - \sigma)^2} \right), \quad (2.45)$$

where  $\mathcal{F}$  is the manifold

$$\mathcal{F} := \left\{ \sigma = \frac{1}{Z} e^{-H}, Z = \operatorname{tr} e^{-H}, H \text{ is quadratic} \right\}. \quad (2.46)$$

Note that, importantly, there is no restriction placed on the quadratic Hamiltonians in (2.46), and these may be defined in terms of fermionic operators that are different from the  $a_j$  associated to the lattice sites. In Section 5.1, we examine the interaction distance across the phase diagram of several models, and leverage this quantity to measure the success of variational quantum algorithms in preparing the corresponding ground states. Furthermore, in Chapter 6, we study the interaction distance in the context of the XYZ model, and explore ways to compute it directly in terms of physical observables.

There is a crucial simplification in evaluating  $D_{\mathcal{F}}$  as written in Eq. (2.45), which was shown in [192] leveraging a result from [112]. The minimisation over  $\mathcal{F}$  is equivalent to

$$D_{\mathcal{F}}(\rho) = \min_{\epsilon} \frac{1}{2} \sum_k |\rho_k - \sigma_k(\epsilon)|, \quad (2.47)$$

where the  $\rho_k$  denote the eigenvalues of  $\rho$  in descending order (normalised such that  $\sum_k \rho_k = 1$ ), and

$$\sigma_k(\boldsymbol{\epsilon}) = \frac{1}{Z} e^{-\sum_j \epsilon_j b_k(j)}, \quad (2.48)$$

where, as in (2.26),  $b_k(j)$  is the  $k$ th digit of the binary representation of  $j$  (and thus is either zero or one). The normalisation  $Z$  ensures that  $\sum_k \sigma_k = 1$ , and we assume that  $\sigma_k$  are in the same (descending) order as  $\rho_k$ , which is necessary to achieve a minimum in Eq. (2.47) [112]. Note that the number of modes  $\{\epsilon_j\}$  does not have to be such that the length of the spectra match; in that case, the smaller spectrum is implicitly padded with zeros.

The utility of Eq. (2.47) is that the value of  $D_{\mathcal{F}}(\rho)$  can be determined solely from the information in the entanglement spectrum. Comparing Eq. (2.45) with Eq. (2.47), we see that the minimisation over all matrices  $\sigma \in \mathcal{F}$  was traded for a minimisation over scalars  $\{\epsilon_j\}$ . The latter is a much simpler optimisation problem, and the number of parameters scales linearly with the system size. Thus, the problem becomes numerically tractable, as the computational complexity is only polynomial in system size  $N$  once the spectrum  $\{\rho_k\}$  is known [192]. Obtaining this spectrum efficiently is possible in many relevant cases through, e.g., the DMRG algorithm, which we review later in Section 6.2.

We now summarise how Eq. (2.48) is minimised, as described in [192]. The optimisation routine starts by heuristically choosing an initial guess for the single-particle modes, which fixes the number of modes that will be used throughout the optimisation, in the following way:

1. The candidate normalisation energy  $E_0 = \ln Z$  is chosen to be the lowest element in  $\{-\log \rho_k\}$ , and removed from this set.
2. The first single-particle energy candidate  $\epsilon_1$  is picked as the lowest level in the remaining spectrum, and the closest level to  $E_0 + \epsilon_1$  is removed.
3. The next energy  $\epsilon_2$  is picked, again as the lowest level in the remaining spectrum, and the closest levels to  $E_0 + \epsilon_1 \epsilon_2$  and  $E_0 + \epsilon_2$  are removed.
4. The next energy  $\epsilon_3$  is similarly picked, and the closest levels to  $E_0 + \epsilon_3$ ,  $E_0 + \epsilon_1 \epsilon_3$ ,  $E_0 + \epsilon_2 \epsilon_3$  and  $E_0 + \epsilon_1 \epsilon_2 \epsilon_3$  are removed.

5. This process repeats until the initial spectrum  $\{-\log \rho_k\}$  is either exhausted or the remaining levels fall below some specified precision.

When evaluating which levels are closest to a newly generated one, a threshold is used; if no level is below a certain distance to the new one, no levels are removed. After this initial guess is constructed, a nonlinear optimisation routine having Eq. (2.47) as the cost function is run. Since this optimisation presents with local minima, a global optimisation routine is employed. The algorithm chosen for this was a basinhopping optimisation [192, 201] procedure. This routine runs a local optimisation, stochastically perturbs the minimum found, and then again runs a local optimisation using this perturbed minimum as the initial guess. This is repeated a set number of times, and a candidate for a global minimum is returned. The local optimisation routine used is the Nelder-Mead gradient-free optimisation algorithm.

Note that  $D_{\mathcal{F}}$  is strictly bounded  $0 \leq D_{\mathcal{F}} \leq 1$  [122], and states that have  $D_{\mathcal{F}} = 0$  can be expressed as Gaussian states in terms of some fermionic modes as in Eq. (2.48). This is, of course, true for product states in the computational basis, but it is also the case for certain entangled states such as the ground state of the Ising model in the transverse field [192]. Interestingly, unlike its lower bound,  $D_{\mathcal{F}}$  does not seem to saturate its upper bound – it was conjectured that  $D_{\mathcal{F}} \leq 3 - 2\sqrt{2}$  [122]. Physical states that realize this upper bound of  $D_{\mathcal{F}}$  were identified as ground states of certain types of parafermion chains [122]. These states do not have a particularly high value of VNE, but the structure of their entanglement spectrum is as distinct as possible from that of free-fermions, in the sense of Eq. (2.47). This structure is that of a "flat" entanglement spectrum, with  $\rho_k = 1/N$ , where  $N$  is the dimension of the single-particle vector space. For  $N = 3$ , this corresponds to  $(1/3, 1/3, 1/3)$  with  $D_{\mathcal{F}}(\rho) = \frac{1}{6}$ , and it was proved analytically in the Supplementary Material to [192] that this maximises the interaction distance amongst all 4-level spectra (where a zero is added to the spectrum for padding). In general, the interaction distance for these spectra was conjectured to be  $3 - \frac{N}{2^n} - \frac{2^{n+1}}{N}$ , where  $n$  is the highest integer such that  $2^n < N$ ; when  $N$  tends to infinity, this converges to  $3 - 2\sqrt{2}$  [122].

The interaction distance of a state  $\rho$  bounds the difference between the expectation values of any observable with respect to  $\rho$  and  $\sigma$ , where  $\sigma$  is the state that minimises

Eq. 2.45. Indeed, it is the case that [151]

$$|\langle O \rangle_\rho - \langle O \rangle_\sigma| = |\text{tr}(O(\rho - \sigma))| \quad (2.49)$$

$$= \left| \sum_k \langle \phi_k | O | \phi_k \rangle \phi_k \right| \quad (2.50)$$

$$\leq \left| \max_k \langle \phi_k | O | \phi_k \rangle \sum_k \phi_k \right| \quad (2.51)$$

$$= \|O\|_\infty \left| \sum_k \phi_k \right| \quad (2.52)$$

$$= \|O\|_\infty \text{tr} |\rho - \sigma| \quad (2.53)$$

$$= \|O\|_\infty 2D_{\mathcal{F}}(\rho), \quad (2.54)$$

where in step (2.50) we made use of the fact that  $\rho, \sigma$  are mutually diagonal, and assumed  $|\phi_k\rangle$  to be a common eigenbasis (with  $\phi_k = \rho_k - \sigma_k$ , where  $\rho_k, \sigma_k$  are the eigenvalues of  $\rho, \sigma$ ). In step (2.53) we used the definition of the trace distance, and in step (2.54) we used the definition of the interaction distance. We will make use of this bound in Section 6.4, where we study a link between the interaction distance and a measure of the interactions of a system based on Wick's theorem.

In [192], it is argued, based on results from [103], that the interaction distance can diagnose whether the system admits a description in terms of free quasiparticles. Quasiparticles are elementary excitations which can capture the low-energy behaviour of a condensed matter system in terms of an effective description. Their use has been successful in describing the low-energy behaviour of systems such as liquid helium [59, 60, 98], the fractional quantum Hall effect [67] and the AKLT [6] spin chain.

## 2.7 Example: The Ising model

The quantum Ising model is a well-known, paradigmatic spin model in condensed matter physics [50]. Its Hamiltonian can be written as

$$H = -J \sum_{j=1}^L X_j X_{j+1} - h_z \sum_{j=1}^L Z_j - h_x \sum_{j=1}^L X_j, \quad (2.55)$$

where we consider the presence of both a transverse field, controlled by the parameter  $h_z$ , and a longitudinal field, controlled by the parameter  $h_x$ . The  $J$  parameter is a coupling defining the energy scale, which we will set to  $\pm 1$ . The properties of the ground state of this model are insensitive to the sign of  $J$  in the absence of the longitudinal field. However, once  $h_x \neq 0$ , the phase diagram is substantially different for the two models. On the one hand, when  $J = 1$ , the model is ferromagnetic, possessing a single critical point at  $(h_z = 1, h_x = 0)$  described by the free Ising conformal field theory [63] for which the entanglement entropy of the ground state diverges logarithmically with system size [27]. On the other hand, when  $J = -1$ , the model is antiferromagnetic, and has a critical line connecting the point  $(h_z, h_x) = (1, 0)$  with the point  $(h_z, h_x) = (0, 2)$ . This critical line is not known analytically, but it has been determined numerically using density-matrix renormalization group simulations in Ref. [146]. The Ising model in Eq. (2.55) serves as a useful laboratory for studying a number of phenomena in condensed matter physics [36, 50, 129]. In Section 5.1.1, we study the interaction distance, introduced in Section 2.6, across the phase diagram of this model.

The limit of the purely transverse field ( $h_x = 0$ ) is particularly important. Along this line, both models are equivalent, and the Hamiltonian is quadratic when written in terms of Majorana operators introduced in Section 2.4 after performing the Jordan-Wigner transformation [159]. Indeed, applying this transformation to (2.55), we obtain

$$H = i \sum_{j=1}^N J \gamma_{2j-1} \gamma_{2j} + i h_z \sum_{j=1}^N \gamma_{2j} \gamma_{2j+1} - h_x \sum_{j=1}^N (-i)^{j-1} \left( \prod_{k=1}^{2(j-1)} \gamma_k \right) \gamma_{2j+1}. \quad (2.56)$$

The longitudinal field term attached to the  $h_x$  parameter is highly non-local under this transformation, while the remaining terms are quadratic in the Majorana operator basis, thus corresponding to a free-fermionic system in this representation when  $h_x = 0$ .

In that case, the model can be written in the form (2.12), with

$$h = \begin{bmatrix} 0 & J & \dots & \dots & & & 0 \\ -J & 0 & h_z & & & & \\ & -h_z & 0 & J & & & \\ \vdots & & -J & 0 & h_z & & \vdots \\ & & & -h_z & 0 & \ddots & \\ \vdots & & & & \ddots & \ddots & \vdots \\ & & & & & 0 & h_z \\ & & & & & -h_z & 0 & J \\ 0 & & \dots & \dots & & -J & 0 \end{bmatrix}. \quad (2.57)$$

Using this representation, following Section 2.4, the Ising model can be numerically efficiently diagonalised and its eigenenergies obtained. For the case of this model, however, it is well known that this entire process can be performed analytically [105, 182]. To this end, one typically expresses (2.55) (where, again, we are considering  $h_x = 0$ ) in a fermionic basis to obtain

$$H = \sum_{j=1}^{L-1} J(a_{j+1}^\dagger a_j^\dagger + a_j a_{j+1} - a_j^\dagger a_{j+1} - a_{j+1}^\dagger a_j) - \sum_{j=1}^L h_z (2a_j^\dagger a_j - 1), \quad (2.58)$$

where we impose OBCs for simplicity (the PBC case is similar with some additional bookkeeping). Applying a discrete Fourier transformation, we obtain the transformed operators

$$f_k = \sum_{j=1}^L a_j e^{-ikj} / \sqrt{N}, \quad (2.59)$$

where  $k = \frac{2n\pi}{L}$ , with  $n$  running over  $N$  integer values such that  $k \in [-\pi, \pi]$ . This yields

$$H = \sum_{k>0} \begin{bmatrix} f_k^\dagger & f_k \end{bmatrix} \begin{bmatrix} -J \cos(k) - h_z & iJ \sin(k) \\ -iJ \sin(k) & J \cos(k) + h_z \end{bmatrix} \begin{bmatrix} f_k^\dagger \\ f_k \end{bmatrix}. \quad (2.60)$$

The quadratic Hamiltonian is now in block-diagonal form with  $2 \times 2$  blocks, and can

## 2.7 Example: The Ising model

---

be directly diagonalised (this is called a *Bogoliubov transformation* [22]) to yield

$$H = \sum_{k>0} \omega_k (d_k^\dagger d_k + d_{-k}^\dagger d_{-k} - 1), \quad (2.61)$$

with

$$\omega_k = 2\sqrt{h_z^2 + J^2 + 2h_z J \cos(k)}. \quad (2.62)$$

As we mentioned in Section 2.5, the reduced density matrix and corresponding entanglement Hamiltonian can be determined for certain integrable models by considering a connection to a corresponding 2D classical spin model. This is the case of the transverse-field Ising model, for which the Hamiltonian can be connected to the transfer matrix of the 6-vertex model. The entanglement Hamiltonian then takes the form [156, 191]

$$H = \begin{cases} -2I(k') \sum_{j=1}^{\infty} [jX_j X_{j+1} + k(j - \frac{1}{2}Z_j)], & h_z > J, \\ -2I(k') \sum_{j=1}^{\infty} [jkX_j X_{j+1} + (j - \frac{1}{2}Z_j)], & h_z < J, \end{cases} \quad (2.63)$$

where  $I(k')$  is the complete elliptic integral of the first kind and  $k = \min(J/h_z, h_z/J)$ ,  $k' = \sqrt{1 - k^2}$ .

We will employ the transverse field Ising model in Chapter 4, where we extensively study free-fermionic models in the context of variational quantum algorithms. The longitudinal field is reintroduced in Chapter 5, where we extend this analysis to non-integrable models.

---

# CHAPTER 3

---

The expressibility of Variational Quantum  
Algorithms

---

In recent years, variational quantum algorithms have attracted much attention [30, 58, 154, 189]. A common feature of these algorithms is that they involve optimising a set of parameters defining a family of quantum circuits to prepare a quantum state of interest. We begin this chapter by presenting a brief overview of VQAs in Section 3.1.

Successfully employing these parameterised circuits requires an adequate level of *expressibility*, which is determined by the set of quantum states that they can prepare. While universal parameterised circuits exist [18, 128], these are typically difficult or impossible to optimise [80]. A way to constrain the expressibility of a parameterised circuit is to employ *problem-tailored ansätze* [100, 210]. Among them is the Quantum Approximate Optimisation Algorithm (QAOA), originally proposed for solving combinatorial optimisation problems such as the MaxCut problem [58].

In this chapter, we study the expressibility of parameterised circuits from the point of view of Lie theory, a powerful tool already used in the study of quantum control [38] and which has recently been applied to VQAs [99–101, 124, 128]. Our contributions correspond to the sections not marked as “Background” (or subsections of those sections), and can be summarised as follows:

- In Section 3.2.2, we show that the states that can be prepared by a parameterised circuit are precisely the ground states of the Hamiltonians that belong to its Lie algebra. We also point out that there is a redundancy in the unitaries that can prepare a given state, and that this redundancy is characterised by a stabiliser Gauge group.
- In Section 3.3, we consider the original QAOA proposed in [58] and of a variation on it with decoupled parameters proposed in [77]. We derive a basis for the Lie algebra of both on a 1D lattice. We also derive a basis for the generators of the associated stabiliser Gauge groups.
- Using the above Lie algebra bases, we conclude that the QAOA on a 1D lattice can prepare precisely all fermionic Gaussian states which have a reflection symmetry (for the OBC case) or both a reflection and translation symmetries (for the PBC case). When the angles are decoupled, any FGS can be prepared. No other states beyond those mentioned can be prepared by the corresponding parameterised circuit.

We exploit the results above in Chapter 4 to conduct a comprehensive numer-

ical study of the factors influencing optimisation hardness in variational quantum algorithms.

### 3.1 Background: Variational Quantum Algorithms

In this section, we offer a brief introduction to variational quantum algorithms. Variational Quantum Algorithms (VQAs) [16, 30] are generally formulated as a feedback loop between an optimisation routine running on a classical computer and a quantum simulator. This routine manipulates a set of controllable parameters defining a family of quantum circuits, with the objective of finding a circuit that is able to prepare a quantum state of interest. A sketch of the variational protocol is given in Fig. 3.1. Given an initial state  $|\psi(0)\rangle$  and a set of parameters  $\boldsymbol{\theta}$ , this circuit prepares the state

$$|\psi(\boldsymbol{\theta})\rangle = U(\boldsymbol{\theta}) |\psi(0)\rangle. \tag{3.1}$$

The specific form that  $U(\boldsymbol{\theta})$  takes is determined by an ansatz; in Section 3.1.1, we give an overview of the most commonly used ansätze in the literature. The goal, as outlined above, is to employ a classical optimisation routine in order to find a set of angles  $\boldsymbol{\theta}^*$ , such that  $|\psi(\boldsymbol{\theta}^*)\rangle$  is a quantum state of interest, which we call a *target state*. This is done by supplying the optimiser with a cost function which measures a distance between the prepared state and a target state. An example is the expectation value of the energy

$$E(\boldsymbol{\theta}) := \frac{\langle \psi(\boldsymbol{\theta}) | H | \psi(\boldsymbol{\theta}) \rangle}{\langle \psi(\boldsymbol{\theta}) | \psi(\boldsymbol{\theta}) \rangle}, \tag{3.2}$$

where  $H$  is a Hamiltonian having a target state as its ground state. Once the value of the cost function is measured, it is passed back to the optimisation algorithm running on the classical computer. This algorithm returns a new set of angles, which are passed again to the quantum simulator, and the process repeats itself until the optimisation algorithm running on the classical computer halts. It must be the case that

$$\min_{\boldsymbol{\theta}} E(\boldsymbol{\theta}) \geq E_0,$$

where  $E_0$  is the ground state energy of  $H$  in Eq. (3.2). Equality is achieved for a set of parameters  $\boldsymbol{\theta}^*$  if and only if  $|\psi(\boldsymbol{\theta}^*)\rangle$  is a ground state of  $H$ .

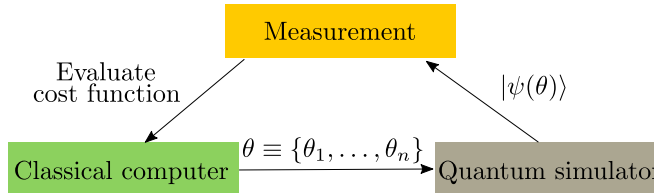


Figure 3.1: A schematic illustrating a variational quantum-classical optimisation routine. The optimisation involves  $n$  parameters  $\theta_j$ , where  $j = 1, 2, \dots, n$ . For the ansatz in Eq. (3.22),  $n = pm$ .

### 3.1.1 Brief summary of different types of VQA

We now briefly summarise the most commonly used VQAs. Our intention is to give a brief overview of the main types of VQA found in the literature, and not to offer a comprehensive review. All VQAs we present here follow the general form 3.1, and mainly differ in the choice of  $U(\theta)$  and of initial state  $|\psi(0)\rangle$ .

#### Quantum Approximate Optimisation Algorithm

A well-known variational algorithm is the Quantum Approximate Optimisation Algorithm (QAOA), designed to tackle combinatorial optimisation problems [58]. Typically, one begins by considering a classical spin Hamiltonian  $H(s_1, \dots, s_n)$  such that a solution to the problem is represented by a spin assignment that minimises the energy; several important NP-hard problems can be written in this form [108]. Given this formulation, we are able to obtain a quantum Hamiltonian by replacing the spin variables  $s_j$  by Pauli operators  $Z_j$ , yielding  $H(Z_1, \dots, Z_n)$ . Solving the original problem is now equivalent to finding the ground state of this Hamiltonian. We exemplify this following the original QAOA proposal [58], where the MaxCut problem is considered. Given a graph  $G$  with edges  $E$ , the MaxCut problem asks for a partition of this graph into two disjoint groups of vertices such that the number of edges between the groups is as large as possible. This can be translated into finding a spin configuration that maximises the classical Hamiltonian

$$\tilde{H} = \frac{1}{2} \sum_{(j,k) \in E} (1 - s_j s_k), \tag{3.3}$$

### 3.1 Background: Variational Quantum Algorithms

---

where  $s_j, s_k$  assume values 1 or  $-1$  depending on which partition the vertices  $j, k$  were assigned to. This, in turn, is equivalent to the problem of minimising the Hamiltonian  $\sum_{(j,k) \in E} s_k s_j$ , which translates into finding a ground state of the quantum Hamiltonian

$$H = \sum_{(j,k) \in E} Z_j Z_k. \quad (3.4)$$

The variational procedure then attempts to find a solution of the problem by minimising the cost function (3.2) featuring this Hamiltonian. The parameterised circuit used for this purpose consists in alternating the problem Hamiltonian  $H_B = H$  with a “mixer” Hamiltonian  $H_A$  such that

$$U(\boldsymbol{\theta}) = \exp(-i\theta_{p,1}H_A) \exp(-i\theta_{p,2}H_B) \dots \exp(-i\theta_{1,1}H_A) \exp(-i\theta_{1,2}H_B), \quad (3.5)$$

where

$$H_A = \sum_{j \in G} X_j, \quad (3.6)$$

$$H_B = H. \quad (3.7)$$

The initial state in this case is taken to be an  $X$ -polarised state  $|\psi(0)\rangle = |\rightarrow \dots \rightarrow\rangle$ , which represents a superposition of all possible solutions to the problem. In Section 3.3, we fully characterise the quantum states that the parameterised circuit (3.5) can produce in one dimension, i.e., when the graph  $G$  is such that the vertices are either arranged linearly or in a cycle.

#### Hamiltonian Variational Ansatz

A variational algorithm that is closely related to QAOA is the Hamiltonian Variational Ansatz (HVA) [204, 210]. It starts by choosing a splitting of the Hamiltonian  $H$  for which we want to prepare the ground state as

$$H = \sum_{j=1}^m H_j, \quad (3.8)$$

### 3.1 Background: Variational Quantum Algorithms

---

where  $[H_j, H_k] \neq 0$  for any  $j, k \in \{1, \dots, m\}$ . The parameterised circuit employed in the HVA then takes the form

$$U(\boldsymbol{\theta}) = \exp(-i\theta_{p,m}H_m)\dots \exp(-i\theta_{p,1}H_1)\dots \exp(-i\theta_{1,m}H_m)\dots \exp(-i\theta_{1,1}H_1). \quad (3.9)$$

and the initial state is taken to be the ground state of one of the  $H_j$ . This ansatz is often used in the preparation of ground states of quantum condensed matter systems [78, 79, 210]; we will employ it to prepare the ground state of several non-integrable models in Chapter 5.

#### Variational Quantum Eigensolver

The Variational Quantum Eigensolver (VQE) was one of the first variational algorithms to be proposed, and was designed to tackle quantum chemistry problems [120, 154]. The ansatz for  $U(\boldsymbol{\theta})$  is typically the so-called *Unitary Coupled Cluster (UCC)* ansatz [4]. It starts by choosing the initial state  $|\psi(0)\rangle$  to be a Hartree-Fock approximation of the target state, and then considers corrections to it which take the form

$$T(\mathbf{t}) = \sum_{jk} t_{jk} a_j^\dagger a_k + \sum_{jklm} t_{jklm} a_j^\dagger a_l^\dagger a_k a_m + \dots \quad (3.10)$$

It then includes the Hermitian conjugate terms  $T(\mathbf{t})^\dagger$  to form the operator  $T(\mathbf{t}) - T(\mathbf{t})^\dagger$ , which is anti-Hermitian [154], so that the exponentiation

$$U(\mathbf{t}) = \exp\left(T(\mathbf{t}) - T(\mathbf{t})^\dagger\right) \quad (3.11)$$

is unitary. By trotterising and using a mapping from fermions to qubits (see Section 2.3) the parameterised circuit takes the form

$$U(\mathbf{t}) = \left( \prod_j e^{(it_j/p)P_j} \right)^p, \quad (3.12)$$

where  $p$  controls both the depth of the circuit and the accuracy of the approximation, and  $P_j$  are tensor products of Pauli matrices resulting from the fermion to spin transformation applied to the terms of (3.10). Note that we have grouped all the indices appearing in Eq. (3.10) into a single index  $j$ .

#### Hardware Efficient Ansatz

The parameterised quantum circuits we introduced so far are called “problem-inspired ansätze”, as their design is rooted in the problem they are tailored to solve. In contrast, a “hardware efficient ansatz” [93] (HEA) is designed taking into account a specific quantum hardware implementation, and aims to reduce the circuit depth as much as possible. These parameterised circuits are “problem-agnostic”, and must be expressive enough to find a solution without directly considering information about the problem. This leads to the presence of barren plateaus (see Section 3.1.3), and represents an obstacle to their practical applicability. A HEA generally takes the form

$$U(\boldsymbol{\theta}) = \prod_{j=1}^p \prod_{k=1}^L \left( U^{j,k}(\theta_{j,k}) U_{\text{ENT}} \right), \quad (3.13)$$

where  $U^{j,k}$  are single-qubit rotations at depth  $j$  and acting on qubit  $k$ , which are alternated with non-parameterised entangling gates  $U_{\text{ENT}}$  e.g. C-Phase gates.

#### 3.1.2 Connecting VQAs to Adiabatic State Preparation

The variational algorithms introduced above, except the HEA, can be directly motivated and understood through the lens of adiabatic quantum state preparation [57, 58, 210]. In adiabatic state preparation, an easy to prepare initial state  $|\psi(0)\rangle$  is evolved under the continuous action of a time-dependent Hamiltonian that interpolates an initial Hamiltonian  $H_A$  and a final Hamiltonian  $H_B$ . The initial Hamiltonian has  $|\psi(0)\rangle$  as its ground state, while the final Hamiltonian has the desired state as its ground state. This interpolation is written as

$$H(s(t)) = (1 - s(t))H_A + s(t)H_B, \quad (3.14)$$

where  $s(t)$  is a *schedule* satisfying  $s(0) = 0, s(1) = 1$ . A well-known limitation of adiabatic state preparation is that the schedule must slow down considerably as the energy gap between the ground state as the first excited state decreases to avoid Landau-Zehner transitions [9] to excited states. It has been suggested that variational quantum algorithms can overcome this limitation [215], motivating their use. Moreover, Pontryagin’s Minimum Principle has been used to argue that a “bang-bang” structure (i.e. where one alternates between a finite set of Hamiltonians as in the variational al-

---

### 3.1 Background: Variational Quantum Algorithms

gorithms above) is optimal for state preparation [212], as opposed to the continuous time-dependent evolution in adiabatic state preparation (though this has been contested [23]).

As outlined in [118], adiabatic state preparation can be trotterised and discretised so that it takes the form of a variational quantum algorithm. First, given a partition of the total evolution time  $T = \sum_j \Delta_j$ , where  $\Delta_j = t_j - t_{j-1}$ , the schedule  $s$  is discretised to a step-function

$$\tilde{s}(t) = s_j := s\left(\frac{t_j + t_{j-1}}{2}\right), \quad t_{j-1} \leq t < t_j, \quad (3.15)$$

and the resulting evolution operator is then trotterised to the form of QAOA in (3.5), with

$$\theta_{B,j} = s_j \Delta_j, \quad (3.16)$$

$$\theta_{A,j} = (1 - s_j) \Delta_j. \quad (3.17)$$

Thus, a quantum adiabatic state preparation schedule can be approximated by a variational algorithm. As  $p \rightarrow \infty$ , and since the angles  $\theta$  in the variational algorithm are free to vary, in this limit any adiabatic schedule can be emulated. This connection between adiabatic state preparation and variational algorithms allows us to obtain an important guarantee about the latter: since for finite systems the energy gap between the ground state and the first excited state does not completely close, the variational algorithm is guaranteed to prepare the target ground state in the  $p \rightarrow \infty$  limit.

#### 3.1.3 The barren plateau phenomenon

One of the principal issues with the use of variational quantum algorithms is the presence of barren plateaus, which consist in an exponential vanishing of the gradient of the cost function with respect to the parameters as the size of the problem increases, making the circuit untrainable. Formally, assuming a uniform distribution over the parameter space, a variational algorithm with parameterised circuit  $U(\theta)$ , initial state  $|\psi(0)\rangle$ , and cost function  $c(\theta)$ , is said to present a barren plateau if, for all indices  $j$

### 3.1 Background: Variational Quantum Algorithms

---

and  $\epsilon \in \mathbb{R}^+$ , it is the case that

$$P\left(\left|\frac{\partial c}{\partial \theta_j}\right| \geq \epsilon\right) \leq \mathcal{O}\left(e^{-L}\right). \quad (3.18)$$

An established method to diagnose the presence of a barren plateaus involves computing the variance of the gradient for a uniform distribution over the angles. Indeed, by Chebyshev’s inequality<sup>1</sup>, it must hold that

$$P\left(\left|\frac{\partial c}{\partial \theta_j}\right| \geq \epsilon\right) \leq \frac{\text{Var}\left(\left|\frac{\partial c}{\partial \theta_j}\right|\right)}{\epsilon^2}. \quad (3.20)$$

In the above, we make use of the fact that the mean value of the partial derivative of the cost function with respect to the uniform distribution over the parameter space is equal to zero for the circuits we consider [80, 121]. In practice, it has been observed that the scaling of the variance is the same for all indices  $j$  [80], so when computing the variance numerically it suffices to do so for a single parameter.

The phenomenon of barren plateaus was first identified in the context of random circuits [73, 121], and was later extended to general parameterised circuits [80] forming approximate *unitary 2-designs*. A distribution over a parameterised circuit is said to form a unitary  $t$ -design if averaging a function over this distribution yields the same results as averaging it over the Haar measure distribution up to the first  $t$  moments. The concept of a unitary 2-design features in randomised benchmarking [42], where one is interested in sampling over a set of unitaries that is representative of the full space of unitaries. Intuitively, the closer a distribution is to being a 2-design, the more expressive the associated parameterised circuit is. In this way, the presence of barren plateaus is linked to the expressibility of the parameterised circuit.

Before proceeding, we note that the field of variational quantum algorithms has undergone remarkable development in recent years. These have been extended and specialised to several other areas, such as machine-learning [19, 37] and finance [52, 141]. An increasing number of modifications and variations on existing algorithms have been

---

<sup>1</sup>Chebyshev’s inequality states that, for a random variable  $X$  with finite standard deviation  $\sigma \neq 0$  and mean  $\mu$ ,  $\forall \epsilon \in \mathbb{R}^+$  it is the case that

$$P(|X - \mu| \geq \epsilon\sigma) \leq \frac{1}{\epsilon^2}. \quad (3.19)$$

proposed to tackle existing issues, such as e.g. adaptively constructing the quantum circuit [68, 217] to be optimised, using classical shadows to avoid barren plateaus [167] or using specialised optimisers [179], among several others. Moreover, VQAs have recently been combined with tensor network quantum simulation techniques to enable efficient quantum circuit compression schemes [8, 45, 82, 107], with applications to machine learning and quantum dynamics. While at present it is still unclear when practical quantum advantage will be reached [39, 173], variational quantum algorithms have proven to be a compelling avenue of research.

### 3.2 Lie Theory of Parameterised Quantum Circuits

The parameterised quantum circuits we will focus on throughout this thesis are constructed by directly adopting an alternating “bang-bang” structure [212], and encompass all the cases described in Section 3.1.1 above except the HEA<sup>1</sup>. Given a tuple of Hamiltonians

$$\mathbf{H} = (H_1, \dots, H_m), \quad (3.21)$$

the circuit is defined by the unitary operator

$$U(\boldsymbol{\theta}, p) = \exp(-i\theta_{p,m}H_m) \dots \exp(-i\theta_{p,1}H_1) \dots \exp(-i\theta_{1,m}H_m) \dots \exp(-i\theta_{1,1}H_1), \quad (3.22)$$

where  $p$  controls the circuit depth and  $\boldsymbol{\theta} \equiv \{\theta_{1,1}, \theta_{1,2}, \dots, \theta_{p,m}\}$  are the parameters to be optimised. We call such a tuple of Hamiltonians  $\mathbf{H}$  a *protocol*. The associated parameters are often called *angles* in the literature. Despite the similarity, note that this framework is more general than the HVA, as the protocol is not necessarily obtained from a splitting of the target Hamiltonian, nor is it necessary that  $[H_a, H_b] \neq 0$ .

#### 3.2.1 Background: Characterising unitaries generated by a PQC

Lie theoretical techniques provide a powerful tool to characterise the expressibility of quantum controllable systems [3]. They have been used in the literature to prove the universality of a set of variational protocols (3.21) under certain assumptions [128],

---

<sup>1</sup>This is because we do not consider non-parameterised gates, though the framework we adopt here could easily be adapted to include this case if necessary.

## 3.2 Lie Theory of Parameterised Quantum Circuits

---

to characterise barren plateaus and overparameterisation (which we will explore in Section 4.3) in variational quantum algorithms [99, 100], and have recently found use in studying symmetries in data in the context of quantum machine learning [101, 124].

We begin by briefly summarising and formalising the existing theory in the literature and defining the associated notation. Given  $U(\boldsymbol{\theta}, p)$  as in (3.22) defined by the Hamiltonians  $\mathbf{H} = (H_1, \dots, H_m)$ , we define

$$\mathcal{U} = \bigcup_{p=1}^{\infty} \mathcal{U}^p, \quad \mathcal{U}^p = \{U(\boldsymbol{\theta}, p) : \boldsymbol{\theta} \in \mathbb{R}^{mp}\}. \quad (3.23)$$

The set  $\mathcal{U}$  contains all unitaries that the protocol  $\mathbf{H}$  can generate at arbitrary circuit depth. It is a group, as it contains the product of any two of its elements and the inverse of any of its elements. Further, since matrix multiplication is differentiable<sup>1</sup>, it constitutes a *Lie group*.

Associated to the Lie group  $\mathcal{U}$  is a *Lie algebra*  $\mathfrak{u}$ , which can be defined at a point  $\boldsymbol{\theta}$  as

$$\mathfrak{u} = \left\{ \frac{\partial U(\boldsymbol{\theta}, p)}{\partial \theta_j} : j, p \in \mathbb{N}^+ \right\}. \quad (3.24)$$

It characterises how the circuit  $U(\boldsymbol{\theta}, p)$  changes with an infinitesimal variation of the parameters. Note that  $\mathcal{U} = \{e^{-iH} : iH \in \mathfrak{u}\}$  and that  $\mathfrak{u} = \langle iH_1, \dots, iH_m \rangle$  [38, 128], where  $\langle \dots \rangle$  denotes the Lie algebra generated by these elements i.e. the vector space obtained by iteratively taking the Lie bracket  $[A, B] = AB - BA$  of  $iH_1, \dots, iH_N$  until no new elements linearly independent with the previous ones can be obtained [72]. This forms the smallest possible Lie algebra that contains the specified generators.

### 3.2.2 Characterising states generated by a PQC

In this thesis, we introduce

$$\mathcal{S}^p = \{U(\boldsymbol{\theta}, p)|\psi(0)\rangle : \boldsymbol{\theta} \in \mathbb{R}^{mp}\}, \quad \mathcal{S} = \bigcup_{p=1}^{\infty} \mathcal{S}^p, \quad (3.25)$$

---

<sup>1</sup>In the sense that the matrix multiplication function  $m(A, B) = AB$  is differentiable as a multivariate function.

### 3.3 The expressibility of the 1D QAOA in terms of free-fermions

---

as the set of states preparable by the variational quantum circuit at depth  $p$  and at any depth, respectively. Note that  $\mathcal{S}$  depends on the initial state chosen. We will restrict our analysis to compact Lie groups, for which there must exist a  $p^*$  such that  $\mathcal{U} = \mathcal{U}^{p^*}$  [38]. By the same argument, there must be a  $\hat{p}$  such that  $\mathcal{S} = \mathcal{S}^{\hat{p}}$ . This represents the circuit depth at which the circuit has reached *maximum expressibility* for a given initial state. We will see that, in general,  $\hat{p} < p^*$ . This happens because we find that there can be a set  $\mathcal{G}$  of unitary matrices in  $\mathcal{U}$  that leave the initial state  $|\psi(0)\rangle$  invariant, forming a stabiliser subgroup. Mathematically, this translates into  $\mathcal{U}$  having a fibre bundle structure and  $\mathcal{S} \cong \mathcal{U}/\mathcal{G}$ , where  $\mathcal{G}$  represents a *Gauge symmetry group* [132] (see Figure 3.2 for a graphical representation). As a consequence of this,

$$\dim \mathcal{S} = \dim \mathcal{U} - \dim \mathcal{G}, \quad (3.26)$$

justifying that, in general,  $\mathcal{S}$  will require fewer parameters to describe than  $\mathcal{U}$ . It is an open question whether there is a method to systematically determine  $p^*$  and  $\hat{p}$  given a set of Hamiltonians  $\mathcal{H}$ . The group  $\mathcal{G}$  is generated by a subalgebra  $\mathfrak{g}$  of the Lie algebra  $\mathfrak{u}$  formed by the elements that (infinitesimally) do not change the quantum state, i.e.

$$\mathfrak{g} = \{K : K|\psi\rangle = \lambda|\psi\rangle, iK \in \mathfrak{u}, \lambda \in \mathbb{R}\}. \quad (3.27)$$

Since  $\mathcal{U} = \{e^{-iA_1}e^{-iA_2}\dots e^{-iA_m} : m \in \mathbb{N}, iA_j \in \mathfrak{u}\}$  [38, 128], the unitaries in  $\mathcal{U}$  can approximate a quantum adiabatic evolution and thus prepare the ground state of any Hamiltonian in  $\mathfrak{u}$  [118], provided that  $|\psi(0)\rangle$  is the ground state of some  $H_0 \in \mathfrak{u}$ . This results from the connection between variational algorithms and adiabatic state preparation outlined in Section 3.1. Conversely, if  $|\psi\rangle$  is prepared by  $U \in \mathcal{U}$ , then it is the ground state of  $H = UH_0U^\dagger \in \mathfrak{u}$ . Thus, the Lie algebra  $\mathfrak{u}$  fully characterises the set  $\mathcal{S}$  of preparable states; we will exploit this in Section 3.3 to study the expressibility of certain variational protocols.

### 3.3 The expressibility of the 1D QAOA in terms of free-fermions

Following the framework outlined in Section 3.1, in this Section we study two different protocols:

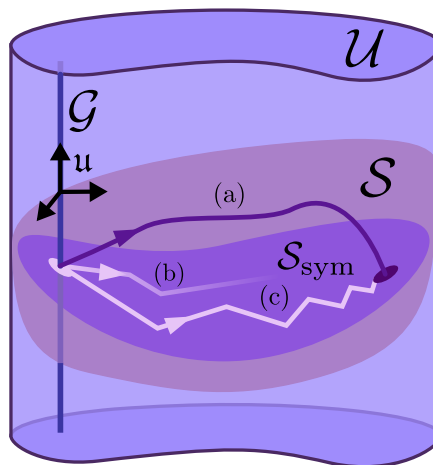


Figure 3.2: Schematic depicting the Lie structures introduced in Section 3.2 and their relation to variational optimisation. From an initial state, the set of unitaries generated by the parameterised circuit,  $\mathcal{U}$ , prepares a manifold of states  $\mathcal{S}$ . The space of directions that the protocol is able to explore at a given point is characterised by the Lie algebra  $\mathfrak{u}$ , and there is a redundancy in the unitaries preparing a state which is represented by a stabiliser Gauge group  $\mathcal{G}$ . Symmetries in the protocol constrain the optimisation (a) to a submanifold of states  $\mathcal{S}_{\text{sym}}$  which, as later explained in Section 4.2, may affect the landscape by introducing local minima (b) or by restricting the features available to the optimiser, causing the optimisation to take longer (c).

1. A *site-independent* protocol, defined by the tuple

$$\mathcal{J} = \left( \sum_j X_j X_{j+1}, \sum_j Z_j \right) = \left( -i \sum_j \gamma_{2j} \gamma_{2j+1}, -i \sum_j \gamma_{2j-1} \gamma_{2j} \right), \quad (3.28)$$

and we denote its Lie algebra by  $\mathfrak{i}$ .

2. A *site-dependent* protocol, defined by the tuple

$$\mathcal{D} = (X_1 X_2, \dots, X_{N-1} X_N, Z_1, \dots, Z_N) \quad (3.29)$$

$$= (-i\gamma_2 \gamma_3, \dots, -i\gamma_{N-1} \gamma_{N-2}, -i\gamma_1 \gamma_2, \dots, -i\gamma_{N-1} \gamma_N), \quad (3.30)$$

and we denote its Lie algebra by  $\mathfrak{d}$ .

Both are illustrated in Figure 3.3. The site-independent protocol corresponds to the original QAOA protocol [58] on a 1D lattice, while the site-dependent one results from re-

### 3.3 The expressibility of the 1D QAOA in terms of free-fermions

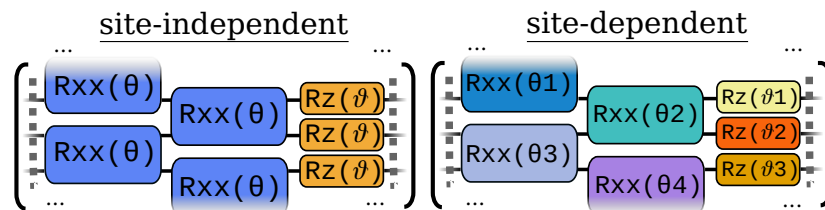


Figure 3.3: Parameterised circuits corresponding to the variational protocols (3.28), (3.29).

moving the layer-wise coupling in the angles of this original protocol [77]. In Chapter 4, we will see that this decoupling results in distinct properties with respect to the optimisation of the associated variational algorithm. Writing out the corresponding unitary explicitly, we obtain

$$\begin{aligned}
 U(\boldsymbol{\theta}, p) = & \exp\left(-i \sum_k \theta_{p,Z}^k Z_k\right) \exp\left(-i \sum_k \theta_{p,XX}^k X_k X_{k+1}\right) \dots \\
 & \exp\left(-i \sum_k \theta_{1,Z}^k Z_k\right) \exp\left(-i \sum_k \theta_{1,XX}^k X_k X_{k+1}\right). \quad (3.31)
 \end{aligned}$$

As mentioned above, the site-independent protocol can be seen as the site-dependent one with the additional constraint that  $\theta_{a,P}^i = \theta_{a,P}$ . Thus, in the site-independent protocol, the value of an angle is the same across a circuit layer, and is independent of the lattice sites that the corresponding operator is acting on.

We now deduce the full structure of the Lie algebras corresponding to the protocols (3.28) and (3.29) above for different boundary conditions. Note that, after applying the Jordan-Wigner transformation, both protocols only feature quadratic Hamiltonians, which we first introduced in Section 2.4. As such, they commute with the fermionic parity operator  $P = \prod_j Z_j$ , and can thus be decomposed into two components, one acting on the positive parity sector and the other acting on the negative parity sector. We will begin by deriving a basis for the algebras unrestricted to any symmetry sector, restricting them to a fixed parity symmetry sector, and seeing how this affects the structure and dimensions of the algebra. Restricting them to a specific parity sector will, in particular, allow us to map the resulting algebras to Majorana operators using the Jordan-Wigner transformation. Note that, for notational simplicity, we often disregard signs when converting from spin to Majorana operators when it does not influence the

### 3.3 The expressibility of the 1D QAOA in terms of free-fermions

---

generated Lie algebras.

In what follows, when computing the generators of the Lie algebra of the stabiliser Gauge group for a quantum state, it suffices to consider the elements of the relevant Lie algebra (seen as quadratic Hamiltonians) that commute with the corresponding covariance matrix, i.e.

$$\mathfrak{g} = \{K \in \mathfrak{u} : [K, \Gamma] = 0\}. \quad (3.32)$$

In our derivations, we consider  $\Gamma = \bigoplus_{j=1}^L \begin{bmatrix} 0 & 1 \\ -1 & 0 \end{bmatrix}$ ; the corresponding algebra for other covariance matrices can be obtained by conjugation.

**Lemma 2.** A basis for the Lie algebra generated by  $\mathcal{D} = \{iZ_j, iX_j X_{j+1}\}_{j=1, \dots, L}$

1. with OBC is

$$\begin{aligned} \mathfrak{d}_{\text{OBC}} &= \{iZ_j, \\ &\quad iX_j Z \dots Z X_k, \quad iX_j Z \dots Z Y_k, \\ &\quad iY_j Z \dots Z X_k, \quad iY_j Z \dots Z Y_k : 1 \leq j < k \leq L\} \end{aligned} \quad (3.33)$$

$$= \{\gamma_j \gamma_k : 1 \leq j < k \leq L\}, \quad (3.34)$$

and it has dimension  $L(2L - 1)$ . A basis for the Lie algebra of the associated Gauge group is

$$\begin{aligned} \mathfrak{g}(\mathfrak{d}_{\text{OBC}}) &= \{iZ_j, \\ &\quad iX_j Z \dots Z X_k + iY_j Z \dots Z Y_k, \\ &\quad iY_j Z \dots Z X_k - iX_j Z \dots Z Y_k : 1 \leq j < k \leq L\} \end{aligned} \quad (3.35)$$

$$\begin{aligned} &= \{\gamma_{2j-1} \gamma_{2j}, \\ &\quad \gamma_{2j} \gamma_{2k-1} - \gamma_{2j-1} \gamma_{2k}, \\ &\quad \gamma_{2j-1} \gamma_{2k-1} + \gamma_{2j} \gamma_{2k} : 1 \leq j < k \leq L\}, \end{aligned} \quad (3.36)$$

and it has dimension  $L^2$ .

### 3.3 The expressibility of the 1D QAOA in terms of free-fermions

---

2. with PBC is

$$\mathfrak{d}_{\text{PBC}} = \mathfrak{d}_{\text{OBC}} \cup (P \cdot \mathfrak{d}_{\text{OBC}}), \quad (3.37)$$

where

$$\begin{aligned} (P \cdot \mathfrak{d}_{\text{OBC}}) = \{ & iZ \dots Z_{j-1} Z_{j+1} \dots Z, \quad iZ \dots Z X_j X_k Z \dots Z, \\ & iZ \dots Z X_j Y_k Z \dots Z, \quad Z \dots Z Y_j X_k Z \dots Z, \\ & iZ \dots Z Y_j Y_k Z \dots Z \quad : 1 \leq j < k \leq L\}, \end{aligned} \quad (3.38)$$

and it has dimension  $2L(2L - 1)$ .

**Lemma 3.** A basis for the Lie algebra generated by  $\mathcal{J} = \{i \sum_j Z_j, i \sum_j X_j X_{j+1}\}$

1. with OBC is

$$\begin{aligned} \mathfrak{i}_{\text{OBC}} = \{ & iZ_j + iZ_{L-j+1}, \\ & iX_j Z \dots Z X_k + iX_{L-k+1} Z \dots Z X_{L-j+1}, \\ & iX_j Z \dots Z Y_k + iY_{L-k+1} Z \dots Z X_{L-j+1}, \\ & iY_j Z \dots Z X_k + iX_{L-k+1} Z \dots Z Y_{L-j+1}, \\ & iY_j Z \dots Z Y_k + iY_{L-k+1} Z \dots Z Y_{L-j+1}, \\ & 1 \leq j < k \leq \lceil L/2 \rceil \} \end{aligned} \quad (3.39)$$

$$\begin{aligned} = \{ & \gamma_{2j-1} \gamma_{2j} + \gamma_{2L-2j+1} \gamma_{2L-2j+2}, \\ & \gamma_{2j} \gamma_{2k-1} + \gamma_{2L-2k+2} \gamma_{2L-2j+1}, \\ & \gamma_{2j} \gamma_{2k} - \gamma_{2L-2k+2} \gamma_{2L-2j+2}, \\ & \gamma_{2j-1} \gamma_{2k-1} - \gamma_{2L-2k+1} \gamma_{2L-2j+1}, \\ & \gamma_{2j-1} \gamma_{2k} + \gamma_{2L-2k+1} \gamma_{2L-2j+2}, \\ & : 1 \leq j < k \leq \lceil L/2 \rceil \}, \end{aligned} \quad (3.40)$$

and this algebra has dimension  $L^2$  [100]. A basis for the Lie algebra of the

### 3.3 The expressibility of the 1D QAOA in terms of free-fermions

---

associated Gauge group is

$$\begin{aligned}
\mathfrak{g}(\mathfrak{iOBC}) = & \{iZ_j + iZ_{L-j+1}, \\
& iX_j Z \dots Z X_k + iX_{L-k+1} Z \dots Z X_{L-j+1} \\
& + iY_j Z \dots Z Y_k + iY_{L-k+1} Z \dots Z Y_{L-j+1}, \\
& iX_j Z \dots Z Y_k + iY_{L-k+1} Z \dots Z X_{L-j+1} \\
& - iY_j Z \dots Z X_k - iX_{L-k+1} Z \dots Z Y_{L-j+1}, \\
& : 1 \leq j < k \leq L\}
\end{aligned} \tag{3.41}$$

$$\begin{aligned}
= & \{\gamma_{2j-1}\gamma_{2j} + \gamma_{2L-2j+1}\gamma_{2L-2j+2}, \\
& \gamma_{2j}\gamma_{2k-1} + \gamma_{2L-2k+2}\gamma_{2L-2j+1} - \gamma_{2j-1}\gamma_{2k} - \gamma_{2L-2k+1}\gamma_{2L-2j+2}, \\
& \gamma_{2j}\gamma_{2k} - \gamma_{2L-2k+2}\gamma_{2L-2j+2} + \gamma_{2j-1}\gamma_{2k-1} - \gamma_{2L-2k+1}\gamma_{2L-2j+1} \\
& : 1 \leq j < k \leq L\},
\end{aligned} \tag{3.42}$$

and it has dimension  $\frac{1}{2}L(L-1)$ .

2. with PBC is

$$\begin{aligned}
\mathfrak{iPBC} = & \{i \sum_j (Z_j + Z_1 \dots Z_{j-1} Z_{j+1} \dots Z_L), \\
& i \sum_j (X_j Z \dots Z X_{j+k} + Z_1 \dots Z_{j-1} X_j X_{j+(L-k)} Z_{j+(L-k)+1} \dots Z_L), \\
& i \sum_j (X_j Z \dots Z Y_{j+k} + Y_j Z \dots Z X_{j+k} + Z_1 \dots Z_{j-1} X_j Y_{j+(L-k)} Z_{j+(L-k)+1} \dots Z_L \\
& + Z_1 \dots Z_{j-1} Y_j X_{j+(L-k)} Z_{j+(L-k)+1} \dots Z_L), \\
& i \sum_j (Y_j Z \dots Z Y_{j+k} + Z_1 \dots Z_{j-1} Y_j Y_{j+(L-k)} Z_{j+(L-k)+1} \dots Z_L) \\
& : 1 \leq k \leq L-1\},
\end{aligned} \tag{3.43}$$

and it has dimension  $3L-2$ .

The proofs for these statements follow by directly taking the brackets of the generators of these algebras. Here, we provide a proof for the structure of  $\mathfrak{d}_{\text{OBC}}$ ; the others can be derived similarly.

*Proof.* By induction on  $L$ :

### 3.3 The expressibility of the 1D QAOA in terms of free-fermions

---

$L = 2$ : Taking the Lie brackets iteratively of  $\{iZ_1, Z_2, iX_1X_2\}$ , one obtains the linearly independent set  $\{iZ_1, iZ_2, iX_1X_2, iX_1Y_2, iY_1X_2, iY_1Y_2\}$ , which has 6 elements.

$L \implies L + 1$ : Assume the Lemma holds for  $L$ . Then, define

$$\mathcal{G}_{a,b} := \{iZ_j, iX_jX_{j+1}\}_{j=a,\dots,b}, \quad (3.44)$$

$$\mathcal{L}_{a,b} := \{iZ_j, iT_{j,k} : a \leq j < k \leq b\}, \quad (3.45)$$

$$T_{j,k} := A_j \otimes \left( \bigotimes_{m=j+1}^{k-1} Z_m \right) \otimes B_k, \quad A_m, B_m \in \{X_m, Y_m\}, \quad (3.46)$$

and let  $\mathcal{R}_{a,b}$  be the Lie algebra generated by  $\mathcal{G}_{a,b}$ . We must prove that  $\mathcal{R}_{1,L+1} = \mathcal{L}_{1,L+1}$ .

By induction hypothesis  $\mathcal{R}_{1,L} = \mathcal{L}_{1,L}$ . Using this, and the definition of Lie algebra generators, we obtain  $\mathcal{L}_{1,L} \subseteq \mathcal{R}_{1,L+1}$ . Since it is easy to prove that

$$[iT_{i,j}, iT_{k,l}] \propto \delta_{jk} iT_{i,l}, \quad (3.47)$$

and  $[iT_{i,j}, iZ_k] \propto (\delta_{ik} + \delta_{jk}) iT_{i,j}$ , we conclude that  $\mathcal{R}_{1,L+1} \setminus \mathcal{L}_{1,L} \subseteq \{iT_{k,L+1}\}_{k=1,\dots,L} \cup \{iZ_{L+1}\}$ . But  $T_{k,L+1} \in \mathcal{L}_{k,L+1} = \mathcal{R}_{k,L+1} \subseteq \mathcal{R}_{1,L+1}$ , and  $Z_{L+1} \in \mathcal{G}_{1,L+1}$ . Thus, it must be the case that  $\mathcal{R}_{1,L+1} = \mathcal{L}_{1,L+1}$ .

Since, from the above,  $\mathcal{L}_{1,L+1} = \mathcal{L}_{1,L} \cup \{T_{k,L+1}\}_{k=1,\dots,L} \cup \{Z_{L+1}\}$ , and since these sets are disjoint, using the induction hypothesis, the dimension of  $\mathcal{L}_{1,L+1}$  is  $L(2L-1) + 4L + 1 = (L+1)(2(L+1) - 1)$ .  $\square$

We now state the structure of these algebras restricted to each of the parity symmetry sectors. As can be seen in Lemma 2 for the generators  $\mathcal{D}$ , when restricting to a parity sector, the algebra in the OBC case remains unchanged, while the algebra in the PBC case is cut in half, and is equal to former. Hence:

$$\mathfrak{d} := \mathfrak{d}_{\text{OBC}} = \mathfrak{d}_{\text{OBC}} \Big|_{P=\pm 1} = \mathfrak{d}_{\text{PBC}} \Big|_{P=\pm 1}, \quad (3.48)$$

and it has dimension  $L(2L-1)$ . For the case of the set of generators  $\mathcal{J}$ , the algebra

### 3.3 The expressibility of the 1D QAOA in terms of free-fermions

---

with OBC also remains unchanged when restricted to a parity sector. Hence,

$$\mathfrak{i}_{\text{OBC}} = \mathfrak{i}_{\text{OBC}} \Big|_{P=\pm 1}, \quad (3.49)$$

and it has dimension  $L^2$ . Finally, the same set of generators with PBC yields

$$\begin{aligned} \mathfrak{i}_{\text{PBC}} \Big|_{P=\pm 1} = & \left\{ i \sum_j Z_j, \right. \\ & i \sum_j (X_j Z \dots Z X_{j+k} \mp Y_j Z \dots Z Y_{j+L-k}), \\ & i \sum_j (X_j Z \dots Z Y_{j+k} + Y_j Z \dots Z X_{j+k} \\ & \quad \pm X_j Z \dots Z Y_{j+L-k} \pm Y_j Z \dots Z X_{j+L-k}), \\ & i \sum_j (Y_j Z \dots Z Y_{j+k} \mp X_j Z \dots Z X_{j+L-k}) : \\ & \left. 1 \leq k \leq L-1 \right\} \end{aligned} \quad (3.50)$$

$$\begin{aligned} = & \left\{ \sum_j \gamma_{2j-1} \gamma_{2j}, \right. \\ & \sum_j \gamma_{2j} \gamma_{2(j+k)-1} \pm \gamma_{2j-1} \gamma_{2(j+L-k)}, \\ & \sum_j \gamma_{2j} \gamma_{2(j+k)} - \gamma_{2j} \gamma_{2(j+k)-1} \\ & \quad \pm \gamma_{2j} \gamma_{2(j+L-k)-1} \mp \gamma_{2j-1} \gamma_{2(j+L-k)-1}, \\ & \sum_i \gamma_{2j-1} \gamma_{2(j+k)} \pm \gamma_{2j} \gamma_{2(j+L-k)-1} \\ & \left. : 1 \leq k \leq L-1 \right\}, \end{aligned} \quad (3.51)$$

### 3.3 The expressibility of the 1D QAOA in terms of free-fermions

---

and it has dimension  $\lfloor 3L/2 \rfloor$ . A basis for the associated Gauge group Lie algebra is:

$$\begin{aligned} \mathfrak{g}(\text{iPBC}|_{P=\pm 1}) = & \left\{ i \sum_j Z_j, \right. \\ & i \sum_j (X_j Z \dots Z X_{j+k} \mp Y_k Z \dots Z Y_{j+L-k} \\ & \left. - Y_j Z \dots Z Y_{j+k} \pm X_j Z \dots Z X_{j+L-k}) : \right. \\ & \left. 1 \leq k \leq L-1 \right\} \end{aligned} \quad (3.52)$$

$$\begin{aligned} = & \left\{ \sum_j \gamma_{2j-1} \gamma_{2j}, \right. \\ & \sum_j \gamma_{2j} \gamma_{2(j+k)-1} \pm \gamma_{2j-1} \gamma_{2(j+L-k)} \\ & \left. + \gamma_{2j-1} \gamma_{2(j+k)} \pm \gamma_{2j} \gamma_{2(j+L-k)-1} \right. \\ & \left. : 1 \leq k \leq L-1 \right\}, \end{aligned} \quad (3.53)$$

and it has dimension  $\lfloor L/2 \rfloor$ .

We can now characterise the expressibility of the protocols (3.28), (3.29) by examining the corresponding Lie algebra. In particular, we are able to determine the set of unitary operators  $\mathcal{U}$  that each protocol can generate and the set of states  $S$  that each can prepare. We consider the initial state to be a fermionic Gaussian state of a given parity respecting the symmetries of the circuit. Our results are summarised in Table 3.1. After applying the Jordan-Wigner transformation to the derived Lie algebras, these can be seen to form the set of free-fermionic Hamiltonians satisfying the symmetries of the circuit. As shown in Section 3.2, every ground state of such a Hamiltonian can be prepared by the circuit at some depth; and the set of these ground states are precisely the fermionic Gaussian states having the same parity as the initial state and respecting the appropriate symmetries. As outlined in Section 3.2, there can be a symmetry subgroup  $\mathcal{G}$  of  $\mathcal{U}$  that leaves the initial state invariant. In the case of a FGS, there is a  $U(L)$  freedom in the fermionic modes, which can be rotated without changing the underlying state [211]. The subset of these rotations contained in  $\mathcal{U}$  will form  $\mathcal{G}$ ; this can be all of the  $U(L)$  freedom, as is the case of the site-dependent protocol, or only part of it, in which case  $\dim \mathcal{G} < \dim U(L)$ .

	Dependent		Independent	
	OBC	PBC	OBC	PBC
$\mathcal{S}$	fixed parity FGS		fixed parity FGS satisfying (2.31)	fixed parity FGS satisfying (2.30) & (2.31)
$\mathfrak{u}$	(3.33)	(3.37)	(3.39)	(3.43)
$\mathfrak{u}$ (fixed parity)	(3.33)		(3.39)	(3.50)
$\mathfrak{g}$ (fixed parity)	(3.35)		(3.41)	(3.52)
$\dim \mathcal{U}$	$L(2L - 1)$	$2L(2L - 1)$	$L^2$	$3L - 2$
$\dim \mathcal{U}$ (fixed parity)	$L(2L - 1)$		$L^2$	$\lfloor 3L/2 \rfloor$
$\dim \mathcal{G}$	$L^2$		$L(L + 1)/2$	$\lfloor L/2 \rfloor$
$\dim \mathcal{S}$	$L(L - 1)$		$L(L - 1)/2$	$L$

Table 3.1: Table summarising the expressibility of the site-dependent, Eq. (3.28), and site-independent, Eq. (3.29), protocols. The basis for the corresponding Lie algebra  $\mathfrak{u}$  is referenced in this table. As outlined in the main text, these are used to analytically deduce  $\mathcal{U}$ , the space of unitaries that each protocol can generate, and  $\mathcal{S}$ , the space of states that each protocol can prepare. We assume that the initial state is a FGS of a given parity respecting the symmetries of the circuit.

### 3.4 Conclusion

In this section, we have reviewed and expanded upon the Lie theoretical framework for parameterised quantum circuits, a fundamental tool in the analysis of their expressibility. While it had been previously established that the Lie algebra of a variational protocol can be used to characterise the unitaries that it can generate [3, 99, 100, 128], we have pointed out that it also fully determines the set of quantum states that can be prepared, which is formed by the ground states of the Hamiltonians in this algebra (provided that the initial state is one such ground state). Furthermore, we show that, in general, the dimension of this set of states is smaller than that of the corresponding Lie algebra, and that there is a Gauge symmetry group that effectively maps Hamiltonians having the same ground state into each other.

Leveraging these results, we analytically proved that a state can be prepared by

the one-dimensional QAOA (as defined in Eqs. (3.31)) at some depth if and only if it is free-fermionic (under the Jordan-Wigner transformation) and respects the symmetries of the circuit. A fermionic perspective on QAOA had been previously taken to analytically study the ground state preparation of the Ising model [47, 203], and variational preparation of particular free models had been performed, both numerically [47, 78, 86, 139] and on real devices [32, 181]; here, we show that the ground state of any such model can be obtained using the QAOA. This was done by deriving a basis for the associated Lie algebra, which also provided us with an explicit form for the vector space of Hamiltonians for which the ground state can be prepared by the algorithm. We will exploit this in Chapter 4, to conduct a comprehensive numerical study of the associated classical optimisation. Values for the dimension of the Lie algebra and space of preparable states are included in Table 3.1; the latter imposes a minimum number of parameters the circuit should have to successfully prepare any fermionic Gaussian state, while the former is known to determine how fast the gradient with respect to the cost function vanishes [100]. By fully characterising these circuits on 1D lattices, we open the possibility to describe the QAOA on more complex graphs by first splitting them into simpler graphs. This could also help better understand the variants of QAOA which attempt to first solve the optimisation problem on subgraphs of the original graph before joining them [64, 216].

---

# CHAPTER 4

---

Optimisation in free-fermionic Variational  
Quantum Algorithms

---

In Chapter 3, we have studied the expressibility of the Quantum Approximate Optimisation Algorithm and concluded that, when the geometry of the underlying lattice is one-dimensional, the quantum states it can prepare are precisely the fermionic Gaussian states respecting the symmetries of the circuit. Despite elucidating which quantum states can be prepared, the aforementioned results do not say anything about the difficulty of the associated optimisation, nor identifies the circuit depth at which the algorithm can prepare these states. In this chapter, we exploit the fact that free-fermionic systems are efficient to simulate classically to perform a comprehensive numerical study of these questions.

We systematically explore how the variational protocol and the Hamiltonian featuring in the cost function can affect the associated optimisation. Moreover, we characterise overparameterisation [94, 210], which is known to make the optimisation significantly easier. We do this by exploiting the fact that overparameterisation starts at a circuit depth that is polynomial in lattice size for the ansätze we consider (this follows from the work in [99, 100] and our characterisation of  $\dim \mathcal{S}$  in Chapter 3). Though the list below is not exhaustive, we highlight the following contributions in this chapter (which we further discuss in the conclusions in Section 4.4):

- In Section 4.2 we observe that, when the quadratic Hamiltonian used in the cost function is non-local, enforcing symmetries introduces local minima to the landscape (which otherwise did not feature any), making the optimisation more difficult.
- In Section 4.3, we characterise overparameterisation with increasing circuit depth and for large lattice sizes, finding that:
  - The optimisation difficulty becomes largely independent of the quadratic Hamiltonian used in the cost function (see Figure 4.1).
  - As circuit depth increases, the average number of iterations to converge to the solution rapidly decreases, before tapering off and saturating at a depth  $p \propto L^2$  (see Figure 4.6).
  - The nr. of iterations to converge initially scales polynomially with lattice size, but this turns into a linear scaling as circuit depth increases (see Figure 4.7).

## 4.1 Minimum circuit depth for maximum expressibility

Following the framework set out in Section 3.2, we attempt to numerically determine the minimum depth  $\hat{p}$  necessary to prepare any state in  $\mathcal{S}$  for the protocols (3.28), (3.29). Recall that we denote by  $m$  the number of variational parameters per unit of  $p$ ; note that, from (3.22), this corresponds to the number of Hamiltonians in the protocol. While it is clear that  $m\hat{p}$  must be greater than  $\dim \mathcal{S}$ , the circuit must be also be deep enough so that correlations are able to propagate across the lattice [118]. A consequence of this is that  $\hat{p} \geq \lceil L/2 \rceil$ .

We numerically compute  $\hat{p}$  by randomly generating Hamiltonians in  $\mathbf{u}$  and verifying that their ground states are prepared to numerical precision. These Hamiltonians are created by taking a linear combination of the basis elements of the corresponding Lie algebras, derived in Section 3.3, where the coefficients are sampled from a normal distribution with mean equal to zero and standard deviation equal to one. We find, in cases where periodic boundary conditions (PBC) are employed, or where the site-dependent protocol is used, that  $\hat{p} = \lceil L/2 \rceil$ , saturating the aforementioned lower bound. This is also the minimum circuit depth found in the literature to be needed successfully prepare the ground state of the transverse field Ising model [78, 118, 203], which is a specific case of a free-fermionic model. For the remaining case, which corresponds to the site-independent protocol using open boundary conditions (OBC),  $\hat{p}$  proved to be unfeasible to determine numerically in a precise manner due to a significantly higher number of local minima.

The quantity

$$m\hat{p} - \dim \mathcal{S} \tag{4.1}$$

represents the number of parameters in the circuit that exceeds  $\dim \mathcal{S}$ . In the site-independent case with periodic boundary conditions,  $q\hat{p} = \dim \mathcal{S}$ . This suggests that, in this case,  $U(\hat{p}, \boldsymbol{\theta}) |\psi(\mathbf{0})\rangle$  forms a parameterisation of  $\mathcal{S}$ , as each fermionic Gaussian state should correspond to a unique set of circuit parameters when the associated angles are appropriately restricted (by e.g. taking into account their periodic nature). In contrast, in the site-dependent case with PBCs, there are  $q\hat{p} - \dim \mathcal{S} = L$  redundant parameters at  $\hat{p}$ . However, we note that one can do away with them by removing the last  $e^{-i \sum_j \theta_{p,z} Z_j}$  layer from this circuit, and we found that we were still able to prepare

randomly generated states in  $\mathcal{S}$  after doing this.

By abuse of terminology, and to separate the cases where the circuit depth is  $\hat{p}$  from those where the circuit depth exceeds this value, we refer to the behaviour at circuit depth  $\hat{p}$  as the *exactly parameterised regime*, regardless of whether  $q\hat{p} = \dim \mathcal{S}$ .

## 4.2 Effect of symmetry on cost minimisation

We proceed to study the hardness of the optimisation and the characteristics of the optimisation landscape when running a variational algorithm using the site-independent, Eq. (3.28), and site-dependent, Eq. (3.29), protocols. We work with PBC, and target the ground state of two models:

1. The critical transverse field Ising model [78]

$$H_I = - \sum_j X_j X_{j+1} - \sum_j Z_j. \quad (4.2)$$

2. Randomly generated symmetric quadratic Hamiltonians

$$H_G = i \sum_{jk} h_{jk} \gamma_j \gamma_k, \quad (4.3)$$

where  $h_{jk}$  respects Eq. (2.30) and Eq. (2.31).

The Ising model was introduced in Section 2.7, and is a well-known quantum-critical model in condensed matter physics [50] possessing a ground state for which the entanglement entropy diverges logarithmically with system size [27]. The second Hamiltonian is obtained by sampling at random out of all the ones for which the ground state is possible to prepare with both protocols. As mentioned at the end of Section 3.2, this is characterised by the Lie algebra corresponding to each protocol; in practice, the algebra of the site-dependent protocol contains that of the site-independent protocol, and the latter, when using PBC, consists of all quadratic Hamiltonians satisfying Eqs. (2.30)-(2.31). Just as in the previous section, these Hamiltonians are sampled by directly generating entries in  $h_{ij}$  using a normal distribution with mean equal to zero and standard deviation equal to one respecting these constraints. Moreover, throughout

## 4.2 Effect of symmetry on cost minimisation

this chapter we use a  $Z$ -polarized state

$$|\psi(0)\rangle = |\uparrow \dots \uparrow\rangle \quad (4.4)$$

as the initial state of the protocol, and the shifted energy density

$$e(|\psi\rangle) = \frac{\langle \psi | H | \psi \rangle - E_0}{L} \quad (4.5)$$

as the cost function, where  $E_0$  is the ground state energy of  $H$  and  $L$  is the size of the system under consideration. The classical minimisation is performed using the BFGS optimisation algorithm; though other optimisers such as Nelder-Mead and conjugate gradient were checked, and the behaviour obtained was qualitatively the same.

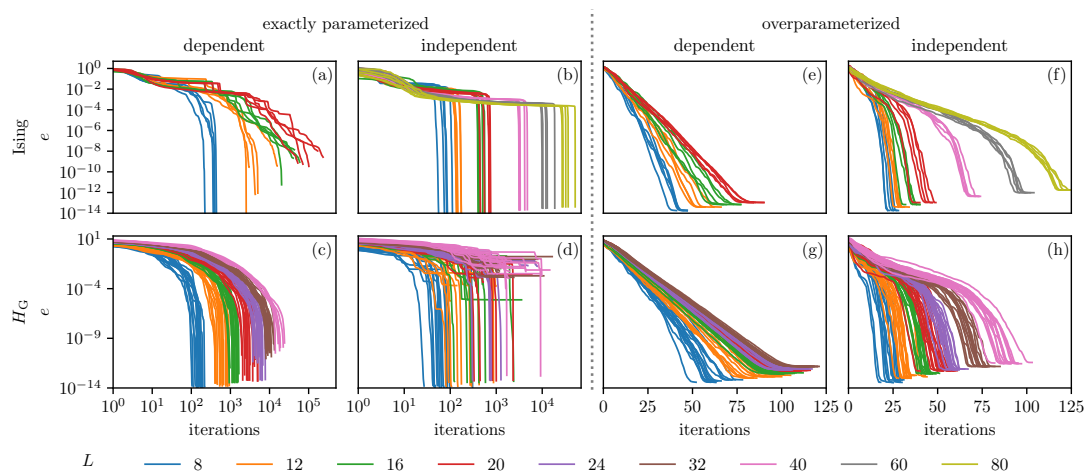


Figure 4.1: Cost function optimisation traces exposing the differences between the minimisations as the protocol and target Hamiltonian change. The effect of circuit depth is probed using the exactly parameterised regime ( $p = L/2$ ) and the overparameterised regime ( $p = L^2/4$ ). The target Hamiltonian is (Top row): the Ising model, as in Eq. (4.2), and 5 random initialisations per value of  $p$ , lattice size and protocol. (Bottom row): 3 randomly generated symmetric quadratic Hamiltonians, as in Eq. (4.3), and 5 random initialisations per generated Hamiltonian, value of  $p$ , lattice size and protocol. The maximum lattice size in each plot reflects the time taken to optimise the circuits, which depends on the number of parameters and on the number of iterations needed for convergence.

Figure 4.1 shows the optimisation traces after classically optimising the algorithm.

We compare two circuit depths:  $p = L/2$ , which we have numerically found to be the minimum depth for which the protocol reaches maximum expressibility, and  $p = L^2/4$ , well into the overparameterised regime (as we quantify in Section 4.3), where the redundancy in parameters is known to greatly reduce the computational cost of the optimisation [94, 95, 99, 210]. We defer a discussion of the latter for Section 4.3. In the following subsections, we observe different ways in which the characteristics of the optimisation can change when varying the target state and the protocol employed.

### 4.2.1 Influence of Hamiltonian locality on problem difficulty

Here, we explore how different properties of the target Hamiltonian can give rise to some of the phenomenology observed in Figure 4.1. One obvious property that distinguishes the Ising Hamiltonian, Eq. (4.2), from that of the random Hamiltonian, Eq. (4.3), is that the former is *local*, while generically this is not the case for the latter. Locality of the target Hamiltonian is known to influence whether the optimisation associated to a quantum circuit will feature barren plateaus, with non-local terms generally presenting exponentially vanishing gradients [31]. Locality can also have an influence below system sizes at which barren plateaus appear, and it has been argued that long-range interactions in the target Hamiltonian make the optimisation harder [109], resulting in higher values of the cost function at the optimum and requiring more iterations to converge.

In this section, we will see that the influence of the locality of the target Hamiltonian on optimisation depends on the constraints of the protocol being used. In particular, we will show that the site-independent and the site-dependent protocol behave differently in this respect. We use three families of models to quantify how the locality of the target Hamiltonian affects the hardness of the optimisation:

1. A special type of a long-range Ising Hamiltonian:

$$H(\alpha) = - \sum_r e^{-\alpha r} \sum_j X_j Z_{j+1} Z_{j+2} \dots Z_{j+r} X_{j+r+1} - \sum_j Z_j, \quad (4.6)$$

where  $\alpha > 0$  describes exponentially decaying interactions in a lattice. The choice of this Hamiltonian is motivated by the fact that its ground state can be expressed in terms of free-fermions for any  $\alpha$ , unlike the related models with power-law decaying interactions studied in Refs. [79, 109].

2.  $(k + 2)$ -local, symmetric, quadratic Hamiltonians

$$H_{\text{LG}}(k) = i \sum_{jl} \tilde{h}_{jl} \gamma_j \gamma_l, \quad \tilde{h}_{jl} = \begin{cases} \text{random, if } |j - l| < 2(k + 2), \\ 0, \text{ if } |j - l| \geq 2(k + 2), \end{cases} \quad (4.7)$$

which are derived from the randomly-generated generic symmetric quadratic Hamiltonians in Eq. (4.3) by setting  $h_{jl} = 0$  for any pair of Majoranas at a distance  $\geq 2(k + 2)$ .

3. A cluster Ising model at criticality [46, 139]

$$H_{\text{C}}(k) = - \sum_j X_j Z_{j+1} Z_{j+2} \dots Z_{j+r} X_{j+k+1} - \sum_j Z_j, \quad (4.8)$$

for which the ground state in one of the gapped phases is a symmetry-protected topological state [165].

In the two latter models, interactions are strictly limited to sites at most  $k + 2$  sites away, while in the first model they are exponentially suppressed.

Figure 4.2 compares the effect of locality on the optimisation. We vary the parameters controlling localisation of the couplings in each of the models Eqs. (4.6)-(4.8), and we measure the success probability in the site-independent case or the number of iterations to converge in the site-dependent case. The success probability is defined as the ratio between the number of random initialisations that resulted in the cost function dropping below numerical precision (and thus the target state being successfully prepared) versus the total number of initialisations. This measure was not used as a benchmark for the site-dependent protocol, as we have found that this protocol is not susceptible to getting trapped in local minima, and thus the success probability is always equal to one regardless of the locality of the Hamiltonian.

We see in Figure 4.2 that the more non-local the target Hamiltonian is, the lower the success probability is in the site-independent protocol. Surprisingly, however, we see that the more non-local the target Hamiltonian is, the *lower* the number of iterations is to converge in the site-dependent case. Both statements are verified for all the models introduced above. Thus, while locality makes it *easier* to prepare the target state using site-independent protocol, it makes the site-dependent protocol *harder* to optimise. We argue that, on the one hand, the symmetry constraints in the site-independent protocol

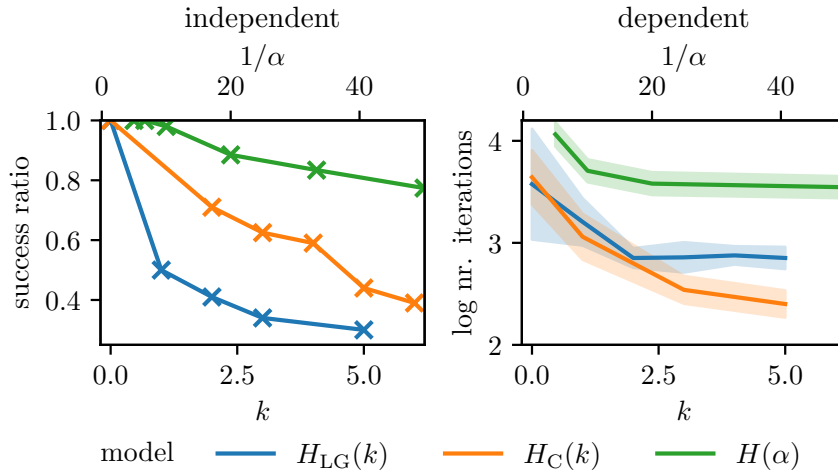


Figure 4.2: Effect of Hamiltonian locality on optimisation hardness in both the site-dependent and site-independent protocols in the exactly parameterised regime using PBCs. The labels refer to the target Hamiltonians defined in Eqs. (4.6), (4.7) and (4.8). The lattice size is 12, except for  $H_{LG}$ , which was computed for  $L = 16$ , as was  $H_C$  with the site independent protocol (this has no particular significance or influence in the results). Between 20 and 150 random initialisations were computed for each Hamiltonian parameter in the site-dependent cases, and between 200 and 500 were computed in the site independent ones. These indicate the number of samples until the results converged; the exact number needed depends on the specific Hamiltonian. The solid line is the mean value, while the shaded area indicates one standard deviation.

cause non-locality in the cost function to drive the optimisation into difficult regions that trap it in local minima. The site-dependent case, on the other hand, is free to explore the entire manifold of fermionic Gaussian states and bypass these traps, with the non-local terms leading the optimisation to converge faster, consistent with Figure 3.2(a), (b), (c).

#### 4.2.2 Cost stagnation and “staircase” plateaus

In Figure 4.1, we identify a “staircase” pattern emerging both when employing the site-dependent protocol to target the Ising model [Figure 4.1(a)] and when using the site independent protocol to target generic quadratic Hamiltonians [Figure 4.1(d)]; we highlight this in Figure 4.3(a). Noting that a similar sharp drop in the cost function

## 4.2 Effect of symmetry on cost minimisation

occurs when employing the site independent protocol to target the Ising model [Figure 4.1(b)], we plot the overlap of the state under preparation along the optimisation with the eigenstates of this Hamiltonian. Though this is only shown for one random initialisation of the parameters, we have run the optimisation several times for different initial conditions and observed the same behaviour. We notice that the overlap with the first excited state is orders of magnitude higher than with other excited eigenstates. The dynamics of state preparation is thus dominated by a competition between the ground state and the first excited state. We conjecture that the staircase plateaus we observe follow a similar mechanism: in each plateau, there is a state in the Hilbert space (akin to the first excited state in the previous description) that fully captures the features that the cost function struggles to distinguish from those of the ground state.

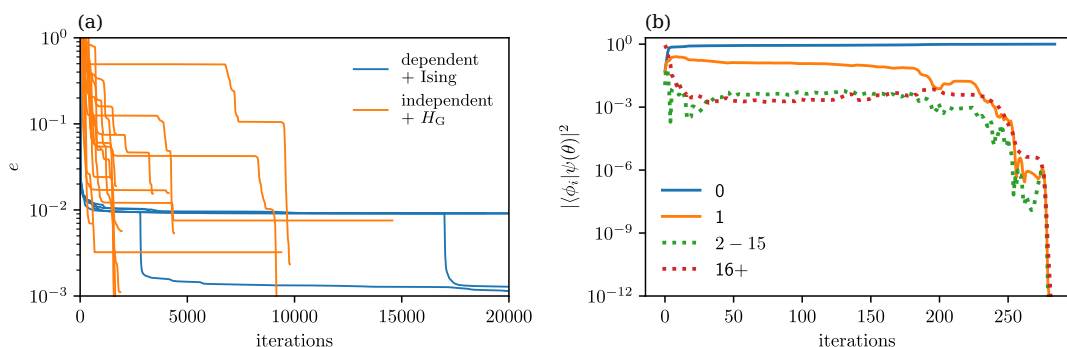


Figure 4.3: (a) Optimisation traces showing the “staircase” pattern seen in Figure 4.1. Here, the system size is 40, and the label refers to the protocol used and the Hamiltonian targetted, respectively. PBCs and  $p = L/2$  are used. (b) Overlaps of the lowest excited states of the target Hamiltonian with the state under preparation  $|\psi(\boldsymbol{\theta})\rangle$ . Numbers in the legend indicate eigenstate indices, with 0 being the ground state, 1 being the first excited state, etc. Single indices indicate that overlap with the corresponding eigenstate is being plotted. A range of indicate that the sum of the overlaps with the eigenstates having indices in that range is being plotted. We see a high overlap with the first excited state throughout the optimisation, indicating that the cost function cannot easily distinguish this state from the ground state. The site-independent protocol was used and the Ising model (4.2) was targeted at  $p = L/2$  and  $L = 16$ .

### 4.2.3 Rate of vanishing of gradients with lattice size

Here, we study how the variance of the gradient with respect to the centre angle in the vector of parameters  $\theta$  scales with the size of the lattice and the circuit depth. As mentioned in Section 3.1.3, this scaling with respect to the centre angle is taken to be representative of the scaling with respect to the other angles [7]; moreover, when the variance vanishes, so do the gradients themselves; as explained in Section 3.1.3, this phenomenon is dubbed a barren plateau [80, 121] when this vanishing is exponential in the size of the lattice.

Figure 4.4 illustrates the scaling of this variance with the lattice size, expressed in terms of the dimension of the Lie algebra, following Ref. [100], which conjectured that the variance of the gradient is inversely proportional to this dimension. We see that while this seems to hold in general, it depends on the circuit depth and the state under preparation. When preparing the Ising model, increasing the circuit depth changes this proportionality by a constant factor. Curiously, when preparing generic FGS with the site-dependent protocol, this factor is independent of the circuit depth. Note also that, when the circuit enters the overparameterised regime, for instance when targeting the Ising model in the site-independent case at  $p = 7L$ , this relation can break down as the variance of the gradient saturates at high circuit depths. Finally, we note that there are exceptions to this relation; in particular, we note that when preparing a generic FGS using the site independent protocol, the gradient seems to oscillate around a constant value of  $\sim 10$  without decaying as the system size increases.

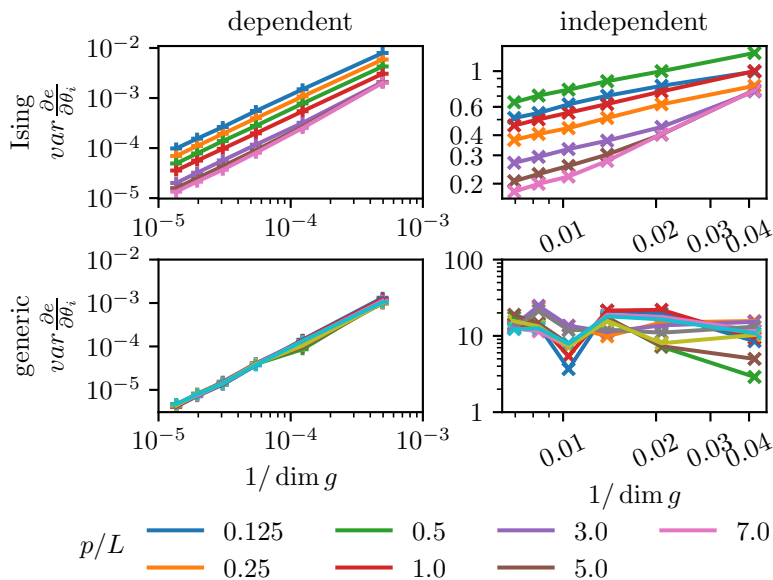


Figure 4.4: Variance of gradient taken at the centre angle  $\|\partial e/\partial\theta_j\|$  using the site-dependent protocol (left) and the site-independent protocol (right) with the ground state of the Ising model as a target state (top) and 5 generic quadratic Hamiltonians (symmetric quadratic Hamiltonians in the independent case) as a target state (bottom), plotted against the inverse of the dimension of the Lie algebra of the protocol, as computed in Section 3.3 and listed in Table 3.1 (note that here the parity is fixed). Various circuit depths, represented by the quantity  $p/L$  in the labels, were used. 20000 samples were taken per value of  $p$ , Hamiltonian and lattice size. Though the samples pertaining to the 5 generic quadratic Hamiltonians are considered simultaneously in the computation of the variance, plotting this variance separately for each such Hamiltonian does not significantly alter the plots shown.

Figure 4.5 illustrates the scaling of the variance of the gradient with circuit depth. We see that, when targeting the Ising model, there is an initial drop in this variance, which then stabilises to a fixed value. In contrast, when preparing a generic FGS, the variance almost immediately converges to this stable value, particularly in the site-dependent case.

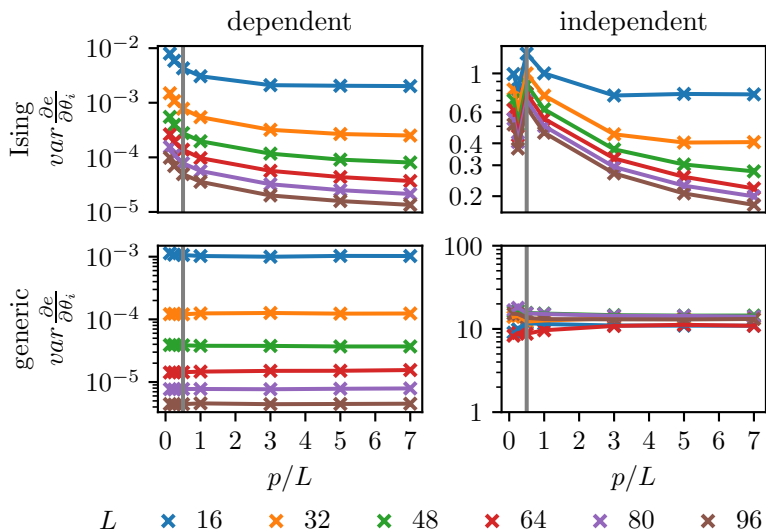


Figure 4.5: Variance of gradient taken at centre angle  $||\partial e / \partial \theta_i||$  using the site-dependent protocol (left) and the site-independent protocol (right) with the ground state of the Ising model as a target state (top) and 5 generic quadratic Hamiltonians (symmetric generic quadratic Hamiltonians in the independent case) as a target state (bottom), plotted against various values of  $p$  between 1 and  $4L$ . Several system sizes (bottom labels) were used. 20000 samples were taken per value of  $p$ , random state and lattice size. The vertical line indicates  $p = L/2$ .

### 4.3 The overparameterised regime

It has been pointed out [94, 210] that, when taking the circuit depth to be very large, the optimisation associated with Eq. (3.1) becomes considerably easier – a phenomenon dubbed *overparameterisation*. The onset of the overparameterised regime has been argued to correspond to the circuit depth at which the Quantum Fisher Information Metric saturates at every point  $\theta$  in the optimisation landscape [75, 99]. This is equivalent to the circuit depth at which an increase in  $p$  does not lead to an increase in the states that can be prepared by the variational circuit in Eq. (3.1), i.e., the circuit depth corresponding to  $\hat{p}$  as defined in Section 3.2.

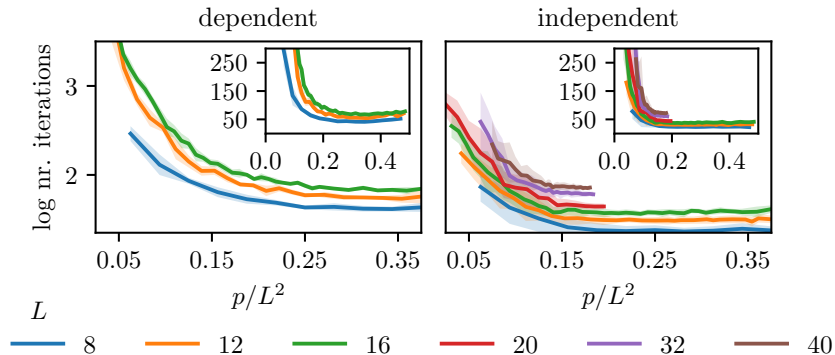


Figure 4.6: Number of iterations to converge vs. the circuit depth in the overparameterised regime. We see a decrease, consistent between different system sizes, which is at first pronounced, but then tapers off until it finally saturates at a circuit depth proportional to  $L^2$ . The insets use a linear scale for the vertical axis; they emphasise the point at which this saturation is reached. The target Hamiltonian is that of the Ising model, Eq. (4.2). Between 5 and 40 random initialisations were performed for each circuit depth; solid lines represent the mean value, and the shaded area indicates standard deviation.

### 4.3.1 Change in optimisation with increasing circuit depth

Here, we study how the number of iterations that the optimiser takes to prepare the state scales with the size of the lattice as the depth of the circuit increases well into the overparameterised regime. We find that, as depth increases, the average number of iterations to converge to the solution initially undergoes a large initial decay, until it slows down and saturates at  $p \propto L^2$ , i.e., past that point, no further increase in circuit depth provides a decrease in the number of iterations to converge. We observe this trend consistently between different optimisers and different system sizes, the latter shown in Figure 4.6. Further, by comparing how the average number of iterations that the optimiser takes to converge scales with lattice size, both when the circuit depth is equal to  $\hat{p}$  and into the overparameterised regime, we see that what is initially a polynomial scaling turns into a linear scaling with lattice size – see Figure 4.7.

From the above, we note that the overparameterised regime can represent a shift in the workload from the classical computer to the quantum computer, as increasing the number of parameters makes the classical optimisation easier, but the preparation

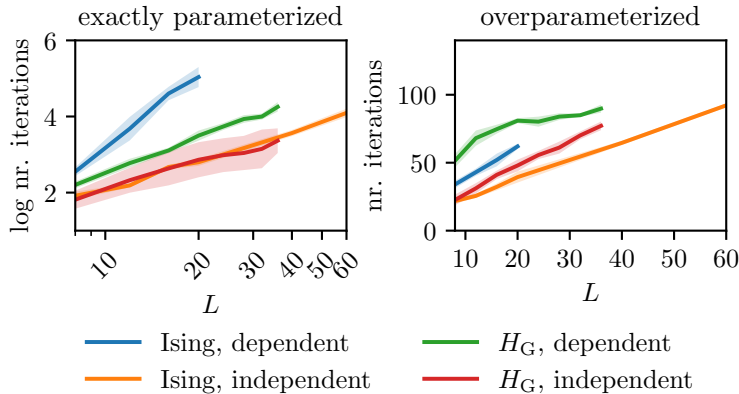


Figure 4.7: Number of iterations to converge vs. lattice size corresponding to the data in Figure 4.1. Solid line is the mean value, and the shaded area indicates the standard deviation. The legend refers to the Hamiltonian targeted and protocol used, in this order. The target Hamiltonians are either the Ising model, Eq. (4.2), or generic symmetric quadratic Hamiltonians, Eq. (4.3). The number of iterations to converge scales polynomially with system size when  $p = L/2$ . This turns into a linear scaling as the circuit enters the overparameterised regime (right).

of the state in the quantum computer harder given the increased circuit depth. Thus, as noise levels in a device decrease, increasing the depth of the circuit so that it is overparameterised might directly allow variational algorithms to take advantage of this. This has the caveat that when the number of parameters passes a certain threshold, the overhead associated with certain algorithms, such as BFGS, exceeds the advantage obtained from overparameterising the circuit; we quantify this in Section 4.3.2. In this case, algorithms designed to handle a large number of parameters, such as ADAM or stochastic gradient descent, should be employed instead.

In what follows, we propose and test an explanation for the phenomenon of overparameterisation in the case of gradient based optimisers. We argue that there is a change in the very properties of the parameterisation of the manifold as the circuit depth increases. A gradient based optimiser is an algorithm that, given an initial condition  $\theta_0$ , and defining  $e(\boldsymbol{\theta}) := e(|\psi(\boldsymbol{\theta})\rangle)$ , iterates the following update function

$$\boldsymbol{\theta}_{i+1} = \boldsymbol{\theta}_i - \eta A \nabla e(\boldsymbol{\theta}_i) \quad (4.9)$$

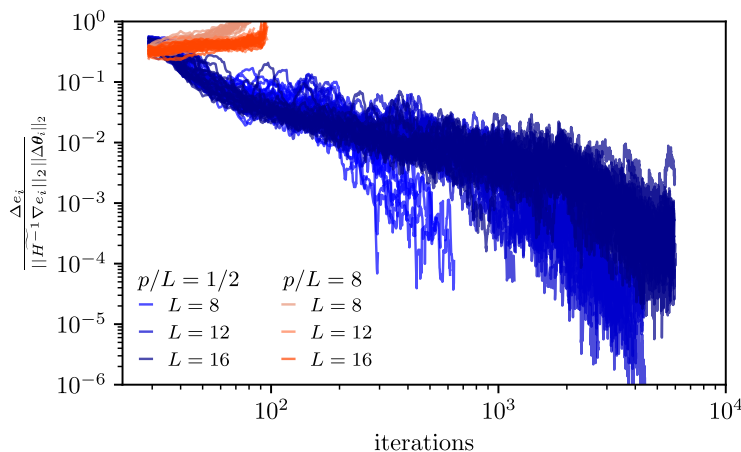


Figure 4.8: Quantification of how well the gradient accounts for the change in the cost function along the optimisation, both in the exactly parameterised ( $p = L/2$ ) and in the overparameterised ( $p/L = 8$ ) regimes. The plot shows the quantity defined in Eq. (4.10) recorded throughout the optimisation. We see that in the overparameterised regime, the value of the gradient consistently predicts the decrease in the cost function up to a constant factor; while it only accounts for a decreasing fraction of this variation in the exactly parameterised regime. Here, the target state was that of the Ising model with PBCs.

until it converges, that is, it can not find a value of  $\eta$  such that the update reduces the cost function  $e$ . Note that, here,  $i$  indexes the vector of angles at the  $i$ th iteration. The matrix  $A$  is a bias that provides extra information to the algorithm. It can be the inverse of the Hessian  $H^{-1}$  in the case of Newton based methods (or an approximation of it as in the case of quasi-Newton methods such as BFGS), or the inverse of the metric of the manifold being optimised over, as is done in e.g. Quantum Natural Gradient descent methods [179]. Importantly, the gradient of a function is a linear local approximation of the function at that point. While that means that, if  $\|\nabla e\| \neq 0$ , there is a value of  $\eta$  such that  $e(\boldsymbol{\theta}_{i+1}) < e(\boldsymbol{\theta}_i)$ , it does not offer any real guarantee about the actual change  $\Delta e_{i+1} = e(\boldsymbol{\theta}_i) - e(\boldsymbol{\theta}_{i+1})$ .

Here, we examine how good this local approximation is as the optimisation progresses, both when the circuit depth is equal to  $\hat{p}$  and in the overparameterised regime. We run the BFGS algorithm, and  $\eta$  is picked on a per-iteration basis by using the strong Wolfe conditions, an established heuristic based on a minimum descent criterion [138].

BFGS is a quasi-Newton method, and so  $A = \widetilde{H}^{-1}$  will be an approximation to the inverse of the Hessian. In Figure 4.8, we plot

$$l = \frac{\Delta e_i}{\|\widetilde{H}^{-1} \nabla e_i\|_2 \|\Delta \theta_i\|_2}, \quad (4.10)$$

which quantifies how much of the variation in the cost function can be attributed to the local approximation given by the gradient at the  $i$ th iteration. We see that in the overparameterised regime, most of the variation in the cost is accounted for by this approximation, leading to the exponential decay seen in Figure 4.1. We conclude that the overparameterised regime leads to parameterisations that are more amenable to optimisation, as they capture the variation in the cost for longer distances in the parameter space (see Figure 4.9).

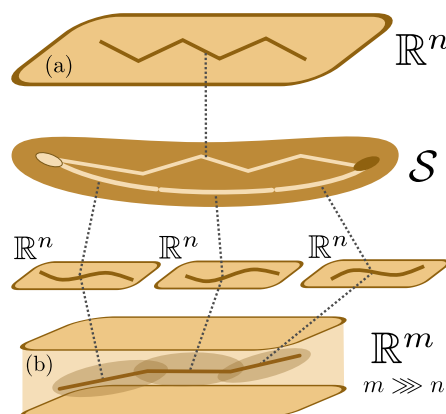


Figure 4.9: The parameterisation at minimal circuit depth  $\hat{p}$  (a) matches the dimension of the manifold of states. By the implicit function theorem, the overparameterisation (b) defines local, lower-dimensional parameterisations, also matching the dimension of the manifold. These more adequately capture its features, while describing the optimisation path in a piecewise manner. It is an open question whether a global parameterisation with these properties could be found.

### 4.3.2 Number of parameters and choice of optimisation algorithm

In Figure 4.10, we examine the effect of increasing the circuit depth on the total time taken to run an optimisation and on the time it would take to prepare these states on a quantum simulator (measured by the sum of the angles). We see that, despite

### 4.3 The overparameterised regime

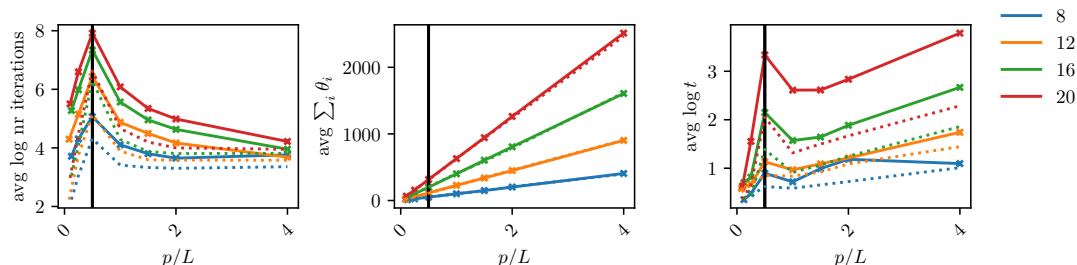


Figure 4.10: Different quantities characterising the hardness of the optimisation with increasing circuit depth. On the left, we plot the mean of the logarithm of the number iterations to converge; the centre plot depicts the mean of the sum of all the angles of the protocol, where periodicity is appropriately taken into account; on the right, the average of the logarithm of the total computational time is shown. Generic symmetric quadratic Hamiltonians were targeted, and results were averaged over 5 random states and 5 random initialisations per state. Filled line corresponds to the site-dependent protocol, while dotted line represents the site-independent protocol; these two cases essentially display the same behaviour. Periodic boundary conditions were used, and the black vertical line indicates  $p = L/2$ , the depth at which the circuit is exactly parameterised. These results were obtained on an Intel(R) Xeon(R) CPU E5-2650 v4 @ 2.20GHz.

increasing the circuit depth into the overparameterised regime making the optimisation easier, the sum of the angles in the protocol grows linearly with the circuit depth. Furthermore, we see that, despite the number of iterations to converge decreasing into the overparameterised regime, when one looks at the actual time taken to run the optimiser, there is an inflexion point where this number first goes down and then starts increasing again. This is due to the algorithm (BFGS) used, which stores an approximation to the Hessian; as the size of the Hessian increases, the computational cost associated to storing and manipulating it dominates the computational time. Thus, while it is feasible to use a larger class of optimisation algorithms at lower system sizes, as one increases the circuit depth, one has to switch to algorithms specialized to dealing with a large number of parameters e.g. ADAM or stochastic gradient descent.

## 4.4 Conclusion

In this chapter, we began by numerically computing the circuit depth  $\hat{p}$  needed to achieve maximum expressibility for the one-dimensional QAOA defined in Eq. (3.5). This is the circuit depth such that, if a state can be prepared at  $p > \hat{p}$  it can also be prepared at  $\hat{p}$ . In Chapter 3 we had denoted this set of states by  $\mathcal{S}$ , and we had determined it to be equal to the set of all fermionic Gaussian states under the Jordan-Wigner transformation for the one-dimensional QAOA. These states are efficient to simulate classically, as explained in Section 2.4; we exploited this in this chapter to systematically study the numerical optimisation of the associated parameterised circuit.

We observed that making the angles of the protocol dependent on the lattice sites makes the preparation of non-local Hamiltonians *easier*, and of local Hamiltonians *harder*, which is the opposite of what is observed when the angles are made to be independent of the lattice sites for each circuit layer. We argued that this is due to the symmetries in the system constraining the features available to the optimiser. This contrasts with the more common case where the use of symmetries in variational algorithms is beneficial [11, 101, 124, 144, 175], and points to there being circumstances where relaxing a symmetry in the circuit is desirable.

Further, we studied in detail the overparameterised regime, exploiting the larger system sizes and circuit depths accessible to us. We find that what is initially a polynomial scaling in the number of iterations to converge to the solution with lattice size turns into a linear scaling. Moreover, we found that the number of iterations to converge to the solution begins by sharply decreasing with the depth of the circuit, before tapering off and saturating at a depth  $p \propto L^2$ . This indicates that we do not need large circuit depths much past the threshold  $\hat{p}$  to benefit from overparameterisation, and that even circuit depths just beyond this value can result in significant improvements. We also note that the saturation depth of  $p \propto L^2$  scales quadratically with the size of the lattice, which contrasts with the linear scaling of the quantities in Table 3.1 for the site-independent case. This indicates that the dimension of the Lie algebra or of the manifold of states  $\mathcal{S}$  can not in general be used to predict this saturation point. Overall, the above results can help better design variational algorithms to take advantage of overparameterisation.

The parameterised circuits we have studied could be used to help benchmark variational algorithms in quantum computers, as free-fermionic systems can be classically

simulated in a noiseless, ideal environment for large system sizes. This type of study has already been performed in a non-variational setting using certain fermionic Gaussian states such as, e.g., Majorana zero modes [181] or the ground state of the Ising model [32]. Moreover, this could potentially be leveraged into error correcting methods by comparing the results from classically simulating a variational algorithm that can be expressed in terms of free-fermions with the results obtained from running the same algorithm on a noisy quantum computer, similarly to what is done in [127].

In addition, our results provide a framework to better understand the theory behind the preparation of fermionic Gaussian states using variational algorithms, already studied in models such as the Ising model [47, 78], the Kitaev model in the exactly solvable limit [86], or the cluster model [139]. Importantly, while there are established algorithms to build circuits that prepare FGS [88, 96], these require a full description of the corresponding covariance matrix; a variational approach is relevant where this structure is not known beforehand e.g. when approximating interacting states [115, 139] or maximising a quantity of interest such as magic [76, 143].

---

# CHAPTER 5

---

Effect of interactions on state preparation with  
variational quantum algorithms

## 5.1 Preparing the ground state of non-integrable quantum models

---

In Chapter 3, we studied the expressibility of variational algorithms and found that the 1D QAOA is able to prepare exactly all free-fermionic states. In Chapter 4, we leveraged this to comprehensively study the associated optimisation. While free-fermions are able to capture important phenomena in quantum many-body physics, such as being able to host certain topological phases of matter, they represent a set of models which are not only integrable but also efficient to simulate classically. While these properties greatly simplify their study, it also means that they generally fail to adequately capture most complex quantum many-body phenomena.

In this chapter, we address the problem of using a variational algorithm to prepare the ground state of a number of models depending on tunable parameters  $H(h_1, h_2, \dots)$ , where  $H$  is non-integrable for general values of  $h_1, h_2, \dots$ . We are interested in predicting the relative success of state preparation across the phase diagram defined by the parameters; moreover, our aim is to relate the success of preparation to some physical property of the target state. Our main contribution is as follows: we find that, ultimately, the quality of state preparation correlates with the interaction distance [192], introduced in Section 2.6. Our findings are numerically supported by examples of non-integrable quantum models, and we show that the *slope* of this cross-correlation can be used to identify the existence of different phases in the model.

### 5.1 Preparing the ground state of non-integrable quantum models

In this section, we address the problem of using a variational algorithm to prepare the ground state of a number of non-integrable models. Throughout, the models under study take the form

$$H = \sum_{j=1}^m h_j H_j, \quad (5.1)$$

where the  $h_j$  are a set of tunable parameters. An immediate question is how to choose an appropriate variational protocol to tackle this problem, as the ones we have studied in Chapters 3, 4 are not expressible enough to prepare non free-fermionic quantum states. The approach we take is to split the Hamiltonian into individual non-commuting terms

---

## 5.1 Preparing the ground state of non-integrable quantum models

to form the protocol

$$\mathcal{P} = (H_1, \dots, H_m), \quad (5.2)$$

a method known as the Hamiltonian Variational Ansatz (HVA) [204, 210], which we first introduced in Section 3.1. This provides us with a guarantee that, as  $p \rightarrow \infty$ , the algorithm can prepare the ground state of the model regardless of the values of the controllable parameters  $h_j$ . This is because, following the framework developed in Section 3.2, the components of the Hamiltonian then comprise the generators of the Lie algebra associated to the protocol; and so, this Hamiltonian is trivially contained in this algebra (in fact, the Lie algebraic construction of variational protocols can be seen as a generalisation of the HVA).

In what follows, we study the variational preparation of the ground state of the transverse and longitudinal field Ising model [5.1.1], the three-spin Ising model [5.1.2] and the cluster Ising model [5.1.3]. In all cases, we take the cost function to be the quantum infidelity,

$$1 - f \equiv 1 - |\langle \psi_{\text{target}} | \psi(\boldsymbol{\theta}) \rangle|^2, \quad (5.3)$$

which is bounded between 0 and 1. Although evaluating fidelity in experiment is impractical or even impossible, it is useful in numerical simulations where the target state is known. The initial state of the protocol is taken to be the ground state of  $-\sum_{j=1}^L X_j$ , i.e., all spins polarized along  $x$ -direction,  $|\psi_{\text{init}}\rangle = |\rightarrow \dots \rightarrow\rangle$ .

### 5.1.1 Transverse and longitudinal field Ising model

Here, our target Hamiltonian will be the one-dimensional quantum Ising model in the presence of both transverse and longitudinal fields, which we first introduced in Section 2.7,

$$H = -\sum_{j=1}^L (\pm 1) Z_j Z_{j+1} - h_x \sum_{j=1}^L X_j - h_z \sum_{j=1}^L Z_j, \quad (5.4)$$

where we assume periodic boundary conditions. Note that, despite the spins in (5.4) being rotated compared to the model introduced in Section 2.7, these are equivalent. The model is either ferromagnetic (FM) or antiferromagnetic (AFM) depending on

## 5.1 Preparing the ground state of non-integrable quantum models

---

whether the coupling of the first term is chosen to be  $+1$  or  $-1$ , respectively. The Ising models in Eqs. (5.4) serve as a useful laboratory for studying a number of phenomena in condensed matter physics [36, 50, 129]. The properties of the ground state of the model in Eq. (5.4) are insensitive to the sign of the FM/AFM coupling in the absence of the longitudinal field  $h_z$ . However, once  $h_z > 0$ , the phase diagram is substantially different for the two models. The FM model has a critical point at  $(h_x, h_z) = (1, 0)$ , while the AFM model has a critical line connecting the point  $(h_x, h_z) = (1, 0)$  with the point  $(h_x, h_z) = (0, 2)$ . The critical line is not known analytically, but it has been determined numerically using density-matrix renormalization group simulations in Ref. [146].

The phase diagrams of the FM and AFM models in their ground state, as diagnosed by the value of the interaction distance  $D_{\mathcal{F}}$  (introduced in Section 2.6) are shown in Fig. 5.1(a)-(b), respectively. The ground state of the Hamiltonian in Eq. (5.4) is obtained numerically using exact diagonalization, and its entanglement spectrum is computed by partitioning the system into two equal halves. From the entanglement spectrum,  $D_{\mathcal{F}}$  is evaluated by numerical optimisation as described in Section 2.6. For both models,  $D_{\mathcal{F}}$  is found to be zero (to machine precision) when  $h_z = 0$ , regardless of the value  $h_x$ . This agrees with the findings in [78] and the study in Chapter 3. Away from this line,  $D_{\mathcal{F}}$  is a sensitive indicator of interaction effects and changes by many orders of magnitude depending on the location in the phase diagram. For example, in the FM model,  $D_{\mathcal{F}}$  exhibits a sharp peak just off the free Ising critical point,  $(h_x = 1, h_z = 0)$ . While the Ising critical point is described by the free Ising conformal field theory [63], and thus it has  $D_{\mathcal{F}} = 0$ , the properties of this CFT change dramatically once  $h_z$  field is introduced [214]. This is consistent with the fermionic picture, where the  $h_z$  field introduces long-range interaction between fermions after the Jordan-Wigner transformation, which makes the system's ground state highly interacting. Somewhat surprisingly, away from the critical point, the value of  $D_{\mathcal{F}}$  sharply decays to values as low as  $\sim 10^{-7}$ , even though the interaction is comparable in magnitude to other terms in the Hamiltonian. This implies that there are large regions of the phase diagram where the ground state of the system is effectively free-fermion-like, even though the Hamiltonian itself is “interacting”. On the other hand, the AFM model features a critical line that extends from the free Ising critical point  $(h_x = 1, h_z = 0)$ . While  $D_{\mathcal{F}} = 0$  at  $(h_x = 1, h_z = 0)$ , the value of interaction distance progressively increases along the critical line towards the interior of the phase diagram – see Fig. 5.1(b).

## 5.1 Preparing the ground state of non-integrable quantum models

---

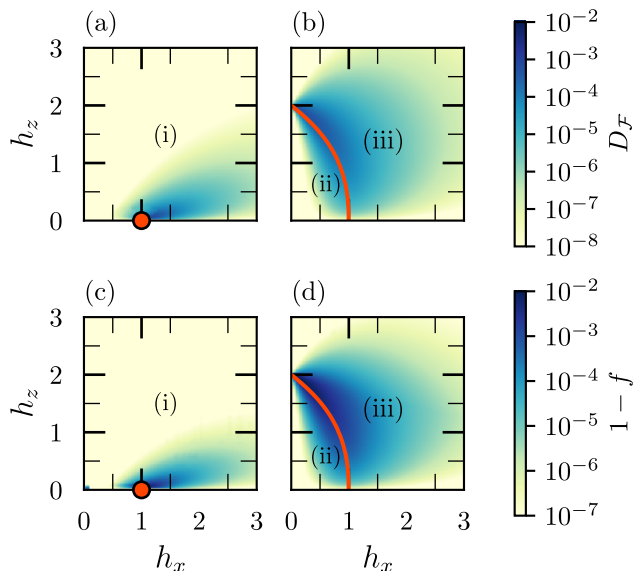


Figure 5.1: Top row: Interaction distance for the ground state of FM (a) and AFM (b) model in Eq. (5.4) as a function of fields  $h_x$  and  $h_z$ . Bottom row: the infidelity  $1 - f$  between the prepared state and the ground state for the FM (c) and AFM model (d). See text for the details of the variational protocol. All data is for system size  $L = 8$  using PBCs. Red dot denotes the critical point of the FM model, which is in a ferromagnetic phase (i) throughout the diagram, while the red line is the critical line in the AFM model according to Ref. [146] separating an antiferromagnetic phase (ii) from a paramagnetic phase (iii).

As discussed in the beginning of this section, the variational protocol used will be  $\mathcal{P} = (H_1, H_2, H_3)$ , with

$$H_1 = - \sum_{j=1}^L Z_j, \quad (5.5)$$

$$H_2 = - \sum_{j=1}^L X_j, \quad (5.6)$$

$$H_3 = - \sum_{j=1}^L Z_j Z_{j+1}, \quad (5.7)$$

obtained from splitting the problem Hamiltonian and illustrated in Figure 5.2. Note that the operators  $H_j$  satisfy  $e^{-i(\theta+\pi)H_j} \propto e^{-i\theta H_j}$ . Indeed,  $H_j = - \sum_{k=1}^L P_k$ , where  $P_k$

## 5.1 Preparing the ground state of non-integrable quantum models

---

are tensor products of single-site Pauli operators, and a well-known identity is that

$$e^{i\theta P_k} = \cos(\theta)I + \sin(\theta)P_k. \quad (5.8)$$

This implies that  $e^{i(\theta+\pi)P_k} = -e^{i\theta P_k}$ , hence,

$$e^{-i(\theta+\pi)H_j} = \prod_{k=1}^L e^{i(\theta+\pi)P_k} = (-1)^L \prod_{k=1}^L e^{i\theta P_k} = (-1)^L e^{-i\theta H_j}. \quad (5.9)$$

As a consequence, in what follows, we restrict the angles  $\theta$  to the  $[0, \pi)$  interval by disregarding the resulting phase. We further restrict the angles  $\theta_{j,3}$  associated with  $H_3$  to the  $[0, \frac{\pi}{2})$  interval, since

$$\prod_{k=1}^L e^{-i(\theta+\frac{\pi}{2})Z_k Z_{k+1}} = \prod_{k=1}^L Z_k Z_{k+1} \prod_{k=1}^L e^{i\theta Z_k Z_{k+1}} \quad (5.10)$$

$$= \prod_{k=1}^L e^{i\theta Z_k Z_{k+1}}. \quad (5.11)$$

The equality (5.10) comes from the fact that

$$e^{i(\theta+\frac{\pi}{2})Z_k Z_{k+1}} = \cos\left(\theta + \frac{\pi}{2}\right)I + \sin\left(\theta + \frac{\pi}{2}\right)Z_k Z_{k+1} \quad (5.12)$$

$$= \sin(-\theta)I + \cos(-\theta)Z_k Z_{k+1} \quad (5.13)$$

$$= Z_k Z_{k+1}(\cos(-\theta) + \sin(-\theta)Z_k Z_{k+1}), \quad (5.14)$$

while the equality (5.11) is due to the fact that  $\prod_{j=1}^L Z_j Z_{j+1} = I$ , as for each lattice site two  $Z$  operators get multiplied, and the product of any Pauli operator with itself is the identity.

The initial guesses for the angles were determined sequentially as  $p$  is increased, following the method in Appendix B1 of Ref. [215]. For minimisations involved in both the variational algorithm and  $D_{\mathcal{F}}$ , we use a basinhopping algorithm with a Metropolis acceptance criterion [201], as implemented in the Python package `scipy.optimize.basinhopping`. This is an optimisation strategy that performs multiple minimisations, taking as the initial condition for the next minimisation the stochastically perturbed result of the previous one. This allows us to avoid the local minima associated with the rugged landscapes of both the variational algorithm and  $D_{\mathcal{F}}$ , as discussed further

## 5.1 Preparing the ground state of non-integrable quantum models

---

in Sec. 5.3. This, however, was not enough to completely eliminate local minima, and all the data presented here required two additional rounds of minimisation. Each of these consisted in running the basinhopping algorithm across the phase diagram again, this time using as initial value for each point the optimal values of each of the adjacent points from the previously obtained data, and keeping the minimum value found.

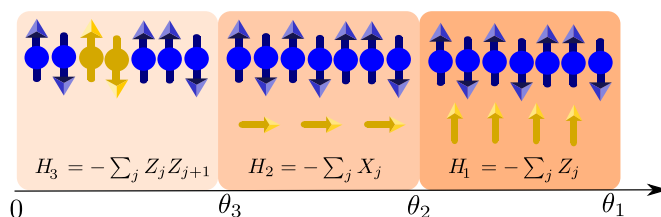


Figure 5.2: An  $m = 3$ -step variational algorithm for the preparation of the ground state of the Ising model in both transverse and longitudinal fields, discussed in Sec. 5.1.

Note that our protocol is a generalisation of the one considered in Ref. [78], which was restricted to the purely transverse field ( $h_z = 0$ ), and made use of a 2-step ansatz with only  $H_2$  and  $H_3$  (this is the symmetric 1D QAOA protocol we studied in Chapters 3 and 4). In that case, both the Hamiltonian and the protocol conserve the total fermion parity, generated by  $P = \prod_{j=1}^L X_j$ . This symmetry is broken once the  $z$ -field is introduced and the ground state acquires a non-zero magnetization  $\langle \psi | \sum_{j=1}^L Z_j | \psi \rangle \neq 0$ . While it is easy to come up with a two-step protocol that does not conserve parity, we have not been able to find one that accurately prepares the ground state for general values of  $(h_x, h_z)$ .

In Figs. 5.1(c)-(d) we present results of the variational protocol across the phase diagram  $(h_x, h_z)$ . The colour scale in Fig. 5.1(c)-(d) shows the infidelity  $1 - f$  between the prepared state and the ground state obtained after fixed  $p = \frac{L}{2}$  steps. We observe that this metric of ground state preparation looks remarkably similar to the behaviour of  $D_{\mathcal{F}}$  in Figs. 5.1(a)-(b). In particular, we recover  $f = 1$  when  $h_z = 0$  [78], while the variational algorithm no longer finds an exact ground state when  $h_z > 0$ . Nevertheless, it approximates the ground state very closely when  $D_{\mathcal{F}}$  is small. Once again, it is easy to see that in this case there is no clear relation between  $1 - f$  and the VNE of the ground state. For example, in the FM model, the VNE should be largest at the critical point; further, as adding  $h_z$  opens a gap in the spectrum, increasing this parameter should reduce the VNE, as its scaling changes from logarithmic divergence with system

## 5.1 Preparing the ground state of non-integrable quantum models

---

size to an area law. However, from the point of view of the variational algorithm, we find precisely the opposite: it is harder to prepare the state with some small amount of  $h_z$  compared to  $h_z = 0$ .

Examining the optimal angles found at each point of the phase diagram of both the FM/AFM Ising models when running the protocol in Eqs.(5.5)-(5.7), we found no continuous variation of the angles across the phase diagram of the kind, e.g., in Ref. [215], where it was observed that plotting the optimal angles  $\theta_{k,j}$  for a fixed  $j$  against the circuit depth  $k$  results in a smooth function as  $L$  increases. In Fig. 5.3, we show a scatter plot of  $D_{\mathcal{F}}$  vs.  $1 - f$  from the data extracted from phase diagrams such as in Fig. 5.1, but using different numbers of steps  $p$ , indicated in the legend. In both FM and AFM models, we expect correlation between  $D_{\mathcal{F}}$  and  $1 - f$  around  $p = \frac{L}{2}$ . This correlation peak is relatively broad as  $p$  is increased further. Eventually, as  $p \rightarrow \infty$ , we expect states to be exactly prepared and this correlation to break down, as in this limit our protocol should have the same power as quantum annealing with an arbitrary schedule ([119], see also Section 3.2). In the opposite limit, as  $p \rightarrow 1$ , we expect that the variational method, in general, is not powerful enough for a correlation to emerge. However, in special cases such as the FM model, we see that  $D_{\mathcal{F}}$  and  $1 - f$  are correlated even at lower  $p$ . We compute the Pearson correlation coefficients for the data in Fig. 5.3 and discuss them in Section 5.1.4; as expected, the Pearson coefficient jumps to a value close to 1 around  $p = \frac{L}{2}$ .

For the AFM Ising model in Fig. 5.3(ii)-(iii), we found that the correlation between  $D_{\mathcal{F}}$  and  $1 - f$  follows a different slope in the two phases of the AFM model separated by the critical line in Fig. 5.1(b),(d). In particular, the behaviour in the ordered phase of the model, Fig. 5.3(ii), clearly illustrates that the correlation between  $D_{\mathcal{F}}$  and  $1 - f$  only starts to emerge around  $p = L/2$ . Moreover, different slopes of the correlation in the two phases suggest that by carefully examining the correlation between these two metrics one could infer about the existence of different phases in models with unknown phase diagrams.

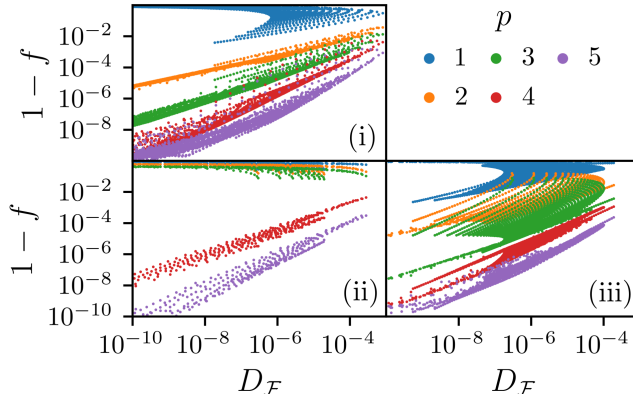


Figure 5.3: (i) Scatter plot of interaction distance  $D_{\mathcal{F}}$  against  $1 - f$  for the FM Ising model from Fig. 5.1(a),(c). (ii)-(iii): Analogous plot for the AFM Ising model in Fig. 5.1(b),(d), where the data points are taken from the antiferromagnetic (ii) or paramagnetic (iii) phase. Data is for  $L = 8$  spins with PBCs and different values of  $p$  indicated in the legend.

### 5.1.2 Three-spin Ising model

Here we demonstrate that our findings also apply in a different model featuring three-spin interactions. The model is defined by the Hamiltonian

$$H = - \sum_{j=1}^L Z_j Z_{j+1} Z_{j+2} - h_x \sum_{j=1}^L X_j - h_z \sum_{j=1}^L Z_j, \quad (5.15)$$

where, again, we assume PBCs. The critical behaviour of this model is in the same universality class as the two-dimensional classical three-state Potts model [63], and its ground state is much harder to prepare than that of the quantum Ising model. Its phase diagram has been mapped out in Ref. [153] (see also Ref. [83] for further generalisations of the model). In the  $h_x > 0$ ,  $-3 \leq h_z < 0$  region, it contains a critical line connecting  $(h_x, h_z) = (0, -3)$  to  $(h_x, h_z) = (1, 0)$ . Below that critical line, corresponding to region (ii) in Figure 5.4, there exists a threefold ground state degeneracy, while above it, corresponding to region (i) in the same figure, the ground state is unique.

The motivation for studying the model in Eq. (5.15) is that its ground state is expected to be more strongly interacting and have a higher value of  $D_{\mathcal{F}}$ . Indeed, the 3-fold ground state degeneracy in the ordered phase gives rise to an approximate 3-fold

## 5.1 Preparing the ground state of non-integrable quantum models

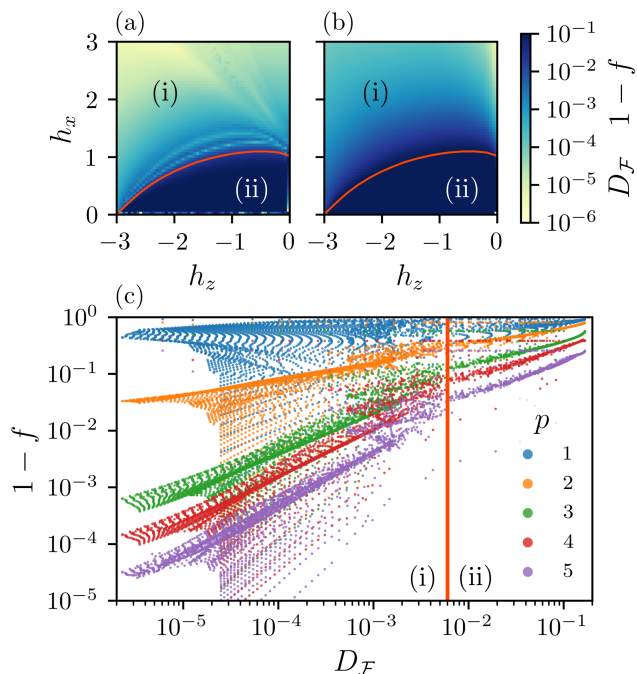


Figure 5.4: Top row: Interaction distance for the 3-spin Ising model in Eq. (5.15) as a function of fields  $h_x$  and  $h_z$  (a) and the infidelity  $1-f$  (b). The protocol is based on Eqs. (5.5), (5.6), (5.17). All data is for system size  $L=9$  using PBCs. Red line is the critical line in the 3-spin Ising model according to Ref. [153] Bottom row: Scatter plot of  $D_{\mathcal{F}}$  against  $1-f$  for the 3-spin Ising model, system size  $N=9$  and different values of  $p$  indicated in the legend. Vertical red line, drawn heuristically, separates the data belonging to the phase above and below the critical line (respectively to the left and right of the vertical line).

degeneracy of the entanglement spectrum, as generally found in “symmetry-protected topological phases” [163]. This can be understood by picking a point ( $h_x=0, h_z=-1$ ), where the exact ground state of the system (with zero momentum under translation) is given by

$$|\psi_0\rangle = \frac{1}{\sqrt{3}}(|\uparrow\downarrow\uparrow\downarrow\uparrow\downarrow\dots\rangle + |\downarrow\uparrow\downarrow\uparrow\downarrow\dots\rangle + |\downarrow\downarrow\uparrow\downarrow\uparrow\dots\rangle). \quad (5.16)$$

The corresponding entanglement spectrum is given by  $\rho_k = \{\frac{1}{3}, \frac{1}{3}, \frac{1}{3}, 0, 0, \dots\}$ . This is the type of entanglement spectrum that gives  $D_{\mathcal{F}} = \frac{1}{6}$ , a value close to the upper bound  $3 - 2\sqrt{2}$  [122], as explained in Section 2.6. An approximate 3-fold degeneracy in the

## 5.1 Preparing the ground state of non-integrable quantum models

---

entanglement spectrum persists throughout the ordered phase of the model; thus we expect the ground state throughout this phase to be more difficult to prepare using QAOA compared to the disordered phase.

The comparison between  $D_{\mathcal{F}}$  and the variational algorithm for the model in Eq. (5.15) is shown in Fig. 5.4. The protocol was chosen such that  $H_1$  and  $H_2$  are defined as in Eqs. (5.5)-(5.6), but for  $H_3$  we use

$$H_3 = - \sum_{j=1}^L Z_j Z_{j+1} Z_{j+2} \quad (5.17)$$

so that the protocol satisfies  $H_3 + h_x H_2 + h_z H_1 = H$ . We have found that, like the two-spin Ising model, the success of the protocol also correlates well with interaction distance, as we see in the top row of Fig. 5.4. Here, as in Section 5.1, minimisations are done using a basinhopping algorithm, and the results required two additional rounds of minimisation. Moreover, we find correlation between  $D_{\mathcal{F}}$  and  $1 - f$  for several values of  $p$ , as shown in the bottom row of Fig. 5.4. As before, the data in the bottom row of Fig. 5.4 was obtained by sampling across the entire phase diagram in the top row of Fig. 5.4.

It is worth noting that we can prepare the ground state in Eq. (5.16) exactly by choosing the protocol  $H_2 = - \sum_j Z_{j-1} Z_j Z_{j+1}$  and  $H_1 = - \sum_j (X_j X_{j+1} + Y_j Y_{j+1})$ , while the initial state is the ground state of  $H_2$  in the sector with magnetization  $-N/3$ , as this is the sector where the states  $\{|\uparrow\downarrow\downarrow \dots\rangle, |\downarrow\uparrow\downarrow \dots\rangle, |\downarrow\downarrow\uparrow \dots\rangle\}$  live. It can be verified that this protocol prepares the exact ground state in Eq. (5.16) in  $N/2$  steps. Moreover, supplementing the protocol with a third operator,  $H_3 = - \sum_j X_j$ , leads to good results across the entire phase with the 3-fold ground-state degeneracy. However, the infidelity  $1 - f$  of the latter protocol does not capture the phase transition in a way that the protocol [Eqs.(5.6), (5.5), (5.17)] does. Moreover, the initial state is more difficult to prepare in this case, unlike the product state of spins in our protocol.

Similar to the models studied in Sec. 5.1, we found no continuous variation of angles in the three-spin Ising model, and the angles  $\theta_{k,1}$  tended to be close to multiples of  $\pi/2$  (see Fig. 5.7). However, in this case the heuristic arguments of Sec. 5.2 do not directly apply as the Gaussianity of the protocol is broken by the triple spin interaction term (5.17). It is an interesting open problem to analytically explain the approximate Gaussianity in the regions where interaction distance is close to zero in this case.

### 5.1.3 Non-integrable Cluster Ising model

Here, we study the model that realises the so-called cluster state [25], which is of importance in measurement-based quantum computation [134] and also in symmetry-protected topological phases of matter [33, 61, 163, 172]. Note that, unlike the related model defined in Eq. (4.8) and studied in Section 4.2.1, the model we now introduce is non-integrable. It displays a critical line in its phase diagram when placed in an external magnetic field, like the AFM model, and we demonstrate similar correlation between the interaction distance and variational preparation of its ground state. It is defined in terms of Pauli matrices (assuming periodic boundary conditions) as

$$H = - \sum_{j=1}^L X_{j-1} Z_j X_{j+1} - h_{yy} \sum_{j=1}^L Y_j Y_{j+1} + h_y \sum_{j=1}^L Y_j. \quad (5.18)$$

When  $h_y = 0$ , the model can be solved using a combination of Jordan-Wigner/Bogoliubov transformations [178], but for general values of  $h_y$  the model is not solvable. It has a critical line described by a conformal field theory with central charge  $c = 3/2$ , connecting the points  $(h_{yy} = 1, h_y = 0)$  and  $(h_{yy} = 0, h_y = 1)$ . The critical line has been mapped out using density-matrix renormalisation group calculations in Ref. [197].

As seen in Fig. 5.5(a)-(b), both the variational algorithm and  $D_{\mathcal{G}}$  are highly sensitive to the critical line, just like we have previously seen in the AFM Ising and 3-spin Ising models. Despite small system size, the critical behaviour is in good qualitative agreement with results of Ref. [197]. The protocol in Fig. 5.5 has been defined by splitting  $H$  into its three components

$$H_1 = - \sum_j^L Y_j, \quad (5.19)$$

$$H_2 = - \sum_j^L Y_j Y_{j+1}, \quad (5.20)$$

$$H_3 = - \sum_j^L X_{j-1} Z_j X_{j+1}. \quad (5.21)$$

For the initial state, one can choose the ground state of  $H_1$ . However, with this initial state, the convergence of the optimisation below the critical line, in region (ii) in Figure 5.5, was found to be very slow. The convergence is considerably more robust

## 5.1 Preparing the ground state of non-integrable quantum models

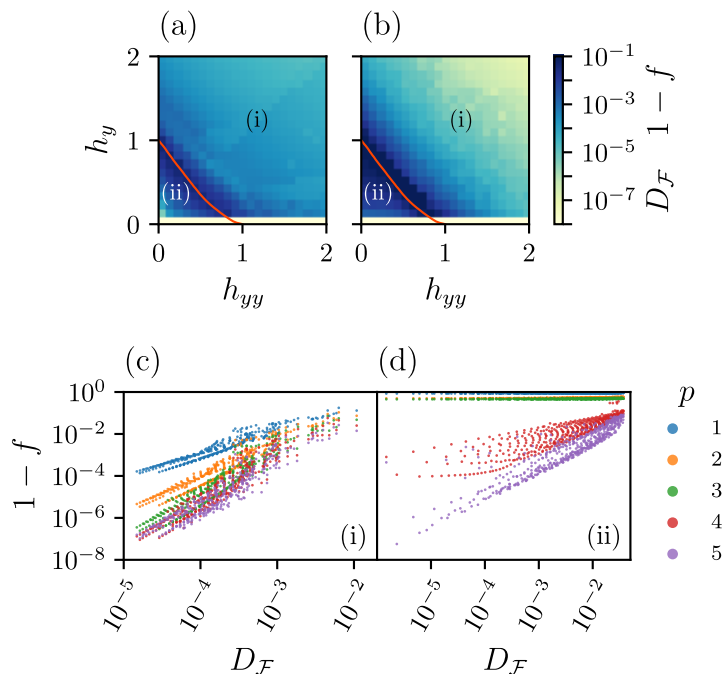


Figure 5.5: Top row: Interaction distance for the cluster Ising model in Eq. (5.18) as a function of  $h_{yy}$  and  $h_y$  (a) and the infidelity  $1 - f$  of the protocol (b). All data is for system size  $L = 8$  with periodic boundary conditions. Critical line, in red, is reproduced from Ref. [197] and separates a cluster phase (i) from a paramagnetic phase (ii). Bottom row: Scatter plot of  $D_{\mathcal{F}}$  against  $1 - f$  for the cluster Ising model, system size  $L = 8$  and different values of  $p$  indicated in the legend. Panel (c) shows points in region (i) while (d) shows points in region (ii).

if we use as initial state the ground state of  $H_2$  in this regime instead. In producing the phase diagram in Fig. 5.5(b) we have run two sweeps of QAOA starting in either of these initial states, and plotting the smaller value of the obtained  $1 - f$ .

It is worth noting that the line with  $h_y = 0$  is prepared *exactly* (to machine precision) in  $p = L/2$  steps using the 2-step protocol involving only  $H_3$  and  $H_2$ , similar to the case of the transverse field Ising model. Moreover, there is correlation between  $D_{\mathcal{F}}$  and  $1 - f$  across each of the two phases of the model, as illustrated in Fig. 5.5(c)-(d).

## 5.1.4 Additional data

We compute the Pearson correlation coefficients for the data in Figs 5.3, 5.4(c) and 5.5(c)-(d), and plot them in Fig. 5.6. We see that the Pearson coefficient is close to 1 around  $p = L/2$ , indicating direct correlation. We expect this to mark the beginning of a broad plateau where the Pearson coefficient remains close to 1, until it eventually starts to drop at larger values of  $p$ . The reason for this decay is the exact preparation of the state in the limit  $p \rightarrow \infty$  for the protocol considered here. Conversely, in the limit  $p \rightarrow 1$ , we expect that, in general, the variational ansatz is not sufficiently powerful for the correlation to emerge.

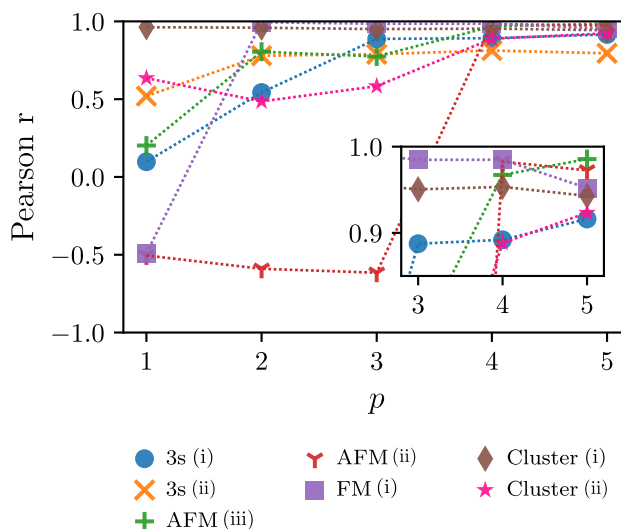


Figure 5.6: Pearson correlation coefficients as a function of  $p$ . Labels "FM" and "AFM" refer to the data for the ferromagnetic and antiferromagnetic models in Figures 5.3, "3s" refers to the data for three-spin model in 5.4(c) and "Cluster" refers to the data for the cluster model in 5.5(c). The inset zooms in on the top-right corner of the plot.

## 5.2 Relation between variational algorithms and interaction distance

In Sec. 5.1, we have numerically established a correlation between  $D_{\mathcal{F}}$  and the success of variational protocols. This suggests that the protocol's success depends on how close

## 5.2 Relation between variational algorithms and interaction distance

---

to being Gaussian (in the sense of Eq. (2.46)) the target ground state is. In this section, we support these numerical observations with analytic arguments. We will first focus on the case of the transverse and longitudinal field Ising model studied in Section 5.1.1.

Note that a shift of  $\pi/2$  in the  $\theta_{k,1}$  part of the protocol results in an overall parity flip, as easily seen from the following sequence of identities:

$$\exp\left(i\left(\theta_{k,1} + \frac{\pi}{2}\right)\sum_j Z_j\right) \exp\left(i\theta_{k,2}\sum_j X_j\right) \quad (5.22)$$

$$= \exp\left(i\theta_{k,1}\sum_j Z_j\right) \prod_j Z_j \exp\left(i\theta_{k,2}\sum_j X_j\right) \quad (5.23)$$

$$= \exp\left(i\theta_{k,1}\sum_j Z_j\right) \exp\left(i\theta_{k,2}\sum_j -X_j\right) \prod_j Z_j. \quad (5.24)$$

Further,

$$\prod_j Z_j |\rightarrow \dots \rightarrow\rangle = |\leftarrow \dots \leftarrow\rangle, \quad (5.25)$$

where  $|\rightarrow\rangle, |\leftarrow\rangle$  denote the eigenstates of  $X$ . This implies that, if we have the freedom of choosing either  $|\rightarrow \dots \rightarrow\rangle$  or  $|\leftarrow \dots \leftarrow\rangle$  as the initial state, we can restrict, without loss of generality, all angles  $\theta_{k,1}$  to an interval of length  $\pi/2$ . Moreover, we found that, after enforcing this restriction, the optimal angles  $\theta_{k,1}$  had a striking tendency to be very close to multiples of  $\frac{\pi}{2}$  (see Fig. 5.7), and can thus all be mapped to be close to 0.

Since both  $|\rightarrow \dots \rightarrow\rangle$  and  $|\leftarrow \dots \leftarrow\rangle$  are product states, they are also fermionic Gaussian states. Moreover, the evolution under the unitaries generated by  $H_3$  and  $H_2$  maps fermionic Gaussian states into fermionic Gaussian states, while the evolution under  $H_1$  spoils this property. However, for  $\theta_{k,1}$  close to 0, the evolution under  $H_1$  introduces only a small, perturbative deviation from a Gaussian state. Added to the fact that the interaction distance can predict the success of the algorithm, this suggests that the Hamiltonian  $H_1$  has a restricted role in the evolution, since this is the only Hamiltonian in the protocol that is not quadratic (and thus can lead to the preparation of states that are not fermionic Gaussian).

This heuristically accounts for the high correlation with interaction distance of the target state, as the states prepared are close to being free. As  $p$  gets larger, more perturbations are possible and the success variational algorithm increases. At a

## 5.2 Relation between variational algorithms and interaction distance

---

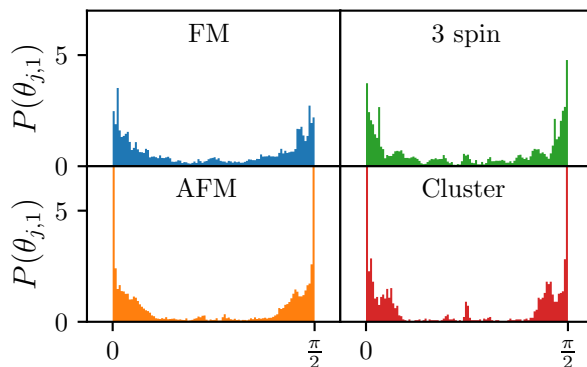


Figure 5.7: Distribution of angles  $\theta_{k,1}$  associated with the Hamiltonian in Eq. (5.5) across phase diagrams of FM/AFM, 3-spin and cluster Ising models in Eqs. (5.4), Eq. (5.15) and Eq. (5.18). Data is for system size  $L = 8$  with the exception of  $L = 9$  for the 3-spin Ising model. In all the plots,  $p = 4$ .

fixed  $p$ , this success is related to the distance of the target state from the Gaussian state manifold. Thus, the symmetry which led us to use a 3-step protocol for the transverse and longitudinal field Ising model could perhaps be broken in a simpler way by substituting either  $H_2$  or  $H_3$  by a non-quadratic Hamiltonian and doing away with  $H_1$ . Furthermore, this property could be exploited by having the initial guess be close to multiples of  $\frac{\pi}{2}$  through an ansatz, or by giving higher weight to regions close to these two points (0 and  $\frac{\pi}{2}$ ) in the minimisation algorithm.

While the analysis above can be directly adapted to case of the non-integrable cluster Ising model in Section 5.1.3, for which the  $H_3$  (5.21) is a quadratic Hamiltonian after applying the Jordan-Wigner transformation, this is not the case for the three-spin Ising model in Section 5.1.2. Recall, however, that interaction distance is computed in terms of fermionic modes that are, in general, not the ones defined on the underlying lattice using the Jordan-Wigner transformation, as explained in Section 2.6. The fact that the interaction distance captures the success of the variational algorithm in this case suggests that there could be fermionic modes for which the  $H_3$  (5.17) used in this model is quadratic, in which case the analysis above would apply. More generally,  $H_2$  and  $H_3$  could be generating a “small” Lie algebra (see Chapter 4), and introducing  $H_1$  extends the expressibility of the protocols by adding another generator.

We conclude that there is a practical limitation to the “natural” protocol proposed in Sec. 5.1, which was obtained as a Trotter splitting of the model Hamiltonians into

translation invariant components: the protocol is unable to prepare ground states that are far from being Gaussian (as measured by interaction distance). This limitation seems to be fundamentally related to the probability spectrum of the target state, i.e., the eigenvalue spectrum of its reduced density matrix. Indeed, when performing the optimisation using as a cost function the relative entropy [135] between the probability spectra of the trial state and of the target state, one finds heat maps similar to those in Fig. 5.1 (data not shown). Thus, there is a correlation between the success of the variational algorithm and  $D_{\mathcal{F}}$ , even though the former minimises the overlap of two vectors, while the latter employs a minimisation using the probability spectrum of the subsystem’s reduced density matrices.

### 5.3 Optimisation landscape

In this section, we explore the minimisation landscape of the optimisation problem studied in Sec. 5.1 for the AFM Ising model. The target state in the cost function is taken to be the ground state of the Hamiltonian at a set of representative points in the  $(h_x, h_z)$  phase diagram,

$$S = \{(0.1, 0.1), (0.1, 2), (1, 1), (2, 0.1), (2, 2)\}. \quad (5.26)$$

These points are drawn from regions of both “hard” and “easy” state preparation according to Fig. 5.1. Here, we use the rescaled relative energy as the cost function [118, 148]

$$\epsilon \equiv \frac{\langle \psi(\boldsymbol{\theta}) | H | \psi(\boldsymbol{\theta}) \rangle - E_{\min}}{E_{\max} - E_{\min}}, \quad (5.27)$$

where  $E_{\min}$ ,  $E_{\max}$  are the extremal eigenenergies in the spectrum of  $H$ . The relative energy  $\epsilon$  is bounded between 0 and 1, such that  $\epsilon = 0$  corresponds to finding an exact ground state. Note that, throughout this section, we place restrictions on the total “time” taken by the protocol,

$$T(\boldsymbol{\theta}) = \sum_{j=1}^p \sum_{k=1}^M \theta_{j,k}. \quad (5.28)$$

In Fig. 5.8 we first look at the probability distribution function for  $\log \epsilon$  for the points

in  $S$ . We generate a sample of  $10^4$  initial  $\theta$  angles, drawn from a uniform distribution in the  $[0, \pi)$  interval. The distribution of  $\log \epsilon$  gives us insight about the structure of the landscape. A sharply-defined distribution of  $\log \epsilon$  is only obtained in the case where  $h_x = h_z = 0.1$ , with the peak at  $\epsilon$  close to 0. The mean of the distribution shifts to large values of  $\epsilon$  upon approaching the critical line, e.g., at  $h_x = h_z = 1$ . In addition to the shift of the mean, the distribution also develops multiple peaks corresponding to local minima. At other points in the phase diagram, such as  $h_x = h_z = 2$ , the separate minima form a smooth curve with larger variance. Finally, in some cases like  $h_x = 2, h_z = 0.1$ , we observe a clear bimodal distribution of the minima. Thus, the distribution of minima varies considerably across the phase diagram and, generally, has multiple peaks.

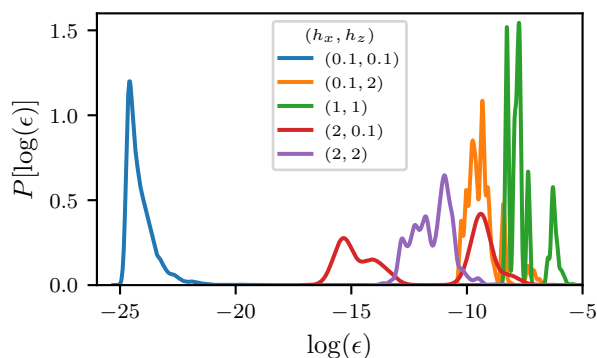


Figure 5.8: Probability distribution function  $P(\log(\epsilon))$  of QAOA outcomes on 10000 uniformly generated initial angles having as target the ground state of the points in  $S$ . Data is for system size  $L = 8$  and  $p = 4$ , with the protocol in Eqs. (5.7)-(5.5).

A systematic investigation of the nature of the landscape of a related minimisation problem was performed in Refs. [26, 44, 104] using a discretised adiabatic state preparation protocol. In these works, the behaviour of the minimisation landscape was examined as a function of the total allowed time for the protocol. It was found [26, 44] that there are distinct “phases” associated with different intervals for the total allowed time. Particularly, at intermediate times, there is a glassy phase presenting with multiple clusters of minima where the minimisation becomes difficult. Following Refs. [26, 44], we have probed the nature of the minimisation landscape in our models and using our protocol and model in Section 5.1.1 when the total time (5.28) is restricted. We impose this restriction in two different ways. First, we allow  $T(\theta)$  to be

less than or equal to some maximum total time  $T_{\leq \max}$ , which can be easily achieved by constraining the allowed interval for each  $\theta_{j,k}$  angle in our protocol. The second method is to demand  $T(\boldsymbol{\theta})$  to be exactly equal to a given total time  $T_{=\max}$ . The results of these two approaches are contrasted in Fig. 5.9(a) and (b).

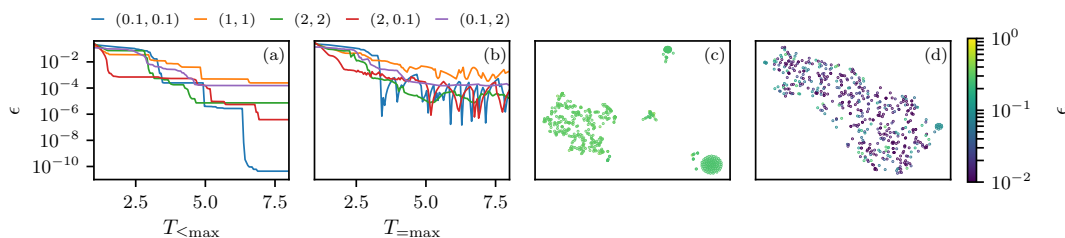


Figure 5.9: Characterisation of the minimisation landscape of the AFM Ising model. Legend indicates the Hamiltonian featuring in the cost function  $\epsilon(\boldsymbol{\theta})$ , and corresponds values of  $(h_x, h_z)$  taken to be representative of different regions in the phase diagram. (a)-(b) Minimum relative energy  $\epsilon$  found after running the `basinhopping` optimisation plotted against  $T_{\leq \max}$  (resp.  $T_{=\max}$ ), where we restrict the optimisation to circuits for which the total amount of time to run (5.28) is less than  $T_{\leq \max}$  (resp. to be equal to  $T_{=\max}$ ). (c)-(d) t-SNE plot identifying relative positions of minima for 500 random initialisations taken at  $(h_x, h_z) = (1, 1)$  and  $T_{=\max} = 1$  (resp.  $T_{=\max} = 8$ ), where the optimisation is performed using the L-BFGS algorithm. All data is for system size  $L = 6$  and  $p = 3$ . Color scale in (c), (d) represents the value of  $\epsilon$  at the minimum.

In Fig. 5.9(a) we see that, as expected, as  $T_{\leq \max}$  increases,  $\epsilon$  decreases. Perhaps surprisingly, this occurs in a very clear step-wise fashion, suggesting that there are discrete values of  $T_{\leq \max}$  that show significant improvement in state preparation. By contrast, in Fig. 5.9(b) we see that as  $T_{=\max}$  increases, the behaviour of  $\epsilon$  is more erratic, indicating that there are discrete, optimum values of  $T$  for which states can be prepared under this restriction. This shows that the protocol can not accommodate non-optimal values  $T_{=\max}$ , that is, there is no way for the protocol to continuously “stall” and wait, “wasting time” so as to emulate the last optimal value of  $T_{=\max}$ . The protocol can, however, “stall” in discrete values of  $\pi$ , due to the symmetry in the angles. A consequence of this seems to be the peaks and troughs in the graphs in Fig. 5.9(b), which show an irregular pattern. This contrasts with the results in Ref. [26, 44], which display an almost monotonically increasing success in state preparation as  $T_{=\max}$  increases.

Next, we took 500 random angle samples restricted to either  $T_{=\max}$  or  $T_{\leq \max}$  and

ran the variational algorithm with target state coming from the ground state at each of the representative points in  $S$ . Here, we have used the L-BFGS local optimisation algorithm, as implemented in the `scipy` Python package, to perform the minimisation. In order to plot the high-dimensional minimisation landscape, we have used t-SNE [196], a dimensionality-reduction algorithm for data visualization that embeds high dimensional data in a space with lower dimension while preserving the relative position of the data points. Performing t-SNE on these samples, we find that, for  $T_{\leq \max}, T_{=\max} < 1$ , there exists clustering of minima, although some of the clusters are significantly less compact than others – see Fig. 5.9(c). For  $T_{\leq \max}, T_{=\max} > 1$ , the clustering rapidly disappears, first for the  $T_{\leq \max}$  restriction and then for the  $T_{=\max}$  restriction – an example of the latter is shown in Fig. 5.9(d) for  $T_{=\max} = 8$ . This indicates that the variational algorithm, which usually does not place restrictions on the values of  $\theta$  angles and therefore implicitly operates in the large- $T$  regime, does not display a glassy phase in its minimisation landscape as found for a different protocol in Refs. [26, 44].

## 5.4 Conclusions

In this chapter, we have investigated the preparation of ground states of non-integrable quantum models using a variational algorithm. Our motivation was to identify physical properties of the state that have an impact on its preparation, thereby allowing us to bound their relative success. While this task appears challenging for rigorous analytical treatment, we have numerically demonstrated a correlation between interaction distance and the success of the variational protocols in several variants of the quantum Ising model. This suggests that, in these models, states which are far from free, as measured by interaction distance, are harder to prepare, i.e., in order to prepare states with larger interaction distance, the variational algorithm needs higher values of  $p$  to achieve the same degree of success as for states with lower interaction distance and lower  $p$ . We have also performed an analysis of the landscape associated with the QAOA optimisation problem. We have found that there are several local minima associated with this landscape, though they are spread out and show no distinctive clustering. Limiting the total allowed time did not alter this landscape significantly for total times  $T \gtrsim 1$ .

One of the applications of our results is that theoretical insight into the closest fermionic Gaussian state representing the target state can be gained by using the ex-

perimentally obtained ansatz and setting the small  $\theta_{k,1}$  angles to be zero. The absence of the glassy phase in the minimisation landscape implies that the protocols constructed here do not lead to a NP-hard optimisation problem and the time to find optimal angles should scale polynomially with the system size.

---

# CHAPTER 6

---

Towards an experimental quantification of  
fermionic interactions

In the previous chapter, we have quantified the hardness of preparation of a quantum state in terms of how far that state is from a free-fermionic one. We did so by comparing the success of the variational quantum algorithm with the interaction distance of the target state, which measures how far a quantum state is from being free-fermionic based on its entanglement spectrum.

In this chapter, we employ the interaction distance to study a well-known model in quantum condensed matter, the XYZ model, which we introduce in Section 6.1. Our contributions correspond to the sections not marked as “Background” (or subsections of those sections), and can be summarised as follows: Using DMRG techniques to obtain its ground state for system sizes on the order of hundreds of lattice sites, we study an emerging freedom in the XYZ model as the lattice size tends to the thermodynamic limit in Section 6.3. By considering Wick’s theorem as a defining property of free-fermionic states, in Section 6.4 we leverage it to obtain an equivalent way of quantifying how far from being free-fermionic a state is; we then use this to devise a method to experimentally measure fermionic interactions. We finish by analysing the robustness of this method in Section 6.5, before concluding in Section 6.6.

### 6.1 Background: The XYZ Model

The 1D spin-1/2 XYZ model with open boundary conditions and on a lattice of size  $L$  is given by

$$H = J_x \sum_{j=1}^{L-1} X_j X_{j+1} + J_y \sum_{j=1}^{L-1} Y_j Y_{j+1} + J_z \sum_{j=1}^{L-1} Z_j Z_{j+1}, \quad (6.1)$$

where  $X_i, Y_i, Z_i$  are the usual Pauli matrices on site  $i$ . This model hosts certain paradigmatic models as special cases, such as the Heisenberg model ( $J_x = J_y = J_z \neq 0$ ) or the XXZ model ( $J_x = J_y = 1$ ), both natural lattice models of magnetism solvable by the Bethe ansatz [17, 184], the XY-model ( $J_z = 0$ ), which is mappable to a system of spinless fermions hopping on a lattice [105] and can help elucidate the low-energy properties of the unconstrained model [131], or the classical nearest-neighbour Ising model ( $J_y = J_z = 0$ ), a celebrated model of ferromagnetism in statistical mechanics [84]. By employing the Jordan-Wigner transformation (see Section 2.3), the XYZ model

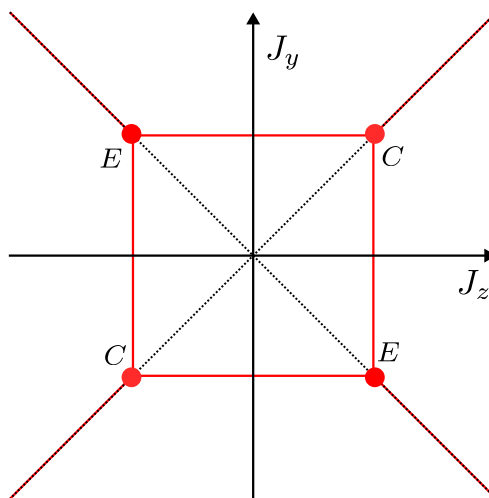


Figure 6.1: Phase diagram of the XYZ model (6.1). Red lines denote gapless regions, and the conformal ( $C$ ) and non-conformal ( $E$ ) tricritical points are indicated.

can be mapped to interacting spinless fermions

$$H = \sum_{j=1}^{L-1} J_+ a_j a_{j+1}^\dagger + J_- a_j a_{j+1} + \text{h.c.} + J_z (4n_j n_{j+1} - 2n_j - 2n_{j+1} + I), \quad (6.2)$$

where  $J_\pm = (J_x \pm J_y)$  and  $n_j = a_j^\dagger a_j$ . In this fermionic representation,  $J_z$  becomes the interaction coupling between fermion populations at neighbouring sites [105]. The other parameters of the model are associated to “non-interacting”, free-fermionic terms in this representation, as defined in Section 2.4.

In what follows, without loss of generality, we take  $J_x = 1$ . The phase diagram of the XYZ model is depicted in Figure 6.1, where gapless regions are represented in red. There are six distinct rotated instances of the XXZ model embedded along the lines  $J_y = \pm 1$ ,  $J_z = \pm 1$ ,  $J_y = \pm J_z$ . The intersection between these lines form two pairs of *tricritical points*; there are two points at  $(1, 1)$  and  $(-1, -1)$ , each corresponding to three XXZ models at their Berezinskii-Kosterlitz-Thouless transition, and two points at  $(1, -1)$  and  $(-1, 1)$ , each corresponding to three XXZ ferromagnets at their first order phase transition. In what follows, due to the symmetries  $(J_y, J_z) \leftrightarrow (-J_z, -J_y)$ ,  $(J_y, J_z) \leftrightarrow (J_z, J_y)$  of the Hamiltonian (6.1), we restrict ourselves to  $J_y \geq 0$  [55].

In 1970, Sutherland observed that the transfer matrix of the 2D zero-field eight-vertex model commutes with the Hamiltonian of the XYZ model [183]. This was

independently studied by Baxter, who famously used this result to derive a number of analytical results on this model [13–15]. The connection between the XYZ model and the 2D zero-field eight vertex model was expressed by Baxter [13] as

$$\Gamma = J_y/J_x, \Delta = J_z/J_x, \quad (6.3)$$

where  $\Gamma, \Delta$ , are parameters of the zero-field eight-vertex model. This is valid in the so-called principal regime, i.e.  $|J_y| < J_x < -J_z$ ; the remainder of the phase diagram can be covered by utilising the symmetries of the model, which were covered in Section 6.1. The parameters  $\Gamma, \Delta$  are in turn expressed in terms of elliptic functions using two other parameters,  $k$  and  $\lambda$ , as

$$\Gamma_r = (1 + k \operatorname{sn}^2 i\lambda)/(1 - k \operatorname{sn}^2 i\lambda), \quad (6.4)$$

$$\Delta_r = -\operatorname{cn} i\lambda \operatorname{dn} i\lambda/(1 - k \operatorname{sn}^2 i\lambda), \quad (6.5)$$

where  $\operatorname{sn}, \operatorname{cn}, \operatorname{dn}$  are the Jacobian elliptic functions. The natural domains of these parameters are

$$0 \leq k \leq 1, \quad (6.6)$$

$$0 \leq \lambda \leq I(k'), \quad (6.7)$$

where  $I$  denotes the complete elliptic integral of the first kind, and

$$k' = \sqrt{1 - k^2}. \quad (6.8)$$

The correlation length of a translationally invariant spin model is conventionally defined as the exponent  $\xi$  such that for some  $\tau$ ,

$$\langle Z_j Z_{j+k} \rangle \sim k^{-\tau} \exp\left\{-\frac{k}{\xi}\right\}. \quad (6.9)$$

Johnson and Baxter obtained [15, 89] the analytical formula for  $\xi$  in the ordered regime of the XYZ model in the thermodynamic limit, expressing it in terms of the

---

## 6.2 Background: Matrix Product States and the DMRG algorithm

---

parameterisation (6.4) as

$$\xi^{-1} = \begin{cases} -\ln k_1 & (\mu \leq \pi/2), \\ -\ln \frac{k_1}{\operatorname{dn}^2 \left[ \frac{J(k_1)J(k')}{2J(k)} - J(k'), k'_1 \right]} & (\pi/2 < \mu), \end{cases} \quad (6.10)$$

where  $k_1 = 2\sqrt{x} \prod_{m=1}^{\infty} \left( \frac{1+x^{4m}}{1+x^{4m-2}} \right)$  and  $x = e^{-\pi\lambda/2J(k)}$ .

## 6.2 Background: Matrix Product States and the DMRG algorithm

The density matrix renormalisation group (DMRG) was first established in 1992 by Steve White [205, 206], and has since become a cornerstone in the study of one dimensional quantum many-body systems [169]. In many relevant applications, it is able to efficiently compute the ground state for lattice sizes on the order of hundreds – a breakthrough in the classical simulations of quantum models, for which the exponential scaling of the vector space is one of the main limiting factors. In this section, we review the DMRG procedure following [169]. Here, we will adopt the matrix product state (MPS) formalism, which was independently developed [2, 12, 56] and later connected to the DMRG algorithm [49, 142, 185, 207]. Matrix product states turned out to be a natural language for expressing and extending the DMRG, and enabled several advancements in the area, such as the time-evolution of quantum states [200] and infinite-size simulations [199].

We begin by describing how an MPS approximation of a quantum state  $|\psi\rangle$  can be obtained. This representation expresses each amplitude of this state as a product of matrices by successively applying a singular value decomposition followed by a truncation of the resulting singular values. The process proceeds as follows: first, note that this state can be written as  $|\psi\rangle = \sum_{\sigma_1, \dots, \sigma_L} c_{\sigma_1, \dots, \sigma_L} |\sigma_1 \dots \sigma_L\rangle$ , where the  $\sigma_l$  are indices for the local single-particle bases at each site, and  $c_{\sigma_1 \dots \sigma_L}$  is a tensor representing the amplitudes of this quantum state. By regrouping the indices<sup>1</sup> and performing an SVD

---

<sup>1</sup>This regrouping consists in indexing the basis for the tensor product space using a single index, as opposed to using separate indices for each single-particle space.

## 6.2 Background: Matrix Product States and the DMRG algorithm

---

(as introduced in 2.5) on the matrix  $c_{a_1,(\sigma_2\dots\sigma_L)}$ , we obtain the representation

$$|\psi\rangle = \sum_{\sigma_1,\dots,\sigma_L} A_{a_1}^{\sigma_1} c_{a_1,\sigma_2,\dots,\sigma_L} |\sigma_1\dots\sigma_L\rangle. \quad (6.11)$$

By repeating this process for each lattice site, we obtain

$$|\psi\rangle = \sum_{\sigma_1,\dots,\sigma_L,a_1,\dots,a_L} A_{a_1}^{\sigma_1} A_{a_1,a_2}^{\sigma_2} \dots A_{a_L}^{\sigma_L} |\sigma_1\dots\sigma_L\rangle. \quad (6.12)$$

A graphical representation of this iterative process is given in Figure 6.2. At each step  $l$ , the singular value decomposition yields

$$U_{(a_{l-1}\sigma_l),a_l} S_{a_l} V_{a_l,(\sigma_{l+1},\dots,\sigma_L)}^T = A_{a_{l-1},a_l}^{\sigma_l} c_{a_l,\sigma_{l+1},\dots,\sigma_L}, \quad (6.13)$$

where  $S_l$  is absorbed into the remaining tensor  $c_{a_l,\sigma_{l+1},\dots,\sigma_L}$ . The state is approximated by truncating the singular values  $S_{a_l}$  under a certain threshold at each step – the number of singular values retained is called the *bond dimension* and is usually denoted by the symbol  $\chi$ . The condition for an MPS to efficiently approximate a state is that this truncation is such that the number of remaining singular values scales efficiently with the size of the system. This is related to the entanglement entropy across the bipartition of the lattice over which the SVD is being computed; indeed, the operation performed at each step is analogous to a Schmidt decomposition, and the squared singular values yield the entanglement spectrum, from which the entanglement entropy is computed. (as explained in Section 2.5). Although this correspondence is not mathematically rigorous (it is possible to construct states with e.g., low entanglement entropy but for which the MPS construction is not efficient), it is for relevant physical models a good indication of whether a state is amenable to being approximated by an MPS [171]. In one dimension, this indicates that gapped systems (for which the entanglement entropy scales as a constant with lattice size) and critical systems, which admit a logarithmic correction to the entanglement entropy, can be successfully studied using matrix product states.

Note that, in the process just described, one could likewise have started from the

## 6.2 Background: Matrix Product States and the DMRG algorithm

---

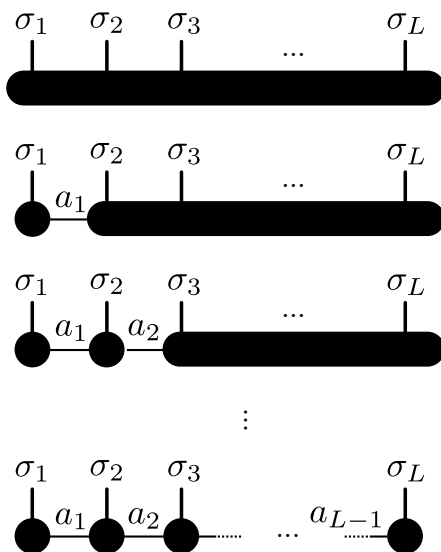


Figure 6.2: The process of approximating a quantum state with amplitudes encoded by the tensor  $c_{\sigma_1, \sigma_2, \dots, \sigma_L}$  by a product of matrices  $A_{a_1}^{\sigma_1} A_{a_1, a_2}^{\sigma_2} \dots A_{a_L}^{\sigma_L}$  as in (6.12). A singular value decomposition is successively applied to a matrix obtained by regrouping the indices of the amplitude tensor. This introduces a new index  $a_l$  at each step, corresponding to the multiplication of the matrices in the decomposition. This index is truncated so that the smallest singular values are discarded, yielding an efficient approximate representation for quantum states where the number of relevant singular values scales efficiently with the size of the system. This is the case for e.g. the ground states of gapped systems and certain systems at criticality admitting a logarithmic correction to the entanglement entropy.

right end of the lattice to obtain

$$|\psi\rangle = \sum_{\sigma_1, \dots, \sigma_L, a_1, \dots, a_L} B_{a_1}^{\sigma_1} B_{a_1, a_2}^{\sigma_2} \dots B_{a_L}^{\sigma_L} |\sigma_1 \dots \sigma_L\rangle, \quad (6.14)$$

where

$$U_{(a_{l-1}\sigma_l), a_l} S_{a_l} V_{a_l, (\sigma_{l+1}, \dots, \sigma_L)}^T = c_{\sigma_1, \dots, \sigma_{l-1} a_{l-1}} B_{a_{l-1}, a_l}^{\sigma_l}, \quad (6.15)$$

and  $S_l$  is again absorbed into the remaining tensor  $c_{\sigma_1, \dots, \sigma_{l-1} a_{l-1}}$ . One could even have mixed both (6.12) and (6.14) by starting from each end of the lattice and meeting at

## 6.2 Background: Matrix Product States and the DMRG algorithm

---

some lattice site  $l$  to obtain

$$|\psi\rangle = \sum_{\sigma_1, \dots, \sigma_L, a_1, \dots, a_L} A_{a_1}^{\sigma_1} \dots A_{a_{l-1}, a_l}^{\sigma_l} S_{a_l} B_{a_l, a_{l+1}}^{\sigma_{l+1}} \dots B_{a_L}^{\sigma_L} |\sigma_1 \dots \sigma_L\rangle. \quad (6.16)$$

The form (6.12) is said to be *left canonical*, while the one in (6.14) is said to be *right canonical* and the one in (6.16) is said to be *mixed canonical*. The key property differentiating the matrices  $A, B$  is that  $\sum_{\sigma_l} A^{\sigma_l \dagger} A^{\sigma_l} = I$ , while  $\sum_{\sigma_l} B^{\sigma_l} B^{\sigma_l \dagger} = I$ ; the matrices  $A^{\sigma_l}$  are said to be *left-normalised*, while the matrices  $B^{\sigma_l}$  are said to be *right-normalised*. In practice, this can be exploited to simplify the index contractions in the DMRG algorithm implementation.

Before moving on to the DMRG algorithm, we must establish how an operator can be represented in a format analogous to (6.12). Note that an operator  $H$  can be written as

$$H = \sum_{\sigma_1, \dots, \sigma_L, \sigma'_1, \dots, \sigma'_L} c_{\sigma_1, \dots, \sigma_L, \sigma'_1, \dots, \sigma'_L} |\sigma_1, \dots, \sigma_L\rangle \langle \sigma'_1, \dots, \sigma'_L|. \quad (6.17)$$

By pairing indices referring to the same site and following the procedure outlined for matrix product states, we obtain a *matrix product operator*

$$H = \sum_{\sigma_1, \dots, \sigma_L, \sigma'_1, \dots, \sigma'_L} W^{\sigma_1 \sigma'_1} \dots W^{\sigma_L \sigma'_L} |\sigma_1, \dots, \sigma_L\rangle \langle \sigma'_1, \dots, \sigma'_L|. \quad (6.18)$$

In practice, when  $H$  is local, this structure can be exploited to efficiently construct an MPO representation [81, 169]. The inner product between states represented by matrix product states  $|\psi\rangle$  as in (6.12) and  $|\phi\rangle = \sum_{\sigma_1, \dots, \sigma_L} \tilde{A}^{\sigma_1} \dots \tilde{A}^{\sigma_L} |\sigma_1 \dots \sigma_L\rangle$  can be expressed as

$$\langle \psi | \phi \rangle = \sum_{\sigma_1, \dots, \sigma_L} (A^{\sigma_1} \dots A^{\sigma_L}) (\tilde{A}^{\sigma_1} \dots \tilde{A}^{\sigma_L})^\dagger, \quad (6.19)$$

and the expectation value of  $\psi$  with respect to  $H$  can be computed as

$$\langle \psi | H | \psi \rangle = \sum_{\sigma_1, \dots, \sigma_L, \sigma'_1, \dots, \sigma'_L} (A^{\sigma_1} A^{\sigma_2} \dots A^{\sigma_L}) (W^{\sigma_1 \sigma'_1} \dots W^{\sigma_L \sigma'_L}) (A^{\sigma'_1} A^{\sigma'_2} \dots A^{\sigma'_L})^\dagger. \quad (6.20)$$

Note, however, that the naive evaluation of these expressions is unfeasible. Not only

## 6.2 Background: Matrix Product States and the DMRG algorithm

---

the order of index contraction greatly influences the speed with which the computation is performed, and must be taken into account, but also there are intermediate computations that can be iteratively constructed; in what follows, we will address how the latter consideration plays into the DMRG algorithm. While the expressions involved can be unwieldy, here we are mainly concerned with conveying the principal ideas behind an efficient implementation of the DMRG algorithm; for a more complete treatment, we refer the reader to [169].

The expectation value of a state  $|\psi\rangle$  in mixed-canonical form at a site  $l$  as in (6.16) with respect to an operator  $H$  represented by an MPO as in (6.18) can be evaluated as

$$\langle\psi|H|\psi\rangle = \sum_{\sigma_l, \sigma'_l} \sum_{a'_{l-1}, a'_l} \sum_{a_{l-1}, a_l} \sum_{b_{l-1}, b_l} L_{b_{l-1}}^{a_{l-1}, a'_{l-1}} W_{b_{l-1}, b_l}^{\sigma_l, \sigma'_l} R_{b_l}^{a_l, a'_l} M_{a_{l-1}, a_l}^{\sigma_l \dagger} M_{a'_{l-1}, a'_l}^{\sigma'_l}. \quad (6.21)$$

where  $A, B$  represent the subsystems on either side of site  $l$ ,  $M_{a'_{l-1}, a'_l}^{\sigma'_l}$  represents the centre site matrices in this mixed-canonical representation, and  $L, R$  are defined as

$$L_{b_{l-1}}^{a_{l-1}, a'_{l-1}} = \sum_{a_i, b_i, a'_i; i < l-1} \left( \sum_{\sigma_1, \sigma'_1} A_{1, a_1}^{\sigma_1 \dagger} W_{1, b_1}^{\sigma_1, \sigma'_1} A_{1, a'_1}^{\sigma'_1} \right) \dots \quad (6.22)$$

$$\left( \sum_{\sigma_{l-1}, \sigma'_{l-1}} A_{a_{l-2}, a_{l-1}}^{\sigma_{l-1} \dagger} W_{b_{l-2}, b_{l-1}}^{\sigma_{l-1}, \sigma'_{l-1}} A_{a'_{l-2}, a'_{l-1}}^{\sigma'_{l-1}} \right), \quad (6.23)$$

$$R_{b_l}^{a_l, a'_l} = \sum_{a_i, b_i, a'_i; i > l} \left( \sum_{\sigma_{l+1}, \sigma'_{l+1}} B_{a_l, a_{l+1}}^{\sigma_{l+1} \dagger} W_{b_l, b_{l+1}}^{\sigma_{l+1}, \sigma'_{l+1}} B_{a'_l, a'_{l+1}}^{\sigma'_{l+1}} \right) \dots \quad (6.24)$$

$$\left( \sum_{\sigma_L, \sigma'_L} B_{a_{L-1}, 1}^{\sigma_L \dagger} W_{b_{L-1}, 1}^{\sigma_L, \sigma'_L} B_{a'_{L-1}, 1}^{\sigma'_L} \right). \quad (6.25)$$

The main reason behind writing (6.21) in terms of the matrices  $L$  and  $R$  is that these are iteratively built during the DMRG algorithm, as we will observe in what follows.

In finding the ground state  $|\psi\rangle$  of a Hamiltonian, we seek to minimise the energy  $\frac{\langle\psi|H|\psi\rangle}{\langle\psi|\psi\rangle}$ . To this end, the DMRG algorithm aims to find the extrema of the function

$$\langle\psi|H|\psi\rangle - \lambda\langle\psi|\psi\rangle, \quad (6.26)$$

where  $\lambda$  is a Langrange multiplier. This is done by iteratively fixing all matrices in the

### 6.3 Interaction distance and emergent freedom in the XYZ model

---

decomposition, except those for a single site  $\sigma_l$ , and solving an eigenvalue problem so as to minimise (6.26). The process consists of several "sweeps" across the lattice, and runs as follows:

1. Choose an MPS in right canonical form (6.14) to serve as the initial guess for the algorithm. Iteratively compute the  $R$  matrices (6.25) in (6.21).
2. Sweep right by starting from site  $l = 1$  and successively improving the ground state approximation at the current site, left normalising the resulting matrix by performing an SVD so that the MPS is now in mixed-canonical one site to the right, and shifting to that site. Iteratively build the  $L$  matrices (6.23) in (6.21) during the sweep.
3. Sweep left, analogously to the previous step: starting at the last site, improve the ground state approximation, right normalise the resulting matrix by performing an SVD and shift one site to the left. Iteratively compute the  $R$  matrices (6.25) in (6.21) during the sweep.
4. Repeat until convergence is achieved or a specified number of sweeps is performed.

### 6.3 Interaction distance and emergent freedom in the XYZ model

In this section, we use interaction distance to characterise the entanglement spectrum of the ground state of the XYZ model as the size of the system tends to infinity. This spectrum was derived in the thermodynamic limit in [53] using a connection [15] between this model and the so-called *corner transfer matrices* (CTMs) of the 2D zero-field eight vertex model<sup>1</sup>, which we briefly touched upon in Section 2.5. In this limit, in the basis where the corner transfer matrices are mutually diagonal, the density matrix takes the form

$$\rho = \begin{pmatrix} 1 & 0 \\ 0 & x \end{pmatrix} \otimes \begin{pmatrix} 1 & 0 \\ 0 & x^2 \end{pmatrix} \otimes \begin{pmatrix} 1 & 0 \\ 0 & x^3 \end{pmatrix} \dots \quad (6.27)$$

---

<sup>1</sup>This connection between quantum models and a 2D classical counterpart [136, 137, 186] had previously been used by Peschel, Kaulke and Legeza to derive the structure of the reduced density matrix of the ground state of the transverse field Ising model and of the XXZ model [158]

### 6.3 Interaction distance and emergent freedom in the XYZ model

---

where  $x = \exp(-\pi\lambda/I(k))$ , with  $\lambda, k$  being defined in (6.4), (6.5). The spectrum of this matrix can be seen to follow the structure (2.48) with single-particle modes  $\epsilon_j = x^j$ ; thus the ground state of this model is free-fermionic in the thermodynamic limit.

While the entanglement spectrum is known in this limit, it is of interest to examine it at finite sizes, and to study how it converges as the lattice grows to an infinite number of sites. This is relevant to simulations in near-term quantum computers, for which the number of qubits is at most on the order of hundreds [164]. In the remainder of this section, we conduct this study by computing the interaction distance across the phase diagram of the model as the system size increases. We do so by employing the density matrix renormalisation group (DMRG) algorithm [169, 205], as implemented in the iTensor [62] library, to obtain the entanglement spectrum of the ground state of the model at each point in the diagram. As explained in Section 6.2, this is an algorithm that can efficiently compute the ground state of a local 1D quantum Hamiltonian on the order of hundreds of lattice sites.

There are technical issues arising from the use of DMRG that we must consider. The model (6.1) possesses a quasi-degeneracy that is exponentially vanishing with system size; that is, as the system size approaches infinity, the gap between the ground state of the model and its first excited state decreases exponentially, resulting in degenerate ground states in this limit. Consequently, when we employ DMRG to find the ground state of the model for large system sizes, a superposition between the ground state and the first excited state will generally be returned. Since here we concern ourselves with quantities computed from the entanglement spectrum of the state, and this spectrum is greatly affected by the presence of a superposition, this degeneracy must be lifted so that accurate results can be obtained.

This issue was solved by simply picking an appropriate, physically motivated, initial state for the algorithm. We found that when this is done, the algorithm naturally resolves the quasi-degeneracy. Concretely, the initial state is picked in the basis associated to the largest coefficient in the Hamiltonian, and depends on the sign of this coefficient. If this sign is negative, a Néel state  $|\uparrow\downarrow \dots \uparrow\downarrow\rangle$  in the appropriate basis is picked, corresponding to an antiferromagnetic ordering in the direction of the largest coupling; if it is positive, a fully polarised state  $|\uparrow\uparrow \dots \uparrow\rangle$  in the appropriate basis is picked, corresponding to a ferromagnetic ordering in the direction of the largest coupling. For instance if  $|J_y| > |J_x|$ ,  $|J_y| > |J_z|$  and  $J_y < 0$ , then a  $Y$ -polarized Néel initial

### 6.3 Interaction distance and emergent freedom in the XYZ model

state is picked.

The interaction distance for the XYZ model (6.1) is shown in Fig. 6.3 for 200 spins. Along the line  $J_y = J_z$ , which is equivalent to the XXZ model with antiferromagnetic couplings studied in Ref. [150],  $D_{\mathcal{F}}$  is large around the gapless critical phase  $|J_y| > 1$ . On the line  $J_y = -J_z$ ,  $D_{\mathcal{F}}$  is large across a much narrower region around its  $|J_y| > 1$  gapless phase. Away from the critical regions,  $D_{\mathcal{F}}$  tends to zero, showing that the entanglement spectrum starts to quickly converge to that of a free-fermionic state. We will focus our investigation around the gapless regions, where  $D_{\mathcal{F}}$  exhibits non-trivial behaviour.

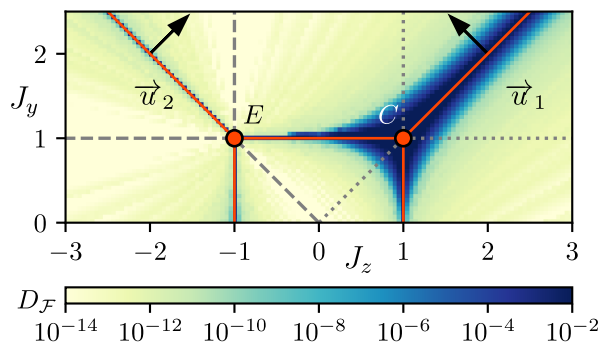


Figure 6.3: Interaction distance,  $D_{\mathcal{F}}$ , in Eq. (2.45), obtained using DMRG across the phase diagram of the XYZ model for  $L=200$  spins. Red lines denote critical lines, and the conformal ( $C$ ) and non-conformal ( $E$ ) tricritical points are indicated [54]. Vectors  $\vec{u}_1, \vec{u}_2$  are orthogonal to the critical lines and are used in Fig. 6.4. Interaction distance is strongly suppressed in gapped phases of the XYZ model, signalling the emergence of Gaussianity. The DMRG bond dimension was allowed to scale as necessary.

While the ground state of the XYZ model presents with free-fermionic entanglement when  $L \rightarrow \infty$ , we expect that the model becomes free when  $L$  exceeds the correlation length  $\xi$  by a certain amount. As argued in [192] and reviewed in Section 2.6, this is because the system then hosts quasiparticles spanning this number of lattice sites, and the correlations between these quasiparticles, which have a free-fermionic nature, then dominate the entanglement spectrum. When applied to the XYZ model, the interaction distance can diagnose the emergence of freedom and thus quantify the point at which the entanglement spectrum becomes free-fermionic for various system sizes  $L$  compared to  $\xi$ . Without loss of generality, we consider the behaviour of  $D_{\mathcal{F}}$  along the  $\vec{u}_1$  vector, which crosses the  $J_y = J_z$  critical region, and the  $\vec{u}_2$  vector, which crosses the  $J_y = -J_z$

## 6.4 Violation of Wick's theorem as an experimental proxy for interaction distance

---

critical region, as shown in Fig. 6.4(a). We find that, for values of the couplings away from the critical lines,  $D_{\mathcal{F}}$  tends to zero exponentially fast as system size increases, signalling the emerging freedom.

To analyse the conditions under which this happens, we determine the system size  $L_{\min}$  beyond which the interaction distance starts decreasing, as well as the rate  $r$  at which  $D_{\mathcal{F}} \propto \exp(-rL)$  approaches zero. Fig. 6.4(b) shows that  $r$  decreases as the correlation length  $\xi$  increases, i.e. the rate of exponential decay of  $D_{\mathcal{F}}$  decreases the closer we are to the critical regions. Hence,  $D_{\mathcal{F}}$  can quantify the point at which the results in the thermodynamic limit become valid, and shows that the quantum correlations of the XYZ model become free-fermion-like by having  $D_{\mathcal{F}} \rightarrow 0$  exponentially fast with  $L$ , provided that the size is larger than a minimum value  $L_{\min}$ . The latter is a polynomial function of the correlation length  $\xi$ , as can be seen in Fig. 6.4(c). We observe that the larger the correlation length, i.e., the closer to criticality, the larger the system needs to be in order for the interaction distance to exhibit the exponential decay. We emphasise that this strong dependence of  $D_{\mathcal{F}}$  on  $L$  allows one to efficiently identify the emergent Gaussianity in a simulation of the XYZ model with an exponential accuracy with a linear cost in the size of the simulated system.

## 6.4 Violation of Wick's theorem as an experimental proxy for interaction distance

Investigating the behaviour of the XYZ model in terms of the interaction distance reveals the emergence of Gaussianity in a quantitative way. Ideally, however, we would like to have an experimentally accessible quantity that enables one to detect this emergent freedom in the laboratory, as in general the full entanglement spectrum of the system can be difficult to extract in an experimental context [40, 97, 160]. To this effect, we first start by studying how a violation in Wick's theorem, which is satisfied by all fermionic Gaussian states, can be quantified and related to the interaction distance. This approach will eventually lead us to an identification of the emergent freedom of a many-body quantum system using simple, physical observables.

Wick's theorem provides the means to calculate higher-point correlators of a Gaussian state in terms of its two-point correlators (see Section 2.4). For a four-point

## 6.4 Violation of Wick's theorem as an experimental proxy for interaction distance

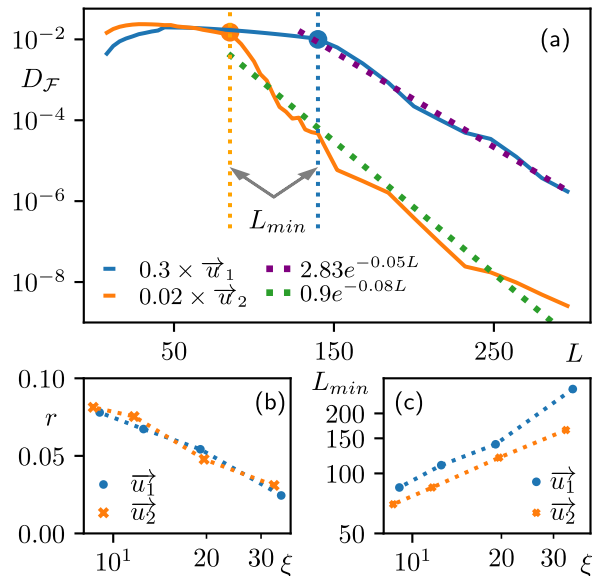


Figure 6.4: (a) Exponential decay of  $D_{\mathcal{F}}$  with system size at different points along  $\vec{u}_1$  and  $\vec{u}_2$  cuts through the phase diagram in Fig. 6.3. We observe a short initial increase, followed by a plateau and the final decrease beyond some crossover length scale,  $L_{\min}$ , indicated by the dotted lines. Dashed lines are fits to the asymptotic exponential decay,  $D_{\mathcal{F}} \propto \exp(-rL)$ , for data points  $L > L_{\min}$ . (b) Slope  $k$  of the exponential decay, extracted at various points along  $\vec{u}_1$  and  $\vec{u}_2$ , exhibits a power-law dependence on correlation length  $\xi$ . The latter is computed using the analytic formulas (6.10) applicable in the thermodynamic limit. (c) Correlation length  $\xi$  displays power-law dependence on  $L_{\min}$ . The DMRG bond dimension was set to 512 for computations included in this figure

operator  $a_i^\dagger a_i a_j^\dagger a_j$ , it states that

$$\langle a_j^\dagger a_j a_k^\dagger a_k \rangle_\rho = \langle a_j^\dagger a_j \rangle_\rho \langle a_k^\dagger a_k \rangle_\rho, \quad (6.28)$$

where  $\langle \mathcal{O} \rangle_\rho := \text{tr}(\rho \mathcal{O})$  and  $\rho$  is a FGS. For a general quantum state, this is no longer necessarily true. To quantify the degree of violation of (6.28), we will consider

$$\mathcal{W}(\rho) = |\langle d_j^\dagger d_j d_k^\dagger d_k \rangle_\rho - \langle d_j^\dagger d_j \rangle_\rho \langle d_k^\dagger d_k \rangle_\rho|, \quad (6.29)$$

where the operators  $d_i$  used in the computation of  $\mathcal{W}$  are the eigenoperators associated

## 6.4 Violation of Wick's theorem as an experimental proxy for interaction distance

---

to the entanglement Hamiltonian of  $\rho$ , which, as explained in Section 2.5, can for a general quantum state be written in the following form:

$$H_E^{\text{int}} = \sum_j \epsilon_j d_j^\dagger d_j + \sum_{j,k} \epsilon_{jk} d_j^\dagger d_j d_k^\dagger d_k + \dots, \quad (6.30)$$

where  $\epsilon_i$  are the single particle energies and  $\epsilon_{ij}$  are the two particle energies of the entanglement Hamiltonian, and so forth. If this state is Gaussian with respect to the bipartition chosen, then all energies other than the single particle ones vanish.

Like the interaction distance, this quantity can be used to identify the effect of fermionic interactions. In fact, we can show that whenever a model is identified as free by the interaction distance, this is necessarily also the case for  $\mathcal{W}(\rho)$ , as  $\mathcal{W}(\rho) \leq 6D_{\mathcal{F}}(\rho)$ . To prove this bound, let first  $\sigma$  be a fermionic Gaussian state. Then,  $\mathcal{W}(\sigma) = 0$ , and we can write

$$\begin{aligned} \mathcal{W}(\rho) &= |\langle d_j^\dagger d_j d_k^\dagger d_k \rangle_\rho - \langle d_j^\dagger d_j d_k^\dagger d_k \rangle_\sigma - \langle d_j^\dagger d_j \rangle_\rho \langle d_k^\dagger d_k \rangle_\rho + \langle d_j^\dagger d_j \rangle_\sigma \langle d_k^\dagger d_k \rangle_\sigma| \leq \\ &|\text{tr}(d_j^\dagger d_j d_k^\dagger d_k (\rho - \sigma))| + |\langle d_j^\dagger d_j \rangle_\rho| |\text{tr}(d_k^\dagger d_k (\rho - \sigma))| + |\text{tr}(d_j^\dagger d_j (\rho - \sigma))| |\langle d_k^\dagger d_k \rangle_\sigma|. \end{aligned} \quad (6.31)$$

We know that (see Section 2.6)

$$\text{tr}(\mathcal{O}(\rho - \sigma)) \leq 2\|\mathcal{O}\|D_{\mathcal{F}}(\rho), \quad (6.32)$$

where  $\|\mathcal{O}\|$  can be taken to be the largest eigenvalue of the operator  $\mathcal{O}$  [151]. Then, from (6.31), we obtain

$$\mathcal{W}(\rho) \leq 6D_{\mathcal{F}}(\rho). \quad (6.33)$$

The two-point correlator with respect to

$$\rho = \exp(-H_E^{\text{int}}) \quad (6.34)$$

can be computed as [157]

$$\langle d_j^\dagger d_j \rangle_\rho = \frac{1}{e^{\epsilon_j} + 1}, \quad (6.35)$$

and the four point correlators as

$$\langle d_j^\dagger d_j d_k^\dagger d_k \rangle_\rho = \frac{1}{e^{\epsilon_{jk}}} + e^{\epsilon_{jk} - \epsilon_j} + e^{\epsilon_{jk} - \epsilon_k} + 1. \quad (6.36)$$

## 6.4 Violation of Wick's theorem as an experimental proxy for interaction distance

---

By leveraging these expressions, we can calculate the violation (6.29) of Wick's theorem exclusively in terms of the entanglement energies  $\epsilon_j$ ,  $\epsilon_k$  and  $\epsilon_{jk}$ . As in interaction distance, we do this to avoid computing an explicit representation of the eigenoperators  $d_j$  (see Section 2.4). In what follows, we obtain these energies heuristically by assuming that the two smallest levels (excluding the one corresponding to the normalisation) are  $\epsilon_j$  and  $\epsilon_k$ . We then assume that the level closest to their sum corresponds to  $\epsilon_{jk}$ . Despite the heuristic nature of this approach, it yields very good results, as can be seen in the relationship between  $\mathcal{W}$  and  $D_{\mathcal{F}}$  throughout the phase diagram of the XYZ model (6.1) plotted in Figure 6.5(a). Not only the inequality (6.33) we have derived is satisfied, but there is a clear polynomial relationship between the two quantities, which indicates that they capture the same information. This suggests that the optimisation involved in the computation of interaction distance may in certain cases be replaced by the heuristic approach we have taken in determining the single-particle modes. Furthermore, it reflects that  $D_{\mathcal{F}}$  is principally determined by the largest elements of the entanglement spectrum. As explained in Section 2.5, the eigenoperators  $d_j$ ,  $d_j^\dagger$  are, in general, related to the operators  $a_j$ ,  $a_j^\dagger$  defined on the underlying lattice model (6.2) through a non-local transformation. At this stage, therefore, we are presented with the same issue as with interaction distance: in order to determine (6.29) experimentally, one needs full state tomography.

To measure the emerging freedom of the system in terms of physical observables, we directly compute the violation of Wick's theorem relative to the local operators  $a_j$ ,  $a_j^\dagger$ . We later analyse the generality of this approach. We find that the best results are obtained when the  $a_j$ ,  $a_j^\dagger$  are constructed for a Jordan-Wigner quantisation axis matching the coefficient in the model which is largest in absolute value, as shown in Fig. 6.5(c). For instance, where  $|J_z| \geq |J_y|, |J_x|$  we define the violation of the local Wick's theorem as

$$\mathcal{W}_l(\rho) = |\langle Z_j Z_{j+1} \rangle_\rho - \langle Z_j \rangle_\rho \langle Z_{j+1} \rangle_\rho - \langle Y_j X_{j+1} \rangle_\rho \langle X_j Y_{j+1} \rangle_\rho + \langle X_j X_{j+1} \rangle_\rho \langle Y_j Y_{j+1} \rangle_\rho|, \quad (6.37)$$

which is written in terms of two-spin correlators that are experimentally accessible. In general, this axis of quantisation could be optimised depending on the underlying quantum state and physical model being studied, and could possibly even continuously vary along the phase diagram. This would bring the choice of fermionic operators closer

## 6.4 Violation of Wick's theorem as an experimental proxy for interaction distance

---

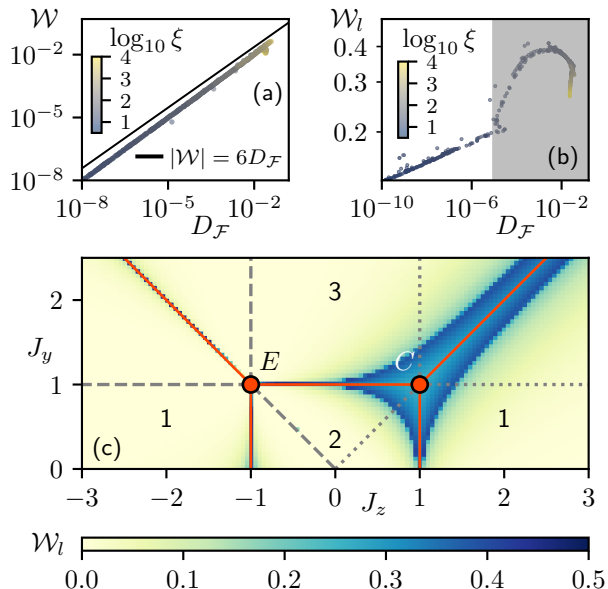


Figure 6.5: (a)-(b) Scatter plots comparing  $|\mathcal{W}|$  in Eq. (6.29) and  $|\mathcal{W}_l|$  in Eq. (6.37) with  $D_{\mathcal{F}}$ , for sizes  $L = 600$  and  $L = 400$ , respectively. We see that  $|\mathcal{W}|$  essentially coincides with  $D_{\mathcal{F}}$ , while  $|\mathcal{W}_l|$  strongly correlates with  $D_{\mathcal{F}}$  below the threshold  $D_{\mathcal{F}}^* \approx 10^{-9}$ . The shaded area,  $D_{\mathcal{F}} > D_{\mathcal{F}}^*$ , corresponds to data points near critical regions with high correlation lengths, where the relationship between  $D_{\mathcal{F}}$  and  $\mathcal{W}_l$  breaks down. (c)  $|\mathcal{W}_l|$  across the phase diagram of the XYZ model in Eq. (6.1) for size  $L = 400$ . When computing  $|\mathcal{W}_l|$ , we use a different Jordan-Wigner axis of quantisation for each region, labelled as follows: in 1 we pick the  $z$  quantisation axis, in 2 we pick the  $x$ -axis, and in 3 the  $y$ -axis. The DMRG bond dimension was allowed to scale as necessary in (a), and was set to 128 in (b) and (c).

to the  $d_i$  eigenbasis, which result from generic unitary transformations of the underlying lattice modes on each side of the bipartition.

While  $\mathcal{W}_l$  does not necessarily satisfy the inequality (6.33), we have numerically determined that it is tightly related to  $D_{\mathcal{F}}$  with a monotonic one-to-one correspondence in the gapped region of the XYZ model, as shown in Fig. 6.5(b). Discrepancies from this behaviour only emerge near the critical regions, due to the finite-size effects. Thus,  $\mathcal{W}_l$  can successfully identify the emerging freedom of the XYZ model. In Fig. 6.5(c), we evaluated  $\mathcal{W}_l$  throughout the phase diagram of the XYZ model, finding similar behaviour to  $D_{\mathcal{F}}$  in Fig. 6.3(b).  $\mathcal{W}_l$  becomes identical to  $\mathcal{W}$  when the model is in

the gapped antiferromagnetic phase of the XXZ-model, when  $J_y^2 + J_z^2 \rightarrow \infty$ , or when  $J_y^2 + J_z^2 \rightarrow 0$ . In this case the violation of the local Wick's theorem  $\mathcal{W}_l$  provides the same information as  $D_{\mathcal{F}}$ , while it can be measured in the laboratory.

## 6.5 Robustness of experimental probe under realistic conditions

To demonstrate the experimental relevance of our results, we analyse the applicability of  $\mathcal{W}_l$  in the presence of realistic conditions, such as variations in the range of interactions, coupling inhomogeneities and local random potentials. For example, in a cold atom implementation, the interactions between the constituent particles are characterised by a long-range algebraic decay [29, 117]. Moreover, there might be inhomogeneities in the engineered couplings due to imperfections in the laser control procedures or spurious random local potentials.

We first consider the effect that a polynomial profile of interactions has on the behaviour of  $\mathcal{W}_l$ . We introduce a long-range XYZ model

$$H^{\text{LR}} = \sum_{j,k} \frac{1}{|j-k|^\alpha} (J_x X_j X_{j+k} + J_y Y_j Y_{j+k} + J_z Z_j Z_{j+k}), \quad (6.38)$$

where  $\alpha$  controls the power-law decay of the couplings. The ground-state properties of this model can be captured using finite DMRG by expressing the algebraically decaying interaction as a sum of exponentials; this allows us to represent the Hamiltonian as a matrix-product operator [140, 162]. In Fig. 6.6(a) we show the behaviour of  $\mathcal{W}_l$  as a function of system size in the long-range model. We picked a representative point which is in the gapped, antiferromagnetic phase for the entire range of  $\alpha$  values considered [110]. As in the short-range model,  $\mathcal{W}_l$  decreases rapidly after the system exceeds a certain size  $L_{\text{min}}$ . Note that, in contrast to the short-range case,  $\mathcal{W}_l$  now levels off at a very small but non-zero value as  $L \rightarrow \infty$ , indicating that the entanglement of the ground state does not become completely free in the thermodynamic limit. The saturation value depends on the couplings and  $\alpha$ .

A second type of robustness check we performed is the effect of experimental noise on  $\mathcal{W}_l$ . To model this, we firstly introduce randomised couplings on each site. In Fig. 6.6(b) the couplings along the  $\vec{u}_2$  cut are sampled uniformly from  $[J_j - \delta J^{\text{max}}, J_j + \delta J^{\text{max}}]$

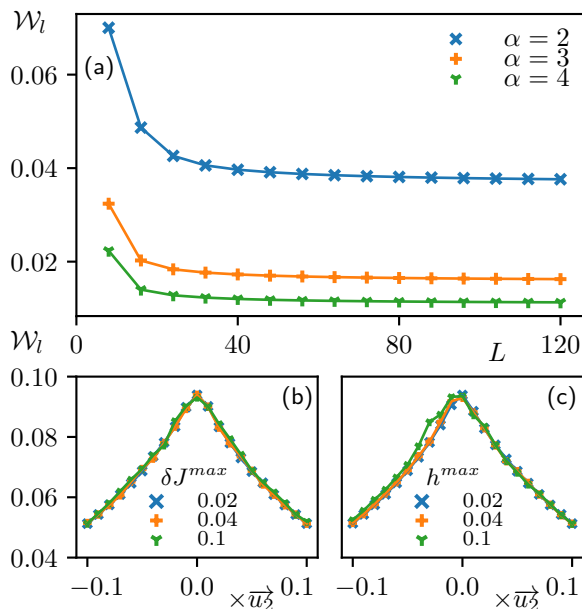


Figure 6.6: (a)  $W_l$  as a function of system size for the long-range XYZ model in Eq. (6.38) with fixed  $J_x = 1.0$ ,  $J_y = -1.0$  and  $J_z = 5.0$  and various  $\alpha$ . (b)  $W_l$  across the  $\vec{u}_2^z$  cut with different amounts of per-site randomness  $\delta J^{\max}$  applied to the couplings  $J_x$ ,  $J_y$  and  $J_z$  at system size  $L = 100$ . (c)  $W_l$  across the  $\vec{u}_2^z$  cut with a random local field of strength  $h^{\max}$  applied to every site of an  $L = 100$  system. The DMRG code was run with bond dimension  $\chi = 128$ .

on each site with  $W_l$  remaining stable and increasing only a small amount up to large variations in the couplings. We additionally consider the impact of a spurious local magnetic field in the  $z$ -direction. In Fig. 6.6(c) a random local field sampled uniformly from  $[-h^{\max}, h^{\max}]$  was added on each site of the chain along the  $\vec{u}_2^z$  cut.  $W_l$  also shows stability under this class of perturbations. Hence, the emerging freedom of the XYZ model persists in the presence of experimental imperfections that break its integrability, while the behaviour of its ground-state correlations, as witnessed by  $D_{\mathcal{F}}$  and  $W_l$ , remains largely the same.

## 6.6 Conclusions

There is a stark contrast between genuinely interacting systems and free ones in terms of the complexity of their description, as well as their physical properties, such as

their thermalisation behaviour and out-of-equilibrium dynamics. The entanglement spectrum of the ground state of the XYZ model, which encompasses a large family of physically relevant models, has a free-fermionic structure in the thermodynamic limit, even though it incorporates fermionic interactions in its definition. Here, we identified the system size conditions for the freedom to emerge near and away from the critical regions of the model as a function of the correlation length of the system.

We proposed a way to observe the emergence of Gaussianity in the correlations of the XYZ model in terms of observables that can be directly measured in the laboratory. Moreover, we quantified the emergent Gaussian behaviour in the XYZ model for the experimentally relevant cases of finite system sizes, long-range interaction potentials, as well as inhomogeneous couplings and random local potentials. As Gaussianity emerges exponentially fast with system size, we anticipate that our results can be experimentally verified in several experimental realisations of XYZ-type models, both in solid state materials as well as synthetic ultracold atom systems [70, 87, 130, 152, 161, 168, 187].

As our method does not rely on the integrability techniques, which are mainly restricted to one spatial dimension, it could be applied to other non-integrable 1D systems or even 2D models, provided a suitable lattice bipartition can be identified. An open question is, of course, how the transformation of  $\mathcal{W}$  to  $\mathcal{W}_l$  should be performed in general. A rigorous method to express  $\mathcal{W}$  in terms of experimentally measurable operators would involve considering the explicit transformation of the eigenoperators  $d_j$  to the fermionic operators  $a_j$  defined in terms on the lattice degrees of freedom. This will in general be unfeasible in practice – a direct decomposition would result in an exponential number of terms, most of which are non-local. This would make a finite-size study quite difficult, while analytical results in the thermodynamic limit may be ultimately irrelevant (where e.g. the ground state is already known to be free-fermionic in this limit).

Thus, though a formal study and general characterisation of the eigenoperators  $d_j$  would be of great interest, case-by-case heuristic approximations backed up by numerical and physical arguments may be the best goal for experimental applications. On this note, aspects worth exploring are the nature of the fermion-qubit mapping used – in this work, the standard Jordan-Wigner transformation was employed, which results in highly non-local operators due to the presence of a string of  $Z$  operators. Mappings such as the Bravyi-Kitaev [174] or Verstraete-Cirac [198] transformations could allow

for a more elaborate approximate decomposition while maintaining the locality of the resulting operators.

---

# CHAPTER 7

---

Conclusions

---

In this work, we have explored how variational algorithms can be used to prepare the ground state of a number of many-body models in quantum condensed matter. We have, in particular, probed how the interplay between the physical properties of the models and the associated optimisation procedure can affect the success of the algorithm. To this end, we made use of several techniques, such as the interaction distance, which aims to measure the distance between an interacting fermionic state and a corresponding optimal fermionic Gaussian state. We reviewed this measure in Section 2.6, and later independently studied it in Chapter 6, where we computed it in context of the XYZ model of magnetism and explored the possibility of measuring Gaussianity through simple physical observables.

After a review of spin and fermionic systems in Chapter 2, our analysis started in Chapter 3, where we expanded upon the Lie theoretical framework for variational algorithms. There, we have pointed out that the states that the algorithm can prepare form the set of all ground states of the Hamiltonians in the Lie algebra of the variational protocol. Moreover, we identified a Lie subalgebra which generates a Gauge subgroup of the unitaries in the protocol. This Gauge subgroup leaves the initial state invariant, justifying that one does not need the entire set of unitaries to prepare every possible state, and that certain directions in the parameter space will leave the state under preparation unchanged. By computing the Lie algebra of the Quantum Approximate Optimisation Algorithm defined on a 1-dimensional lattice, we analytically showed that a state can be prepared by this protocol if and only if that state is free-fermionic. This was exploited in Chapter 4 to conduct a comprehensive numerical study. By carefully modifying the variational protocol, we extend it to non-integrable models in Chapter 5.

We proceeded to perform this extensive numerical characterisation of the 1D QAOA in Chapter 4. There, we exploited the efficient classical simulation of free-fermionic systems, both to counteract the overhead imposed by the necessity of performing a nonlinear optimisation, and to reach large system sizes not ordinarily attainable in exact classical simulations. In our exploration, we found that the physical properties of the target Hamiltonian greatly affect the optimisation of the algorithm. In particular, we observed that using a protocol with fewer symmetries makes the preparation of non-local Hamiltonians *easier*, and of local Hamiltonians *harder*, while the opposite happens when symmetries are enforced. We argued that constraining the space of states that the optimiser can explore causes non-local Hamiltonians to drive it into regions that

---

trap it in local minima. This evidences how the mutual influence between the physical features of the model and the parameter optimisation needs to be taken into account when employing these algorithms. It also highlights that in certain cases, the use of symmetries may be detrimental to the optimisation. This is particularly interesting, since symmetries are generally believed to benefit the algorithm by reducing its search space.

In contrast with the case above, there exist conditions where the influence of the physical features predominantly dominates the parameter optimisation – and vice versa. On the one hand, in our study of overparameterisation in Section 4.3, we see that by increasing the circuit depth beyond a certain threshold, the optimisation converges to the target state exponentially in the number of iterations regardless of the target Hamiltonian chosen. Interestingly, we see that the number of iterations that the algorithm takes to converge to the solution also decreases with this depth, indicating that the effects of overparameterisation are quickly established beyond this threshold. On the other hand, in our study of non-integrable models in Chapter 5, the success of state preparation was dominated by how far from being free-fermionic the model is, as measured using the entanglement spectrum of the model through the interaction distance. Moreover, we observe that the connection between the success of the optimisation and the interaction distance can provide information about which phase the model is in. This reinforces the idea that the success of the optimisation is mainly determined by a physical property of the model in this case. Thus, in the case of the overparameterised circuit, factors directly related to the algorithm determine its success, while in the interaction distance case, it is a property of the model that predominantly influences how effective the algorithm ultimately is.

By taking a quantum many-body perspective, our work furthers the understanding of variational algorithms and their applications. Its conclusions, however, are not restricted to condensed matter systems, as many problems must ultimately be mapped to such a system to be optimised variationally e.g. combinatorial optimisation problems which are translated to the problem of finding the ground state of an Ising-type Hamiltonian [108].

An interesting future direction would be to rigorously prove some of the results involving free-fermionic systems in Chapter 4. While these systems are known to be amenable to an analytical treatment (see e.g. [47]), the associated variational optim-

---

isation tends to make this challenging [203]. A problem that may be within reach is that of determining the minimum circuit depth for maximum expressibility. A family of circuits that can provably parameterise fermionic Gaussian states is relevant, as there are no known examples (to the best of the author’s knowledge) of a practical parameterisation of that manifold of states. Such a parameterisation can improve upon approaches to optimisation where the state is a priori unconstrained and is explicitly projected back to a fermionic Gaussian state at every step, resulting in a truncation error [211]. In addition, the possibility to overparameterise the circuit, potentially making the optimisation in such studies trivial, is a significant advantage in this approach. An application of this would be to variationally approximate quantum states by fermionic Gaussian states, which would also yield a measure of fermionic Gaussianity. This measure would depend on the cost function chosen – if e.g. this is the overlap with the target state, we would obtain a distance to the set of fermionic Gaussian states defined in terms of a given set of fermionic modes. However, if we chose a distance to the entanglement spectrum of the target state (with respect to some bipartition) as the cost, this measure would then be equivalent to the interaction distance, which we reviewed in Section 2.6 and studied in Chapter 6 in the context of the XYZ model.

Another compelling line of research would be to systematically explore the differences between various protocols having the same Lie algebra. Indeed, a Lie algebra can admit several sets of generators – and from the results in Section 3.2, the corresponding algorithms will all ultimately produce the same set of states. A comparison between protocols constructed in such a way would be relevant in determining differences between variational algorithms with the same expressibility. Indeed, given some target state, we expect it to be the case that a protocol is more suitable to its preparation than others; more generally, the minimum circuit depth for maximum expressibility may be smaller for certain sets of generators. Moreover, it would be interesting to explore how the Gauge degree of freedom that we have pointed out affects the Hamiltonian in the cost function. Indeed, an entire family of Hamiltonians still in the Lie algebra having a specified target state as its ground state can be obtained by conjugation by elements of the Gauge group. One could hope that it is the case that some of these Hamiltonians will work better as a cost function (through faster convergence or fewer local minima). Finally, this Lie algebraic approach could provide a suitable set of Hamiltonians for adaptively constructed circuits [68, 217] to generate quantum gates from – as long as

---

this set contains elements of the Lie algebra which include at least one set of generators, the algorithm's expressibility is determined.

# BIBLIOGRAPHY

- [1] Amira Abbas, David Sutter, Christa Zoufal, Aurelien Lucchi, Alessio Figalli, and Stefan Woerner. The power of quantum neural networks. *Nature Computational Science*, 1(6):403–409, 2021. ISSN 2662-8457. doi:[10.1038/s43588-021-00084-1](https://doi.org/10.1038/s43588-021-00084-1).
- [2] Ian Affleck, Tom Kennedy, Elliott H. Lieb, and Hal Tasaki. Rigorous results on valence-bond ground states in antiferromagnets. *Physical Review Letters*, 59(7):799–802, 1987. doi:[10.1103/physrevlett.59.799](https://doi.org/10.1103/physrevlett.59.799).
- [3] F. Albertini and D. D’Alessandro. Notions of controllability for quantum mechanical systems, 2001. doi:[10.48550/ARXIV.QUANT-PH/0106128](https://doi.org/10.48550/ARXIV.QUANT-PH/0106128).
- [4] Abhinav Anand, Philipp Schleich, Sumner Alperin-Lea, Phillip W. K. Jensen, Sukin Sim, Manuel Díaz-Tinoco, Jakob S. Kottmann, Matthias Degroote, Artur F. Izmaylov, and Alán Aspuru-Guzik. A quantum computing view on unitary coupled cluster theory. *Chemical Society Reviews*, 51(5):1659–1684, 2022. doi:[10.1039/d1cs00932j](https://doi.org/10.1039/d1cs00932j).
- [5] Eric R. Anschuetz and Bobak T. Kiani. Quantum variational algorithms are swamped with traps. *Nature Communications*, 13(1), 2022. doi:[10.1038/s41467-022-35364-5](https://doi.org/10.1038/s41467-022-35364-5).
- [6] Daniel P. Arovas and Assa Auerbach. Extended heisenberg models of antiferromagnetism: Analogies to the fractional quantum hall effect. *Physical Review Letters*, 60(6):531–534, 1988. doi:[10.1103/physrevlett.60.531](https://doi.org/10.1103/physrevlett.60.531).
- [7] Andrew Arrasmith, Zoë Holmes, M Cerezo, and Patrick J Coles. Equivalence of quantum barren plateaus to cost concentration and narrow gorges. *Quantum Science and Technology*, 7(4):045015, 2022. doi:[10.1088/2058-9565/ac7d06](https://doi.org/10.1088/2058-9565/ac7d06).

- [8] Nikita Astrakhantsev, Sheng-Hsuan Lin, Frank Pollmann, and Adam Smith. Time evolution of uniform sequential circuits, 2022. doi:[10.48550/ARXIV.2210.03751](https://doi.org/10.48550/ARXIV.2210.03751).
- [9] V. Bapst, L. Foini, F. Krzakala, G. Semerjian, and F. Zamponi. The quantum adiabatic algorithm applied to random optimization problems: The quantum spin glass perspective. *Physics Reports*, 523(3):127–205, 2013. doi:[10.1016/j.physrep.2012.10.002](https://doi.org/10.1016/j.physrep.2012.10.002).
- [10] J. Bardeen, L. N. Cooper, and J. R. Schrieffer. Microscopic theory of superconductivity. *Physical Review*, 106(1):162–164, 1957. doi:[10.1103/physrev.106.162](https://doi.org/10.1103/physrev.106.162).
- [11] George S. Barron, Bryan T. Gard, Orien J. Altman, Nicholas J. Mayhall, Edwin Barnes, and Sophia E. Economou. Preserving symmetries for variational quantum eigensolvers in the presence of noise. *Phys. Rev. Applied*, 16:034003, 2021. doi:[10.1103/PhysRevApplied.16.034003](https://doi.org/10.1103/PhysRevApplied.16.034003).
- [12] R. J. Baxter. Dimers on a rectangular lattice. *Journal of Mathematical Physics*, 9(4):650–654, 1968. doi:[10.1063/1.1664623](https://doi.org/10.1063/1.1664623).
- [13] R. J. Baxter. One-dimensional anisotropic Heisenberg chain. *Phys. Rev. Lett.*, 26:834–834, 1971. doi:[10.1103/PhysRevLett.26.834](https://doi.org/10.1103/PhysRevLett.26.834).
- [14] Rodney Baxter. Eight-vertex model in lattice statistics and one-dimensional anisotropic heisenberg chain. III. eigenvectors of the transfer matrix and hamiltonian. *Annals of Physics*, 76(1):48–71, 1973. doi:[10.1016/0003-4916\(73\)90441-7](https://doi.org/10.1016/0003-4916(73)90441-7).
- [15] Rodney J. Baxter. *Exactly Solved Models in Statistical Mechanics*. Academic Press London, 1985. doi:[10.1142/9789814415255\\_0002](https://doi.org/10.1142/9789814415255_0002).
- [16] Marcello Benedetti, Erika Lloyd, Stefan Sack, and Mattia Fiorentini. Parameterized quantum circuits as machine learning models. *Quantum Science and Technology*, 4(4):043001, 2019. doi:[10.1088/2058-9565/ab4eb5](https://doi.org/10.1088/2058-9565/ab4eb5).
- [17] H. Bethe. Zur theorie der metalle. *Zeitschrift für Physik*, 71(3-4):205–226, 1931. doi:[10.1007/bf01341708](https://doi.org/10.1007/bf01341708).
- [18] Jacob Biamonte. Universal variational quantum computation. *Phys. Rev. A*, 103:L030401, 2021. doi:[10.1103/PhysRevA.103.L030401](https://doi.org/10.1103/PhysRevA.103.L030401).

- [19] Jacob Biamonte, Peter Wittek, Nicola Pancotti, Patrick Rebentrost, Nathan Wiebe, and Seth Lloyd. Quantum machine learning. *Nature*, 549(7671):195–202, 2017. doi:[10.1038/nature23474](https://doi.org/10.1038/nature23474).
- [20] Claude Bloch and Albert Messiah. The canonical form of an antisymmetric tensor and its application to the theory of superconductivity. *Nuclear Physics*, 39:95–106, 1962. doi:[10.1016/0029-5582\(62\)90377-2](https://doi.org/10.1016/0029-5582(62)90377-2).
- [21] Nick S. Blunt, Joan Camps, Ophelia Crawford, Róbert Izsák, Sebastian Leontica, Arjun Mirani, Alexandra E. Moylett, Sam A. Scivier, Christoph Sünderhauf, Patrick Schopf, Jacob M. Taylor, and Nicole Holzmann. Perspective on the current state-of-the-art of quantum computing for drug discovery applications. *Journal of Chemical Theory and Computation*, 18(12):7001–7023, 2022. doi:[10.1021/acs.jctc.2c00574](https://doi.org/10.1021/acs.jctc.2c00574).
- [22] N. N. Bogoljubov. On a new method in the theory of superconductivity. *Il Nuovo Cimento*, 7(6):794–805, 1958. doi:[10.1007/bf02745585](https://doi.org/10.1007/bf02745585).
- [23] Lucas T. Brady, Christopher L. Baldwin, Aniruddha Bapat, Yaroslav Kharkov, and Alexey V. Gorshkov. Optimal protocols in quantum annealing and quantum approximate optimization algorithm problems. *Physical Review Letters*, 126(7), 2021. doi:[10.1103/physrevlett.126.070505](https://doi.org/10.1103/physrevlett.126.070505).
- [24] Sergey Bravyi and David Gosset. Complexity of quantum impurity problems. *Communications in Mathematical Physics*, 356(2):451–500, 2017. doi:[10.1007/s00220-017-2976-9](https://doi.org/10.1007/s00220-017-2976-9).
- [25] Hans J. Briegel and Robert Raussendorf. Persistent entanglement in arrays of interacting particles. *Phys. Rev. Lett.*, 86:910–913, 2001. doi:[10.1103/PhysRevLett.86.910](https://doi.org/10.1103/PhysRevLett.86.910).
- [26] Marin Bukov, Alexandre G. R. Day, Phillip Weinberg, Anatoli Polkovnikov, Pankaj Mehta, and Dries Sels. Broken symmetry in a two-qubit quantum control landscape. *Phys. Rev. A*, 97(5):052114, 2018. doi:[10.1103/PhysRevA.97.052114](https://doi.org/10.1103/PhysRevA.97.052114).
- [27] Pasquale Calabrese and John Cardy. Entanglement entropy and quantum field theory. *Journal of Statistical Mechanics: Theory and Experiment*, 2004(06):P06002, 2004. doi:[10.1088/1742-5468/2004/06/p06002](https://doi.org/10.1088/1742-5468/2004/06/p06002).

- [28] Yudong Cao, Jonathan Romero, Jonathan P. Olson, Matthias Degroote, Peter D. Johnson, Mária Kieferová, Ian D. Kivlichan, Tim Menke, Borja Peropadre, Nicolas P. D. Sawaya, Sukin Sim, Libor Veis, and Alán Aspuru-Guzik. Quantum chemistry in the age of quantum computing. *Chemical Reviews*, 119(19):10856–10915, 2019. doi:[10.1021/acs.chemrev.8b00803](https://doi.org/10.1021/acs.chemrev.8b00803).
- [29] Lincoln D Carr, David DeMille, Roman V Krems, and Jun Ye. Cold and ultracold molecules: science, technology and applications. *New Journal of Physics*, 11(5):055049, 2009. doi:[10.1088/1367-2630/11/5/055049](https://doi.org/10.1088/1367-2630/11/5/055049).
- [30] M. Cerezo, Andrew Arrasmith, Ryan Babbush, Simon C. Benjamin, Suguru Endo, Keisuke Fujii, Jarrod R. McClean, Kosuke Mitarai, Xiao Yuan, Lukasz Cincio, and Patrick J. Coles. Variational quantum algorithms. *Nature Reviews Physics*, 3(9):625–644, 2021. ISSN 2522-5820. doi:[10.1038/s42254-021-00348-9](https://doi.org/10.1038/s42254-021-00348-9).
- [31] M. Cerezo, Akira Sone, Tyler Volkoff, Lukasz Cincio, and Patrick J. Coles. Cost function dependent barren plateaus in shallow parametrized quantum circuits. *Nature Communications*, 12(1):1791, 2021. ISSN 2041-1723. doi:[10.1038/s41467-021-21728-w](https://doi.org/10.1038/s41467-021-21728-w).
- [32] Alba Cervera-Lierta. Exact Ising model simulation on a quantum computer. *Quantum*, 2:114, 2018. ISSN 2521-327X. doi:[10.22331/q-2018-12-21-114](https://doi.org/10.22331/q-2018-12-21-114).
- [33] Xie Chen, Zheng-Cheng Gu, and Xiao-Gang Wen. Complete classification of one-dimensional gapped quantum phases in interacting spin systems. *Phys. Rev. B*, 84:235128, 2011. doi:[10.1103/PhysRevB.84.235128](https://doi.org/10.1103/PhysRevB.84.235128).
- [34] Siew-Ann Cheong and Christopher L. Henley. Many-body density matrices for free fermions. *Physical Review B*, 69(7), 2004. doi:[10.1103/physrevb.69.075111](https://doi.org/10.1103/physrevb.69.075111).
- [35] Ming-Chiang Chung and Ingo Peschel. Density-matrix spectra of solvable fermionic systems. *Physical Review B*, 64(6), 2001. doi:[10.1103/physrevb.64.064412](https://doi.org/10.1103/physrevb.64.064412).
- [36] R. Coldea, D. A. Tennant, E. M. Wheeler, E. Wawrzynska, D. Prabhakaran, M. Telling, K. Habicht, P. Smeibidl, and K. Kiefer. Quantum Criticality in an Ising Chain: Experimental Evidence for Emergent E8 Symmetry. *Science*, 327(5962):177–180, 2010. ISSN 0036-8075. doi:[10.1126/science.1180085](https://doi.org/10.1126/science.1180085).

- [37] Iris Cong, Soonwon Choi, and Mikhail D. Lukin. Quantum convolutional neural networks. *Nature Physics*, 15(12):1273–1278, 2019. ISSN 1745-2481. doi:[10.1038/s41567-019-0648-8](https://doi.org/10.1038/s41567-019-0648-8).
- [38] Domenico D'Alessandro. *Introduction to Quantum Control and Dynamics*. Chapman and Hall/CRC, 2007. doi:[10.1201/9781584888833](https://doi.org/10.1201/9781584888833).
- [39] Andrew J. Daley, Immanuel Bloch, Christian Kokail, Stuart Flannigan, Natalie Pearson, Matthias Troyer, and Peter Zoller. Practical quantum advantage in quantum simulation. *Nature*, 607(7920):667–676, 2022. doi:[10.1038/s41586-022-04940-6](https://doi.org/10.1038/s41586-022-04940-6).
- [40] M. Dalmonte, B. Vermersch, and P. Zoller. Quantum simulation and spectroscopy of entanglement hamiltonians. *Nature Physics*, 14(8):827–831, 2018. ISSN 1745-2481. doi:[10.1038/s41567-018-0151-7](https://doi.org/10.1038/s41567-018-0151-7).
- [41] Marcello Dalmonte, Viktor Eisler, Marco Falconi, and Benoît Vermersch. Entanglement hamiltonians: From field theory to lattice models and experiments. *Annalen der Physik*, 534(11):2200064, 2022. doi:[10.1002/andp.202200064](https://doi.org/10.1002/andp.202200064).
- [42] Christoph Dankert, Richard Cleve, Joseph Emerson, and Etera Livine. Exact and approximate unitary 2-designs and their application to fidelity estimation. *Physical Review A*, 80(1), 2009. doi:[10.1103/physreva.80.012304](https://doi.org/10.1103/physreva.80.012304).
- [43] BISWA NATH DATTA. CANONICAL FORMS OBTAINED VIA ORTHOGONAL TRANSFORMATIONS. In *Numerical Methods for Linear Control Systems*, pages 79–103. Elsevier, 2004. doi:[10.1016/b978-012203590-6/50008-2](https://doi.org/10.1016/b978-012203590-6/50008-2).
- [44] Alexandre G. R. Day, Marin Bukov, Phillip Weinberg, Pankaj Mehta, and Dries Sels. Glassy Phase of Optimal Quantum Control. *Phys. Rev. Lett.*, 122(2):020601, 2019. doi:[10.1103/PhysRevLett.122.020601](https://doi.org/10.1103/PhysRevLett.122.020601).
- [45] Rohit Dilip, Yu-Jie Liu, Adam Smith, and Frank Pollmann. Data compression for quantum machine learning. *Physical Review Research*, 4(4), 2022. doi:[10.1103/physrevresearch.4.043007](https://doi.org/10.1103/physrevresearch.4.043007).
- [46] Andrew C. Doherty and Stephen D. Bartlett. Identifying phases of quantum many-body systems that are universal for quantum computation. *Phys. Rev. Lett.*, 103:020506, 2009. doi:[10.1103/PhysRevLett.103.020506](https://doi.org/10.1103/PhysRevLett.103.020506).

- [47] Henrik Dreyer, Mircea Bejan, and Etienne Granet. Quantum computing critical exponents. *Phys. Rev. A*, 104:062614, 2021. doi:[10.1103/PhysRevA.104.062614](https://doi.org/10.1103/PhysRevA.104.062614).
- [48] Yuxuan Du, Zhuozhuo Tu, Xiao Yuan, and Dacheng Tao. Efficient measure for the expressivity of variational quantum algorithms. *Phys. Rev. Lett.*, 128:080506, 2022. doi:[10.1103/PhysRevLett.128.080506](https://doi.org/10.1103/PhysRevLett.128.080506).
- [49] J Dukelsky, M. A Martín-Delgado, T Nishino, and G Sierra. Equivalence of the variational matrix product method and the density matrix renormalization group applied to spin chains. *Europhysics Letters (EPL)*, 43(4):457–462, 1998. doi:[10.1209/epl/i1998-00381-x](https://doi.org/10.1209/epl/i1998-00381-x).
- [50] Amit Dutta, Gabriel Aeppli, Bikas K. Chakrabarti, Uma Divakaran, Thomas F. Rosenbaum, and Diptiman Sen. *Quantum Phase Transitions in Transverse Field Spin Models: From Statistical Physics to Quantum Information*. Cambridge University Press, 2015. doi:[10.1017/CBO9781107706057](https://doi.org/10.1017/CBO9781107706057).
- [51] Pablo Echenique and J. L. Alonso. A mathematical and computational review of hartree–fock SCF methods in quantum chemistry. *Molecular Physics*, 105(23-24): 3057–3098, 2007. doi:[10.1080/00268970701757875](https://doi.org/10.1080/00268970701757875).
- [52] Daniel J. Egger, Claudio Gambella, Jakub Marecek, Scott McFaddin, Martin Mevissen, Rudy Raymond, Andrea Simonetto, Stefan Woerner, and Elena Yndurain. Quantum computing for finance: State-of-the-art and future prospects. *IEEE Transactions on Quantum Engineering*, 1:1–24, 2020. doi:[10.1109/TQE.2020.3030314](https://doi.org/10.1109/TQE.2020.3030314).
- [53] Elisa Ercolessi, Stefano Evangelisti, and Francesco Ravanini. Exact entanglement entropy of the xyz model and its sine-Gordon limit. *Physics Letters A*, 374(21):2101–2105, 2010. ISSN 0375-9601. doi:<https://doi.org/10.1016/j.physleta.2010.03.014>.
- [54] Elisa Ercolessi, Stefano Evangelisti, Fabio Franchini, and Francesco Ravanini. Essential singularity in the Renyi entanglement entropy of the one-dimensional XYZ spin- $\frac{1}{2}$  chain. *Phys. Rev. B*, 83:012402, 2011. doi:[10.1103/PhysRevB.83.012402](https://doi.org/10.1103/PhysRevB.83.012402).
- [55] Stefano Evangelisti. Quantum correlations in field theory and integrable systems, 2013. doi:[10.48550/ARXIV.1302.5836](https://doi.org/10.48550/ARXIV.1302.5836).

- [56] M Fannes, B Nachtergaele, and R. F Werner. Exact antiferromagnetic ground states of quantum spin chains. *Europhysics Letters (EPL)*, 10(7):633–637, 1989. doi:[10.1209/0295-5075/10/7/005](https://doi.org/10.1209/0295-5075/10/7/005).
- [57] Edward Farhi, Jeffrey Goldstone, Sam Gutmann, and Michael Sipser. Quantum computation by adiabatic evolution, 2000. doi:[10.48550/ARXIV.QUANT-PH/0001106](https://doi.org/10.48550/ARXIV.QUANT-PH/0001106).
- [58] Edward Farhi, Jeffrey Goldstone, and Sam Gutmann. A quantum approximate optimization algorithm, 2014. doi:[10.48550/ARXIV.1411.4028](https://doi.org/10.48550/ARXIV.1411.4028).
- [59] R. P. Feynman. Atomic theory of liquid helium near absolute zero. *Physical Review*, 91(6):1301–1308, 1953. doi:[10.1103/physrev.91.1301](https://doi.org/10.1103/physrev.91.1301).
- [60] R. P. Feynman and Michael Cohen. Energy spectrum of the excitations in liquid helium. *Physical Review*, 102(5):1189–1204, 1956. doi:[10.1103/physrev.102.1189](https://doi.org/10.1103/physrev.102.1189).
- [61] Lukasz Fidkowski and Alexei Kitaev. Topological phases of fermions in one dimension. *Phys. Rev. B*, 83:075103, 2011. doi:[10.1103/PhysRevB.83.075103](https://doi.org/10.1103/PhysRevB.83.075103).
- [62] Matthew Fishman, Steven White, and Edwin Stoudenmire. The ITensor software library for tensor network calculations. *SciPost Physics Codebases*, 2022. doi:[10.21468/scipostphyscodeb.4](https://doi.org/10.21468/scipostphyscodeb.4).
- [63] P. Francesco, P. Mathieu, and D. Senechal. *Conformal Field Theory*. Graduate Texts in Contemporary Physics. Springer New York, 2012. ISBN 978-1-4612-2256-9.
- [64] Keisuke Fujii, Kaoru Mizuta, Hiroshi Ueda, Kosuke Mitarai, Wataru Mizukami, and Yuya O. Nakagawa. Deep variational quantum eigensolver: A divide-and-conquer method for solving a larger problem with smaller size quantum computers. *PRX Quantum*, 3(1), 2022. doi:[10.1103/prxquantum.3.010346](https://doi.org/10.1103/prxquantum.3.010346).
- [65] Bryan T. Gard, Linghua Zhu, George S. Barron, Nicholas J. Mayhall, Sophia E. Economou, and Edwin Barnes. Efficient symmetry-preserving state preparation circuits for the variational quantum eigensolver algorithm. *npj Quantum Information*, 6(1):10, 2020. ISSN 2056-6387. doi:[10.1038/s41534-019-0240-1](https://doi.org/10.1038/s41534-019-0240-1).

- [66] T. Giamarchi and Oxford University Press. *Quantum Physics in One Dimension*. International Series of Monographs on Physics, ISSN 0950-5563, Oxford Science Publications. Clarendon Press, 2004. ISBN 9780198525004.
- [67] S. M. Girvin, A. H. MacDonald, and P. M. Platzman. Collective-excitation gap in the fractional quantum hall effect. *Physical Review Letters*, 54(6):581–583, 1985. doi:[10.1103/physrevlett.54.581](https://doi.org/10.1103/physrevlett.54.581).
- [68] Harper R. Grimsley, Sophia E. Economou, Edwin Barnes, and Nicholas J. Mayhall. An adaptive variational algorithm for exact molecular simulations on a quantum computer. *Nature Communications*, 10(1):3007, 2019. ISSN 2041-1723. doi:[10.1038/s41467-019-10988-2](https://doi.org/10.1038/s41467-019-10988-2).
- [69] Harper R. Grimsley, George S. Barron, Edwin Barnes, Sophia E. Economou, and Nicholas J. Mayhall. Adaptive, problem-tailored variational quantum eigensolver mitigates rough parameter landscapes and barren plateaus. *npj Quantum Information*, 9(1), 2023. doi:[10.1038/s41534-023-00681-0](https://doi.org/10.1038/s41534-023-00681-0).
- [70] M. Gring, M. Kuhnert, T. Langen, T. Kitagawa, B. Rauer, M. Schreitl, I. Mazets, D. Adu Smith, E. Demler, and J. Schmiedmayer. Relaxation and prethermalization in an isolated quantum system. *Science*, 337(6100):1318–1322, 2012. ISSN 0036-8075. doi:[10.1126/science.1224953](https://doi.org/10.1126/science.1224953).
- [71] Stuart Hadfield, Zihui Wang, Bryan O’Gorman, Eleanor Rieffel, Davide Venturelli, and Rupak Biswas. From the Quantum Approximate Optimization Algorithm to a Quantum Alternating Operator Ansatz. *Algorithms*, 12(2):34, 2019. ISSN 1999-4893. doi:[10.3390/a12020034](https://doi.org/10.3390/a12020034).
- [72] B. Hall. *Lie Groups, Lie Algebras, and Representations: An Elementary Introduction*. Graduate Texts in Mathematics. Springer, 2003. ISBN 9780387401225.
- [73] Aram W. Harrow and Richard A. Low. Random quantum circuits are approximate 2-designs. *Communications in Mathematical Physics*, 291(1):257–302, 2009. doi:[10.1007/s00220-009-0873-6](https://doi.org/10.1007/s00220-009-0873-6).
- [74] Douglas Rayner Hartree and W. Hartree. Self-consistent field, with exchange, for beryllium. *Proceedings of the Royal Society of London. Series A - Mathematical and Physical Sciences*, 150(869):9–33, 1935. doi:[10.1098/rspa.1935.0085](https://doi.org/10.1098/rspa.1935.0085).

- [75] Tobias Haug, Kishor Bharti, and M.S. Kim. Capacity and quantum geometry of parametrized quantum circuits. *PRX Quantum*, 2:040309, 2021. doi:[10.1103/PRXQuantum.2.040309](https://doi.org/10.1103/PRXQuantum.2.040309).
- [76] M. Hebenstreit, R. Jozsa, B. Kraus, S. Strelchuk, and M. Yoganathan. All pure fermionic non-gaussian states are magic states for matchgate computations. *Phys. Rev. Lett.*, 123:080503, 2019. doi:[10.1103/PhysRevLett.123.080503](https://doi.org/10.1103/PhysRevLett.123.080503).
- [77] Rebekah Herrman, Phillip C. Lotshaw, James Ostrowski, Travis S. Humble, and George Siopsis. Multi-angle quantum approximate optimization algorithm. *Scientific Reports*, 12(1), 2022. doi:[10.1038/s41598-022-10555-8](https://doi.org/10.1038/s41598-022-10555-8).
- [78] Wen Wei Ho and Timothy H. Hsieh. Efficient variational simulation of non-trivial quantum states. *SciPost Phys.*, 6:29, 2019. doi:[10.21468/SciPostPhys.6.3.029](https://doi.org/10.21468/SciPostPhys.6.3.029).
- [79] Wen Wei Ho, Cheryne Jonay, and Timothy H. Hsieh. Ultrafast variational simulation of nontrivial quantum states with long-range interactions. *Phys. Rev. A*, 99(5):052332, 2019. doi:[10.1103/PhysRevA.99.052332](https://doi.org/10.1103/PhysRevA.99.052332).
- [80] Zoë Holmes, Kunal Sharma, M. Cerezo, and Patrick J. Coles. Connecting ansatz expressibility to gradient magnitudes and barren plateaus. *PRX Quantum*, 3:010313, 2022. doi:[10.1103/PRXQuantum.3.010313](https://doi.org/10.1103/PRXQuantum.3.010313).
- [81] C. Hubig, I. P. McCulloch, and U. Schollwöck. Generic construction of efficient matrix product operators. *Phys. Rev. B*, 95:035129, 2017. doi:[10.1103/PhysRevB.95.035129](https://doi.org/10.1103/PhysRevB.95.035129).
- [82] William Huggins, Piyush Patil, Bradley Mitchell, K Birgitta Whaley, and E Miles Stoudenmire. Towards quantum machine learning with tensor networks. *Quantum Science and Technology*, 4(2):024001, 2019. doi:[10.1088/2058-9565/aaca94](https://doi.org/10.1088/2058-9565/aaca94).
- [83] Ferenc Iglói. Quantum hard rods: Critical behavior and conformal invariance. *Phys. Rev. B*, 40(4):2362–2367, 1989. doi:[10.1103/PhysRevB.40.2362](https://doi.org/10.1103/PhysRevB.40.2362).
- [84] Ernst Ising. Beitrag zur theorie des ferromagnetismus. *Zeitschrift für Physik*, 31(1):253–258, 1925. doi:[10.1007/bf02980577](https://doi.org/10.1007/bf02980577).

- [85] L. ISSERLIS. ON CERTAIN PROBABLE ERRORS AND CORRELATION COEFFICIENTS OF MULTIPLE FREQUENCY DISTRIBUTIONS WITH SKEW REGRESSION. *Biometrika*, 11(3):185–190, 1916. doi:[10.1093/biomet/11.3.185](https://doi.org/10.1093/biomet/11.3.185).
- [86] Ammar Jahin, Andy C. Y. Li, Thomas Iadecola, Peter P. Orth, Gabriel N. Perdue, Alexandru Macridin, M. Sohaib Alam, and Norm M. Tubman. Fermionic approach to variational quantum simulation of kitaev spin models. *Physical Review A*, 106(2), 2022. doi:[10.1103/physreva.106.022434](https://doi.org/10.1103/physreva.106.022434).
- [87] Paul Niklas Jepsen, Jesse Amato-Grill, Ivana Dimitrova, Wen Wei Ho, Eugene Demler, and Wolfgang Ketterle. Spin transport in a tunable Heisenberg model realized with ultracold atoms. *Nature*, 588(7838):403–407, 2020. ISSN 1476-4687. doi:[10.1038/s41586-020-3033-y](https://doi.org/10.1038/s41586-020-3033-y).
- [88] Zhang Jiang, Kevin J. Sung, Kostyantyn Kechedzhi, Vadim N. Smelyanskiy, and Sergio Boixo. Quantum algorithms to simulate many-body physics of correlated fermions. *Phys. Rev. Applied*, 9:044036, 2018. doi:[10.1103/PhysRevApplied.9.044036](https://doi.org/10.1103/PhysRevApplied.9.044036).
- [89] James D. Johnson, Samuel Krinsky, and Barry M. McCoy. Vertical-arrow correlation length in the eight-vertex model and the low-lying excitations of the XYZ Hamiltonian. *Phys. Rev. A*, 8:2526–2547, 1973. doi:[10.1103/PhysRevA.8.2526](https://doi.org/10.1103/PhysRevA.8.2526).
- [90] R.O. Jones. Density functional theory: Its origins, rise to prominence, and future. *Reviews of Modern Physics*, 87(3):897–923, 2015. doi:[10.1103/revmodphys.87.897](https://doi.org/10.1103/revmodphys.87.897).
- [91] P. Jordan and E. Wigner. Über das paulische Äquivalenzverbot. *Zeitschrift für Physik*, 47(9-10):631–651, 1928. doi:[10.1007/bf01331938](https://doi.org/10.1007/bf01331938).
- [92] R. Jozsa and A. Miyake. Matchgates and classical simulation of quantum circuits. *Proc. R. Soc. A.*, pages 3089–3106, 2008. doi:[10.1098/rspa.2008.0189](https://doi.org/10.1098/rspa.2008.0189).
- [93] Abhinav Kandala, Antonio Mezzacapo, Kristan Temme, Maika Takita, Markus Brink, Jerry M. Chow, and Jay M. Gambetta. Hardware-efficient variational quantum eigensolver for small molecules and quantum magnets. *Nature*, 549(7671):242–246, 2017. doi:[10.1038/nature23879](https://doi.org/10.1038/nature23879).

- [94] Bobak Toussi Kiani, Seth Lloyd, and Reevu Maity. Learning unitaries by gradient descent, 2020. doi:[10.48550/ARXIV.2001.11897](https://doi.org/10.48550/ARXIV.2001.11897).
- [95] Joonho Kim, Jaedeok Kim, and Dario Rosa. Universal effectiveness of high-depth circuits in variational eigenproblems. *Phys. Rev. Research*, 3:023203, 2021. doi:[10.1103/PhysRevResearch.3.023203](https://doi.org/10.1103/PhysRevResearch.3.023203).
- [96] Ian D. Kivlichan, Jarrod McClean, Nathan Wiebe, Craig Gidney, Alán Aspuru-Guzik, Garnet Kin-Lic Chan, and Ryan Babbush. Quantum simulation of electronic structure with linear depth and connectivity. *Phys. Rev. Lett.*, 120:110501, 2018. doi:[10.1103/PhysRevLett.120.110501](https://doi.org/10.1103/PhysRevLett.120.110501).
- [97] Christian Kokail, Rick van Bijnen, Andreas Elben, Benoît Vermersch, and Peter Zoller. Entanglement Hamiltonian tomography in quantum simulation. *Nature Physics*, 2021. doi:[10.1038/s41567-021-01260-w](https://doi.org/10.1038/s41567-021-01260-w).
- [98] L. Landau. Theory of the superfluidity of helium II. *Physical Review*, 60(4):356–358, 1941. doi:[10.1103/physrev.60.356](https://doi.org/10.1103/physrev.60.356).
- [99] Martin Larocca, Nathan Ju, Diego García-Martín, Patrick J. Coles, and M. Cerezo. Theory of overparametrization in quantum neural networks, 2021. doi:[10.48550/ARXIV.2109.11676](https://doi.org/10.48550/ARXIV.2109.11676).
- [100] Martin Larocca, Piotr Czarnik, Kunal Sharma, Gopikrishnan Muraleedharan, Patrick J. Coles, and M. Cerezo. Diagnosing barren plateaus with tools from quantum optimal control. *Quantum*, 6:824, 2022. doi:[10.22331/q-2022-09-29-824](https://doi.org/10.22331/q-2022-09-29-824).
- [101] Martín Larocca, Frédéric Sauvage, Faris M. Sbahi, Guillaume Verdon, Patrick J. Coles, and M. Cerezo. Group-invariant quantum machine learning. *PRX Quantum*, 3(3), 2022. doi:[10.1103/prxquantum.3.030341](https://doi.org/10.1103/prxquantum.3.030341).
- [102] R. B. Laughlin. Anomalous quantum Hall effect: An incompressible quantum fluid with fractionally charged excitations. *Phys. Rev. Lett.*, 50:1395–1398, 1983. doi:[10.1103/PhysRevLett.50.1395](https://doi.org/10.1103/PhysRevLett.50.1395).
- [103] Hui Li and F. D. M. Haldane. Entanglement Spectrum as a Generalization of Entanglement Entropy: Identification of Topological Order in Non-Abelian Fractional Quantum Hall Effect States. *Phys. Rev. Lett.*, 101(1):010504, 2008. doi:[10.1103/PhysRevLett.101.010504](https://doi.org/10.1103/PhysRevLett.101.010504).

- [104] Daniel Liang, Li Li, and Stefan Leichenauer. Investigating quantum approximate optimization algorithms under bang-bang protocols. *Phys. Rev. Research*, 2: 033402, 2020. doi:[10.1103/PhysRevResearch.2.033402](https://doi.org/10.1103/PhysRevResearch.2.033402).
- [105] Elliott Lieb, Theodore Schultz, and Daniel Mattis. Two soluble models of an antiferromagnetic chain. *Annals of Physics*, 16(3):407–466, 1961. ISSN 0003-4916. doi:[https://doi.org/10.1016/0003-4916\(61\)90115-4](https://doi.org/10.1016/0003-4916(61)90115-4).
- [106] E.M. Lifshitz and L. P. Pitaevskii (Auth.). *Statistical Physics. Theory of the Condensed State*. 1980. ISBN 9780080503509; 0080503500.
- [107] Sheng-Hsuan Lin, Rohit Dilip, Andrew G. Green, Adam Smith, and Frank Pollmann. Real- and imaginary-time evolution with compressed quantum circuits. *PRX Quantum*, 2(1), 2021. doi:[10.1103/prxquantum.2.010342](https://doi.org/10.1103/prxquantum.2.010342).
- [108] Andrew Lucas. Ising formulations of many NP problems. *Frontiers in Physics*, 2, 2014. doi:[10.3389/fphy.2014.00005](https://doi.org/10.3389/fphy.2014.00005).
- [109] Chufan Lyu, Xiaoyu Tang, Junning Li, Xusheng Xu, Man-Hong Yung, and Abolfazl Bayat. Variational quantum simulation of long-range interacting systems. *New Journal of Physics*, 25(5):053022, 2023. doi:[10.1088/1367-2630/acd571](https://doi.org/10.1088/1367-2630/acd571).
- [110] Mohammad F. Maghrebi, Zhe-Xuan Gong, and Alexey V. Gorshkov. Continuous symmetry breaking in 1d long-range interacting quantum systems. *Phys. Rev. Lett.*, 119:023001, 2017. doi:[10.1103/PhysRevLett.119.023001](https://doi.org/10.1103/PhysRevLett.119.023001).
- [111] Ettore Majorana. Teoria simmetrica dell’elettrone e del positrone. *Il Nuovo Cimento*, 14(4):171–184, 1937. doi:[10.1007/bf02961314](https://doi.org/10.1007/bf02961314).
- [112] Damian Markham, Jarosław Adam Miszczyk, Zbigniew Puchała, and Karol Życzkowski. Quantum state discrimination: A geometric approach. *Phys. Rev. A*, 77:042111, 2008. doi:[10.1103/PhysRevA.77.042111](https://doi.org/10.1103/PhysRevA.77.042111).
- [113] Carlos Ortiz Marrero, Mária Kieferová, and Nathan Wiebe. Entanglement-induced barren plateaus. *PRX Quantum*, 2(4), 2021. doi:[10.1103/prxquantum.2.040316](https://doi.org/10.1103/prxquantum.2.040316).

- [114] Gabriel Matos, Andrew Hallam, Aydin Deger, Zlatko Papić, and Jiannis K. Pachos. Emergence of gaussianity in the thermodynamic limit of interacting fermions. *Phys. Rev. B*, 104:L180408, 2021. doi:[10.1103/PhysRevB.104.L180408](https://doi.org/10.1103/PhysRevB.104.L180408).
- [115] Gabriel Matos, Sonika Johri, and Zlatko Papić. Quantifying the efficiency of state preparation via quantum variational eigensolvers. *PRX Quantum*, 2:010309, 2021. doi:[10.1103/PRXQuantum.2.010309](https://doi.org/10.1103/PRXQuantum.2.010309).
- [116] Gabriel Matos, Chris N. Self, Zlatko Papić, Konstantinos Meichanetzidis, and Henrik Dreyer. Characterization of variational quantum algorithms using free fermions. *Quantum*, 7:966, 2023. doi:[10.22331/q-2023-03-30-966](https://doi.org/10.22331/q-2023-03-30-966).
- [117] Anton Mazurenko, Christie S. Chiu, Geoffrey Ji, Maxwell F. Parsons, Márton Kanász-Nagy, Richard Schmidt, Fabian Grusdt, Eugene Demler, Daniel Greif, and Markus Greiner. A cold-atom Fermi–Hubbard antiferromagnet. *Nature*, 545 (7655):462–466, 2017. ISSN 1476-4687. doi:[10.1038/nature22362](https://doi.org/10.1038/nature22362).
- [118] Glen Bigan Mbeng, Rosario Fazio, and Giuseppe Santoro. Quantum annealing: a journey through digitalization, control, and hybrid quantum variational schemes, 2019. doi:[10.48550/ARXIV.1906.08948](https://doi.org/10.48550/ARXIV.1906.08948).
- [119] Glen Bigan Mbeng, Rosario Fazio, and Giuseppe E. Santoro. Optimal quantum control with digitized quantum annealing, 2019. doi:[10.48550/ARXIV.1911.12259](https://doi.org/10.48550/ARXIV.1911.12259).
- [120] Jarrod R. McClean, Jonathan Romero, Ryan Babbush, and Alán Aspuru-Guzik. The theory of variational hybrid quantum-classical algorithms. *New Journal of Physics*, 18(2):023023, 2016. doi:[10.1088/1367-2630/18/2/023023](https://doi.org/10.1088/1367-2630/18/2/023023).
- [121] Jarrod R. McClean, Sergio Boixo, Vadim N. Smelyanskiy, Ryan Babbush, and Hartmut Neven. Barren plateaus in quantum neural network training landscapes. *Nature Communications*, 9(1), 2018. doi:[10.1038/s41467-018-07090-4](https://doi.org/10.1038/s41467-018-07090-4).
- [122] Konstantinos Meichanetzidis, Christopher J. Turner, Ashk Farjami, Zlatko Papić, and Jiannis K. Pachos. Free-fermion descriptions of parafermion chains and string-net models. *Phys. Rev. B*, 97:125104, 2018. doi:[10.1103/PhysRevB.97.125104](https://doi.org/10.1103/PhysRevB.97.125104).

- [123] Antonio A. Mele, Glen B. Mbeng, Giuseppe E. Santoro, Mario Collura, and Pietro Torta. Avoiding barren plateaus via transferability of smooth solutions in a hamiltonian variational ansatz. *Physical Review A*, 106(6), 2022. doi:[10.1103/physreva.106.l060401](https://doi.org/10.1103/physreva.106.l060401).
- [124] Johannes Jakob Meyer, Marian Mularski, Elies Gil-Fuster, Antonio Anna Mele, Francesco Arzani, Alissa Wilms, and Jens Eisert. Exploiting symmetry in variational quantum machine learning. *PRX Quantum*, 4(1), 2023. doi:[10.1103/prxquantum.4.010328](https://doi.org/10.1103/prxquantum.4.010328).
- [125] Nikolaj Moll, Panagiotis Barkoutsos, Lev S Bishop, Jerry M Chow, Andrew Cross, Daniel J Egger, Stefan Filipp, Andreas Fuhrer, Jay M Gambetta, Marc Ganzhorn, Abhinav Kandala, Antonio Mezzacapo, Peter Müller, Walter Riess, Gian Salis, John Smolin, Ivano Tavernelli, and Kristan Temme. Quantum optimization using variational algorithms on near-term quantum devices. *Quantum Science and Technology*, 3(3):030503, 2018. doi:[10.1088/2058-9565/aab822](https://doi.org/10.1088/2058-9565/aab822).
- [126] Ashley Montanaro. Quantum algorithms: an overview. *npj Quantum Information*, 2(1), 2016. doi:[10.1038/npjqi.2015.23](https://doi.org/10.1038/npjqi.2015.23).
- [127] Ashley Montanaro and Stasja Stanisic. Error mitigation by training with fermionic linear optics, 2021. doi:[10.48550/ARXIV.2102.02120](https://doi.org/10.48550/ARXIV.2102.02120).
- [128] M. E. S. Morales, J. D. Biamonte, and Z. Zimborás. On the universality of the quantum approximate optimization algorithm. *Quantum Information Processing*, 19(9), 2020. doi:[10.1007/s11128-020-02748-9](https://doi.org/10.1007/s11128-020-02748-9).
- [129] C. M. Morris, R. Valdés Aguilar, A. Ghosh, S. M. Koohpayeh, J. Krizan, R. J. Cava, O. Tchernyshyov, T. M. McQueen, and N. P. Armitage. Hierarchy of bound states in the one-dimensional ferromagnetic ising chain  $\text{CoNb}_2\text{O}_6$  investigated by high-resolution time-domain terahertz spectroscopy. *Phys. Rev. Lett.*, 112:137403, 2014. doi:[10.1103/PhysRevLett.112.137403](https://doi.org/10.1103/PhysRevLett.112.137403).
- [130] S. Murmann, F. Deuretzbacher, G. Zürn, J. Bjerlin, S. M. Reimann, L. Santos, T. Lompe, and S. Jochim. Antiferromagnetic Heisenberg spin chain of a few cold atoms in a one-dimensional trap. *Phys. Rev. Lett.*, 115:215301, 2015. doi:[10.1103/PhysRevLett.115.215301](https://doi.org/10.1103/PhysRevLett.115.215301).

- [131] Naoto Nagaosa. *Quantum Field Theory in Condensed Matter Physics*. Springer Berlin Heidelberg, 1999. doi:[10.1007/978-3-662-03774-4](https://doi.org/10.1007/978-3-662-03774-4).
- [132] M. Nakahara. *Geometry, Topology, and Physics*. Geometry, Topology, and Physics. Institute of Physics Pub., 2017. ISBN 9781138413368.
- [133] Kouhei Nakaji and Naoki Yamamoto. Expressibility of the alternating layered ansatz for quantum computation. *Quantum*, 5:434, 2021. ISSN 2521-327X. doi:[10.22331/q-2021-04-19-434](https://doi.org/10.22331/q-2021-04-19-434).
- [134] Michael A. Nielsen. Cluster-state quantum computation. *Reports on Mathematical Physics*, 57(1):147 – 161, 2006. ISSN 0034-4877. doi:[https://doi.org/10.1016/S0034-4877\(06\)80014-5](https://doi.org/10.1016/S0034-4877(06)80014-5).
- [135] Michael A. Nielsen and Isaac L. Chuang. *Quantum Computation and Quantum Information: 10th Anniversary Edition*. Cambridge University Press, 2010.
- [136] Tomotoshi Nishino. Density matrix renormalization group method for 2D classical models. *Journal of the Physical Society of Japan*, 64(10):3598–3601, 1995. doi:[10.1143/JPSJ.64.3598](https://doi.org/10.1143/JPSJ.64.3598).
- [137] Tomotoshi Nishino and Kouichi Okunishi. Corner transfer matrix algorithm for classical renormalization group. *Journal of the Physical Society of Japan*, 66(10):3040–3047, 1997. doi:[10.1143/JPSJ.66.3040](https://doi.org/10.1143/JPSJ.66.3040).
- [138] J. Nocedal and S. Wright. *Numerical Optimization*. Springer Series in Operations Research and Financial Engineering. Springer New York, 2006. ISBN 9780387227429. doi:[10.1007/978-0-387-40065-5](https://doi.org/10.1007/978-0-387-40065-5).
- [139] Ken N. Okada, Keita Osaki, Kosuke Mitarai, and Keisuke Fujii. Identification of topological phases using classically-optimized variational quantum eigensolver, 2022. doi:[10.48550/ARXIV.2202.02909](https://doi.org/10.48550/ARXIV.2202.02909).
- [140] Matthew J. O’Rourke, Zhendong Li, and Garnet Kin-Lic Chan. Efficient representation of long-range interactions in tensor network algorithms. *Phys. Rev. B*, 98:205127, 2018. doi:[10.1103/PhysRevB.98.205127](https://doi.org/10.1103/PhysRevB.98.205127).

- [141] Román Orús, Samuel Mugel, and Enrique Lizaso. Quantum computing for finance: Overview and prospects. *Reviews in Physics*, 4:100028, 2019. ISSN 2405-4283. doi:<https://doi.org/10.1016/j.revip.2019.100028>.
- [142] Stellan Östlund and Stefan Rommer. Thermodynamic limit of density matrix renormalization. *Physical Review Letters*, 75(19):3537–3540, 1995. doi:[10.1103/physrevlett.75.3537](https://doi.org/10.1103/physrevlett.75.3537).
- [143] Michał Oszmaniec, Ninnat Dangniam, Mauro E.S. Morales, and Zoltán Zimborás. Fermion sampling: A robust quantum computational advantage scheme using fermionic linear optics and magic input states. *PRX Quantum*, 3:020328, 2022. doi:[10.1103/PRXQuantum.3.020328](https://doi.org/10.1103/PRXQuantum.3.020328).
- [144] Matthew Otten, Cristian L. Cortes, and Stephen K. Gray. Noise-resilient quantum dynamics using symmetry-preserving ansatzes, 2019. doi:[10.48550/ARXIV.1910.06284](https://doi.org/10.48550/ARXIV.1910.06284).
- [145] Carlos Outeiral, Martin Strahm, Jiye Shi, Garrett M. Morris, Simon C. Benjamin, and Charlotte M. Deane. The prospects of quantum computing in computational molecular biology. *WIREs Computational Molecular Science*, 11(1):e1481, 2021. doi:<https://doi.org/10.1002/wcms.1481>.
- [146] A. A. Ovchinnikov, D. V. Dmitriev, V. Ya. Krivnov, and V. O. Cheranovskii. Antiferromagnetic Ising chain in a mixed transverse and longitudinal magnetic field. *Phys. Rev. B*, 68(21):214406, 2003. doi:[10.1103/PhysRevB.68.214406](https://doi.org/10.1103/PhysRevB.68.214406).
- [147] Jiannis K. Pachos and Zlatko Papić. Quantifying the effect of interactions in quantum many-body systems. *SciPost Phys. Lect. Notes*, page 4, 2018. doi:[10.21468/SciPostPhysLectNotes.4](https://doi.org/10.21468/SciPostPhysLectNotes.4).
- [148] Guido Pagano, Aniruddha Bapat, Patrick Becker, Katherine S. Collins, Arinjoy De, Paul W. Hess, Harvey B. Kaplan, Antonis Kyprianidis, Wen Lin Tan, Christopher Baldwin, Lucas T. Brady, Abhinav Deshpande, Fangli Liu, Stephen Jordan, Alexey V. Gorshkov, and Christopher Monroe. Quantum approximate optimization of the long-range ising model with a trapped-ion quantum simulator. *Proceedings of the National Academy of Sciences*, 117(41):25396–25401, 2020. doi:[10.1073/pnas.2006373117](https://doi.org/10.1073/pnas.2006373117).

- [149] J.B. Parkinson and D.J.J. Farnell. *An Introduction to Quantum Spin Systems*. Lecture Notes in Physics. Springer Berlin Heidelberg, 2010. ISBN 9783642132902.
- [150] Kristian Patrick, Vincent Caudrelier, Zlatko Papić, and Jiannis K. Pachos. Interaction distance in the extended XXZ model. *Phys. Rev. B*, 100:235128, 2019. doi:[10.1103/PhysRevB.100.235128](https://doi.org/10.1103/PhysRevB.100.235128).
- [151] Kristian Patrick, Marcela Herrera, Jake Southall, Irene D'Amico, and Jiannis K. Pachos. Efficiency of free auxiliary models in describing interacting fermions: From the kohn-sham model to the optimal entanglement model. *Physical Review B*, 100(7), 2019. doi:[10.1103/physrevb.100.075133](https://doi.org/10.1103/physrevb.100.075133).
- [152] G. Pelegrí, J. Mompart, V. Ahufinger, and A. J. Daley. Quantum magnetism with ultracold bosons carrying orbital angular momentum. *Phys. Rev. A*, 100:023615, 2019. doi:[10.1103/PhysRevA.100.023615](https://doi.org/10.1103/PhysRevA.100.023615).
- [153] K. A. Penson, J. M. Debierre, and L. Turban. Conformal invariance and critical behavior of a quantum Hamiltonian with three-spin coupling in a longitudinal field. *Phys. Rev. B*, 37(13):7884–7887, 1988. doi:[10.1103/PhysRevB.37.7884](https://doi.org/10.1103/PhysRevB.37.7884).
- [154] Alberto Peruzzo, Jarrod McClean, Peter Shadbolt, Man-Hong Yung, Xiao-Qi Zhou, Peter J. Love, Alán Aspuru-Guzik, and Jeremy L. O'Brien. A variational eigenvalue solver on a photonic quantum processor. *Nature Communications*, 5(1):4213, 2014. ISSN 2041-1723. doi:[10.1038/ncomms5213](https://doi.org/10.1038/ncomms5213).
- [155] Ingo Peschel. Calculation of reduced density matrices from correlation functions. *Journal of Physics A: Mathematical and General*, 36(14):L205–L208, 2003. doi:[10.1088/0305-4470/36/14/101](https://doi.org/10.1088/0305-4470/36/14/101).
- [156] Ingo Peschel. On the reduced density matrix for a chain of free electrons. *Journal of Statistical Mechanics: Theory and Experiment*, 2004(06):P06004, 2004. doi:[10.1088/1742-5468/2004/06/p06004](https://doi.org/10.1088/1742-5468/2004/06/p06004).
- [157] Ingo Peschel and Viktor Eisler. Reduced density matrices and entanglement entropy in free lattice models. *Journal of Physics A: Mathematical and Theoretical*, 42(50):504003, 2009. doi:[10.1088/1751-8113/42/50/504003](https://doi.org/10.1088/1751-8113/42/50/504003).

- [158] Ingo Peschel, Matthias Kaulke, and Örs Legeza. Density-matrix spectra for integrable models. *Annalen der Physik*, 511(2):153–164, 1999. doi:[10.1002/andp.19995110203](https://doi.org/10.1002/andp.19995110203).
- [159] Pierre Pfeuty. The one-dimensional Ising model with a transverse field. *Annals of Physics*, 57(1):79 – 90, 1970. ISSN 0003-4916. doi:[https://doi.org/10.1016/0003-4916\(70\)90270-8](https://doi.org/10.1016/0003-4916(70)90270-8).
- [160] Hannes Pichler, Guanyu Zhu, Alireza Seif, Peter Zoller, and Mohammad Hafezi. Measurement protocol for the entanglement spectrum of cold atoms. *Phys. Rev. X*, 6:041033, 2016. doi:[10.1103/PhysRevX.6.041033](https://doi.org/10.1103/PhysRevX.6.041033).
- [161] Fernanda Pinheiro, Georg M. Bruun, Jani-Petri Martikainen, and Jonas Larson. XYZ quantum Heisenberg models with  $p$ -orbital bosons. *Phys. Rev. Lett.*, 111:205302, 2013. doi:[10.1103/PhysRevLett.111.205302](https://doi.org/10.1103/PhysRevLett.111.205302).
- [162] B Pirvu, V Murg, J I Cirac, and F Verstraete. Matrix product operator representations. *New Journal of Physics*, 12(2):025012, 2010. doi:[10.1088/1367-2630/12/2/025012](https://doi.org/10.1088/1367-2630/12/2/025012).
- [163] Frank Pollmann, Ari M. Turner, Erez Berg, and Masaki Oshikawa. Entanglement spectrum of a topological phase in one dimension. *Phys. Rev. B*, 81(6):064439, 2010. doi:[10.1103/PhysRevB.81.064439](https://doi.org/10.1103/PhysRevB.81.064439).
- [164] John Preskill. Quantum Computing in the NISQ era and beyond. *Quantum*, 2:79, 2018. ISSN 2521-327X. doi:[10.22331/q-2018-08-06-79](https://doi.org/10.22331/q-2018-08-06-79).
- [165] Robert Raussendorf, Daniel E. Browne, and Hans J. Briegel. Measurement-based quantum computation on cluster states. *Phys. Rev. A*, 68:022312, 2003. doi:[10.1103/PhysRevA.68.022312](https://doi.org/10.1103/PhysRevA.68.022312).
- [166] S.R.P.G. Ripka, J.P. Blaizot, and G. Ripka. *Quantum Theory of Finite Systems*. MIT Press, 1986. ISBN 9780262022149.
- [167] Stefan H. Sack, Raimel A. Medina, Alexios A. Michailidis, Richard Kueng, and Maksym Serbyn. Avoiding barren plateaus using classical shadows. *PRX Quantum*, 3(2), 2022. doi:[10.1103/prxquantum.3.020365](https://doi.org/10.1103/prxquantum.3.020365).

- [168] A. Scheie, N. E. Sherman, M. Dupont, S. E. Nagler, M. B. Stone, G. E. Granroth, J. E. Moore, and D. A. Tennant. Detection of Kardar–Parisi–Zhang hydrodynamics in a quantum Heisenberg spin-1/2 chain. *Nature Physics*, 17(6):726–730, 2021. ISSN 1745-2481. doi:[10.1038/s41567-021-01191-6](https://doi.org/10.1038/s41567-021-01191-6).
- [169] Ulrich Schollwöck. The density-matrix renormalization group in the age of matrix product states. *Annals of Physics*, 326(1):96–192, 2011. doi:[10.1016/j.aop.2010.09.012](https://doi.org/10.1016/j.aop.2010.09.012).
- [170] Norbert Schuch and Bela Bauer. Matrix product state algorithms for gaussian fermionic states. *Physical Review B*, 100(24), 2019. doi:[10.1103/physrevb.100.245121](https://doi.org/10.1103/physrevb.100.245121).
- [171] Norbert Schuch, Michael M. Wolf, Frank Verstraete, and J. Ignacio Cirac. Entropy scaling and simulability by matrix product states. *Phys. Rev. Lett.*, 100:030504, 2008. doi:[10.1103/PhysRevLett.100.030504](https://doi.org/10.1103/PhysRevLett.100.030504).
- [172] Norbert Schuch, David Pérez-García, and Ignacio Cirac. Classifying quantum phases using matrix product states and projected entangled pair states. *Phys. Rev. B*, 84:165139, 2011. doi:[10.1103/PhysRevB.84.165139](https://doi.org/10.1103/PhysRevB.84.165139).
- [173] Maria Schuld and Nathan Killoran. Is quantum advantage the right goal for quantum machine learning? *PRX Quantum*, 3(3), 2022. doi:[10.1103/prxquantum.3.030101](https://doi.org/10.1103/prxquantum.3.030101).
- [174] Jacob T. Seeley, Martin J. Richard, and Peter J. Love. The bravyi-kitaev transformation for quantum computation of electronic structure. *The Journal of Chemical Physics*, 137(22):224109, 2012. doi:[10.1063/1.4768229](https://doi.org/10.1063/1.4768229).
- [175] Ruslan Shaydulin and Stefan M. Wild. Exploiting symmetry reduces the cost of training qaoa. *IEEE Transactions on Quantum Engineering*, 2:1–9, 2021. doi:[10.1109/TQE.2021.3066275](https://doi.org/10.1109/TQE.2021.3066275).
- [176] Sukin Sim, Peter D. Johnson, and Alán Aspuru-Guzik. Expressibility and entangling capability of parameterized quantum circuits for hybrid quantum-classical algorithms. *Advanced Quantum Technologies*, 2(12):1900070, 2019. doi:[10.1002/qute.201900070](https://doi.org/10.1002/qute.201900070).

- [177] J. C. Slater. A simplification of the hartree-fock method. *Physical Review*, 81(3): 385–390, 1951. doi:[10.1103/physrev.81.385](https://doi.org/10.1103/physrev.81.385).
- [178] Pietro Smacchia, Luigi Amico, Paolo Facchi, Rosario Fazio, Giuseppe Florio, Saverio Pascazio, and Vlatko Vedral. Statistical mechanics of the cluster Ising model. *Phys. Rev. A*, 84:022304, 2011. doi:[10.1103/PhysRevA.84.022304](https://doi.org/10.1103/PhysRevA.84.022304).
- [179] James Stokes, Josh Izaac, Nathan Killoran, and Giuseppe Carleo. Quantum natural gradient. *Quantum*, 4:269, 2020. doi:[10.22331/q-2020-05-25-269](https://doi.org/10.22331/q-2020-05-25-269).
- [180] Zheng-Hang Sun, Yong-Yi Wang, Jian Cui, and Heng Fan. Improving the performance of quantum approximate optimization for preparing non-trivial quantum states without translational symmetry. *New Journal of Physics*, 25(1):013015, 2023. doi:[10.1088/1367-2630/acb22c](https://doi.org/10.1088/1367-2630/acb22c).
- [181] Kevin J Sung, Marko J Rančić, Olivia T Lanes, and Nicholas T Bronn. Simulating majorana zero modes on a noisy quantum processor. *Quantum Science and Technology*, 8(2):025010, 2023. doi:[10.1088/2058-9565/acb796](https://doi.org/10.1088/2058-9565/acb796).
- [182] Jacopo Surace and Luca Tagliacozzo. Fermionic gaussian states: an introduction to numerical approaches. *SciPost Physics Lecture Notes*, 2022. doi:[10.21468/scipostphyslectnotes.54](https://doi.org/10.21468/scipostphyslectnotes.54).
- [183] Bill Sutherland. Two-dimensional hydrogen bonded crystals without the ice rule. *Journal of Mathematical Physics*, 11(11):3183–3186, 1970. doi:[10.1063/1.1665111](https://doi.org/10.1063/1.1665111).
- [184] Bill Sutherland. *Beautiful Models*. WORLD SCIENTIFIC, 2004. doi:[10.1142/5552](https://doi.org/10.1142/5552).
- [185] Hiroshi Takasaki, Toshiya Hikihara, and Tomotoshi Nishino. Fixed point of the finite system DMRG. *Journal of the Physical Society of Japan*, 68(5):1537–1540, 1999. doi:[10.1143/jpsj.68.1537](https://doi.org/10.1143/jpsj.68.1537).
- [186] Leon Armenovich Takhtadzhyan and Lyudvig Dmitrievich Faddeev. The quantum method of the inverse problem and the Heisenberg xyz model. *Uspekhi Matematicheskikh Nauk*, 34(5):13–63, 1979.

- [187] Leticia Tarruell and Laurent Sanchez-Palencia. Quantum simulation of the hubbard model with ultracold fermions in optical lattices. *Comptes Rendus Physique*, 19(6):365–393, 2018. doi:[10.1016/j.crhy.2018.10.013](https://doi.org/10.1016/j.crhy.2018.10.013).
- [188] Barbara M. Terhal and David P. DiVincenzo. Classical simulation of noninteracting-fermion quantum circuits. *Phys. Rev. A*, 65:032325, 2002. doi:[10.1103/PhysRevA.65.032325](https://doi.org/10.1103/PhysRevA.65.032325).
- [189] Jules Tilly, Hongxiang Chen, Shuxiang Cao, Dario Picozzi, Kanav Setia, Ying Li, Edward Grant, Leonard Wossnig, Ivan Rungger, George H. Booth, and Jonathan Tennyson. The variational quantum eigensolver: a review of methods and best practices, 2021. doi:[10.48550/ARXIV.2111.05176](https://doi.org/10.48550/ARXIV.2111.05176).
- [190] Nikolay V. Tkachenko, James Sud, Yu Zhang, Sergei Tretiak, Petr M. Anisimov, Andrew T. Arrasmith, Patrick J. Coles, Lukasz Cincio, and Pavel A. Dub. Correlation-informed permutation of qubits for reducing ansatz depth in the variational quantum eigensolver. *PRX Quantum*, 2:020337, 2021. doi:[10.1103/PRXQuantum.2.020337](https://doi.org/10.1103/PRXQuantum.2.020337).
- [191] T. T. Truong and I. Peschel. Diagonalisation of finite-size corner transfer matrices and related spin chains. *Zeitschrift für Physik B Condensed Matter*, 75(1):119–125, 1989. doi:[10.1007/bf01313574](https://doi.org/10.1007/bf01313574).
- [192] Christopher J. Turner, Konstantinos Meichanetzidis, Zlatko Papić, and Jiannis K. Pachos. Optimal free descriptions of many-body theories. *Nature Communications*, 8(1):14926, 2017. ISSN 2041-1723. doi:[10.1038/ncomms14926](https://doi.org/10.1038/ncomms14926).
- [193] A V Uvarov and J D Biamonte. On barren plateaus and cost function locality in variational quantum algorithms. *Journal of Physics A: Mathematical and Theoretical*, 54(24):245301, 2021. doi:[10.1088/1751-8121/abfac7](https://doi.org/10.1088/1751-8121/abfac7).
- [194] J. G. Valatin. Comments on the theory of superconductivity. *Il Nuovo Cimento*, 7(6):843–857, 1958. doi:[10.1007/bf02745589](https://doi.org/10.1007/bf02745589).
- [195] Leslie G. Valiant. Quantum circuits that can be simulated classically in polynomial time. *SIAM Journal on Computing*, 31(4):1229–1254, 2002. doi:[10.1137/S0097539700377025](https://doi.org/10.1137/S0097539700377025).

- [196] Laurens van der Maaten and Geoffrey Hinton. Visualizing data using t-sne. *Journal of Machine Learning Research*, 9(86):2579–2605, 2008.
- [197] Ruben Verresen, Roderich Moessner, and Frank Pollmann. One-dimensional symmetry protected topological phases and their transitions. *Phys. Rev. B*, 96:165124, 2017. doi:[10.1103/PhysRevB.96.165124](https://doi.org/10.1103/PhysRevB.96.165124).
- [198] F Verstraete and J I Cirac. Mapping local hamiltonians of fermions to local hamiltonians of spins. *Journal of Statistical Mechanics: Theory and Experiment*, 2005(09):P09012–P09012, 2005. doi:[10.1088/1742-5468/2005/09/p09012](https://doi.org/10.1088/1742-5468/2005/09/p09012).
- [199] G. Vidal. Classical simulation of infinite-size quantum lattice systems in one spatial dimension. *Physical Review Letters*, 98(7), 2007. doi:[10.1103/physrevlett.98.070201](https://doi.org/10.1103/physrevlett.98.070201).
- [200] Guifré Vidal. Efficient classical simulation of slightly entangled quantum computations. *Physical Review Letters*, 91(14), 2003. doi:[10.1103/physrevlett.91.147902](https://doi.org/10.1103/physrevlett.91.147902).
- [201] David J. Wales and Jonathan P. K. Doye. Global optimization by basin-hopping and the lowest energy structures of lennard-jones clusters containing up to 110 atoms. *The Journal of Physical Chemistry A*, 101(28):5111–5116, 1997. doi:[10.1021/jp970984n](https://doi.org/10.1021/jp970984n).
- [202] Samson Wang, Enrico Fontana, M. Cerezo, Kunal Sharma, Akira Sone, Lukasz Cincio, and Patrick J. Coles. Noise-induced barren plateaus in variational quantum algorithms. *Nature Communications*, 12(1):6961, 2021. ISSN 2041-1723. doi:[10.1038/s41467-021-27045-6](https://doi.org/10.1038/s41467-021-27045-6).
- [203] Zhihui Wang, Stuart Hadfield, Zhang Jiang, and Eleanor G. Rieffel. Quantum approximate optimization algorithm for maxcut: A fermionic view. *Phys. Rev. A*, 97:022304, 2018. doi:[10.1103/PhysRevA.97.022304](https://doi.org/10.1103/PhysRevA.97.022304).
- [204] Dave Wecker, Matthew B. Hastings, and Matthias Troyer. Progress towards practical quantum variational algorithms. *Physical Review A*, 92(4), 2015. doi:[10.1103/physreva.92.042303](https://doi.org/10.1103/physreva.92.042303).
- [205] Steven R. White. Density matrix formulation for quantum renormalization groups. *Physical Review Letters*, 69(19):2863–2866, 1992. doi:[10.1103/physrevlett.69.2863](https://doi.org/10.1103/physrevlett.69.2863).

- [206] Steven R. White. Density-matrix algorithms for quantum renormalization groups. *Physical Review B*, 48(14):10345–10356, 1993. doi:[10.1103/physrevb.48.10345](https://doi.org/10.1103/physrevb.48.10345).
- [207] Steven R. White. Density matrix renormalization group algorithms with a single center site. *Physical Review B*, 72(18), 2005. doi:[10.1103/physrevb.72.180403](https://doi.org/10.1103/physrevb.72.180403).
- [208] G. C. Wick. The evaluation of the collision matrix. *Physical Review*, 80(2): 268–272, 1950. doi:[10.1103/physrev.80.268](https://doi.org/10.1103/physrev.80.268).
- [209] David Wierichs, Christian Gogolin, and Michael Kastoryano. Avoiding local minima in variational quantum eigensolvers with the natural gradient optimizer. *Phys. Rev. Res.*, 2:043246, 2020. doi:[10.1103/PhysRevResearch.2.043246](https://doi.org/10.1103/PhysRevResearch.2.043246).
- [210] Roeland Wiersema, Cunlu Zhou, Yvette de Sereville, Juan Felipe Carrasquilla, Yong Baek Kim, and Henry Yuen. Exploring entanglement and optimization within the hamiltonian variational ansatz. *PRX Quantum*, 1:020319, 2020. doi:[10.1103/PRXQuantum.1.020319](https://doi.org/10.1103/PRXQuantum.1.020319).
- [211] Bennet Windt, Alexander Jahn, Jens Eisert, and Lucas Hackl. Local optimization on pure Gaussian state manifolds. *SciPost Phys.*, 10:66, 2021. doi:[10.21468/SciPostPhys.10.3.066](https://doi.org/10.21468/SciPostPhys.10.3.066).
- [212] Zhi-Cheng Yang, Armin Rahmani, Alireza Shabani, Hartmut Neven, and Claudio Chamon. Optimizing variational quantum algorithms using pontryagin’s minimum principle. *Physical Review X*, 7(2), 2017. doi:[10.1103/physrevx.7.021027](https://doi.org/10.1103/physrevx.7.021027).
- [213] Sheir Yarkoni, Elena Raponi, Thomas Bäck, and Sebastian Schmitt. Quantum annealing for industry applications: introduction and review. *Reports on Progress in Physics*, 85(10):104001, 2022. doi:[10.1088/1361-6633/ac8c54](https://doi.org/10.1088/1361-6633/ac8c54).
- [214] A. B. Zamolodchikov. Integrals of motion and  $S$ -matrix of the scaled  $T = T_c$  ising model with magnetic field. *International Journal of Modern Physics A*, 04(16):4235–4248, 1989. doi:[10.1142/S0217751X8900176X](https://doi.org/10.1142/S0217751X8900176X).
- [215] Leo Zhou, Sheng-Tao Wang, Soonwon Choi, Hannes Pichler, and Mikhail D. Lukin. Quantum approximate optimization algorithm: Performance, mechanism, and implementation on near-term devices. *Physical Review X*, 10(2), 2020. doi:[10.1103/physrevx.10.021067](https://doi.org/10.1103/physrevx.10.021067).

- [216] Zeqiao Zhou, Yuxuan Du, Xinmei Tian, and Dacheng Tao. QAOA-in-QAOA: Solving large-scale MaxCut problems on small quantum machines. *Physical Review Applied*, 19(2), 2023. doi:[10.1103/physrevapplied.19.024027](https://doi.org/10.1103/physrevapplied.19.024027).
- [217] Linghua Zhu, Ho Lun Tang, George S. Barron, F. A. Calderon-Vargas, Nicholas J. Mayhall, Edwin Barnes, and Sophia E. Economou. Adaptive quantum approximate optimization algorithm for solving combinatorial problems on a quantum computer. *Physical Review Research*, 4(3), 2022. doi:[10.1103/physrevresearch.4.033029](https://doi.org/10.1103/physrevresearch.4.033029).